QUANTITATIVE IMAGE ANALYSIS IN THE STUDY OF NEUTROPHIL AND NEUTROPHIL-LIKE HL-60 CHEMOTAXIS

APPROVED BY SUPERVISORY COMMITTEE

Steven J. Altschuler, Ph.D. (Co-mentor)

Melanie H. Cobb, Ph.D. (Co-mentor)

Lani F. Wu, Ph.D. (Co-mentor)

Benjamin Tu, Ph.D. (Chair)

James Stull, Ph.D.

Paul Blount, Ph.D.

DEDICATION

First and foremost, I would like to thank my mentors, Dr. Melanie Cobb, Dr. Steven Altschuler, and Dr. Lani Wu, as well as the members of my Graduate Committee: Dr. Benjamin Tu, Dr. Paul Blount, and Dr. James Stull. Your incredible support and intellectual push have helped me develop as a scientist, and I am indebted.

I thank Dr. Chonlarat Wichaidit for MATLAB mentoring, Dr. Orion Weiner and Dr. Curtis Thorne for enlightening discussions, and Dr. Yanqin Wang and Dr. Shanshan Liu for my training in experimental techniques. I also thank the University of Texas Southwestern Medical Scientist Training Program for transitional funding when Drs. Altschuler and Wu moved to UCSF.

Finally, I would like to thank my family. My mother, Dr. Ping Yao, encouraged me to pursue a career in research rather than "only" using the status quo as a medical doctor. (Really, Mom?) My husband, our dog, and our cat (Dr. Josef Velten, Toblerone "Toby" Newton, and Fondue "Kitty!" Schrödinger, respectively) kept my soul alive during graduate school. Thank you for being my home.

QUANTITATIVE IMAGE ANALYSIS IN THE STUDY OF NEUTROPHIL AND NEUTROPHIL-LIKE HL-60 CHEMOTAXIS

by

ELIZABETH REN ZHANG-VELTEN

DISSERTATION

Presented to the Faculty of the Graduate School of Biomedical Sciences

The University of Texas Southwestern Medical Center at Dallas

In Partial Fulfillment of the Requirements

For the Degree of

DOCTOR OF PHILOSOPHY

The University of Texas Southwestern Medical Center at Dallas

Dallas, Texas

May 5, 2017

QUANTITATIVE IMAGE ANALYSIS IN THE STUDY OF NEUTROPHIL AND NEUTROPHIL-LIKE HL-60 CHEMOTAXIS

Publication No. _____

Elizabeth Ren Zhang-Velten

The University of Texas Southwestern Medical Center at Dallas, 2017

Supervising Professors: Melanie Cobb, PhD; Steven Altschuler, PhD; Lani Wu, PhD

Neutrophils are fast-moving first responders of the innate immune system. External chemoattractant signals result in neutrophil polarization: the neutrophil forms a leading edge (front) which constantly protrudes and retracts actin-rich pseudopods, and a contractile myosin-enriched trailing edge (back) which is insensitive and directionally persistent. Previous work has suggested that polymerized actin and contractile actomyosin segregate to the neutrophil's morphological front and back, respectively, due to mutual inhibition. Beyond this initial establishment of spatially segregated domains, however, many questions remain unclear. In this work, I address two questions: (i) first, how do the front and back of the

neutrophil demonstrate seemingly uncoupled behaviors despite these inhibitory links? (ii) and, second, at what fMLP concentration does neutrophil chemotaxis saturate, and how is this maximal concentration determined? With quantitative analysis of immunofluorescent fixed-cell images and live-cell migration videos, I demonstrate the role of microtubules in insulating the front and back modules of chemotactic neutrophils, and the role of ERK in driving neutrophil migration into maximal fMLP concentrations.

TABLE OF CONTENTS

PRIOR PUBLICATIONS ix

LIST OF FIGURES x

LIST OF TABLES xii

LIST OF APPENDICES xiii

LIST OF ABBREVIATIONS xiv

CHAPTER 1. INTRODUCTION

I. Acute inflammation 1

II. Neutrophil chemotactic signaling 3

III. Quantitative biology 7

IV. Thesis aims 11

CHAPTER 2. IDENTIFYING NETWORK MOTIFS THAT INSULATE FRONT-TO-BACK SIGNALING IN POLARIZED NEUTROPHILS

I. Introduction 13

II. Results 16

III. Discussion 27

IV. Materials and methods 31

V. Supplementary methods 34

VI. Figures 42

VII. Tables 54

CHAPTER 3. CONCENTRATION-DEPENDENT TUNING OF ERK DYNAMICS IN NEUTROPHILS AND NEUTROPHIL-LIKE HL-60 CELLS

I. Introduction 57

II. Results 58

III. Discussion 62

IV. Materials and methods 64

V. Figures 69

CHAPTER 4. CONCLUSIONS AND FUTURE DIRECTIONS

I. Microtubule-mediated regulation of the $G_{12/13}$-initiated back module 80

II. MAPK regulation of neutrophil chemotaxis 82

III. C5a-mediated neutrophil dysfunction 83

IV. Conclusion 85

V. Figures 86

APPENDICES 87

REFERENCES 109

PRIOR PUBLICATIONS

Zhang, E. R., Liu, S., Wu, L.F.*, Altschuler, S.J.*, Cobb, M.H.* Chemoattractant concentration–dependent tuning of ERK signaling dynamics in migrating neutrophils. Sci. Signal. 9.458 (2016): ra122-ra122.

Zhang, E. R., Wu, L. F., & Altschuler, S. J. (2013). Envisioning migration: mathematics in both experimental analysis and modeling of cell behavior. *Current Opinion in Cell Biology*, *25*(5), 538-542.

Wang, Y.*, Ku, C. J.*, **Zhang, E. R.***, Artyukhin, A. B., Weiner, O. D., Wu, L. F., & Altschuler, S. J. (2013). Identifying network motifs that buffer front-to-back signaling in polarized neutrophils. *Cell Reports*, *3*(5), 1607-1616.

Swirski, F. K., Wildgruber, M., Ueno, T., Figueiredo, J. L., Panizzi, P., Iwamoto, Y., **Zhang, E.**, & Nahrendorf, M. (2010). Myeloperoxidase-rich Ly-6C+ myeloid cells infiltrate allografts and contribute to an imaging signature of organ rejection in mice. *The Journal of Clinical Investigation*, 120(7), 2627.

Forghani, R., Wojtkiewicz, G. R., Zhang, Y., Seeburg, D., Bautz, B. R., Pulli, B., Milewski, A., Atkinson, W.L., Iwamoto, Y., **Zhang, E.R.**, … & Chen, J. W. (2012). Demyelinating diseases: myeloperoxidase as an imaging biomarker and therapeutic target. *Radiology*, 263(2), 451-460.

Egedal, J., Fox, W., Katz, N., Porkolab, M., Reim, K., & **Zhang, E.** (2007). Laboratory observations of spontaneous magnetic reconnection. *Physical Review Letters*, 98(1), 015003.

LIST OF FIGURES

Figure 1.1. Abridged overview of fMLP-induced signaling through formyl peptide receptor (R) coupled to G_i and $G_{12/13}$. 5

Figure 2.1. Neutrophil polarity network. 42

Figure 2.2. Microtubules insulate back pMLC2 localization against varying front F-actin levels in polarized human neutrophils 43

Figure 2.3. A mathematical model of microtubule interactions with front and back modules reveals a role for insulating localization of back signaling 44

Figure 2.4. Systematic assessment of the performance of different polarity network topologies in insulating the localization of back signaling 46

Figure 2.S1. Back signaling is constant across a wide range of front readouts 47

Figure 2.S2. Validation of response synchrony and microscopy methods 49

Figure 2.S3. Replicates of different drug-treatment conditions 51

Figure 2.S4. Schema of different network topologies used in studies 53

Figure 3.1. Overview of gradient characterization 69

Figure 3.2. Morphology changes, but not ERK1/2 activation, terminate within 10 min..... 71

Figure 3.3. ERK, but not p38, is required for migration toward fMLP 72

Figure 3.4. p38 inhibits ERK at late timepoints..... 73

Figure 3.S1. Migration of cells across a linear fMLP gradient..... 75

Figure 3.S2. ERK activation remains elevated in cells responding to 10 nM fMLP 76

Figure 3.S3. p-p38 falls to or past baseline within 10 minutes of fMLP stimulation. 77

Figure. 3.S4. p38 inhibition results in elevated pERK at late timepoints after 10 or 100 nM fMLP exposure 78

Figure 3.S5. On-target effects of MAPK inhibitors 79

Figure 4.1. Graphical abstract of microtubule-mediated regulation of the $G_{12/13}$-initiated back module 86

Figure 4.2. Neutrophil polarization response to 10 nM fMLP, with and without 30 minutes of 10 nM C5a pretreatment 86

LIST OF TABLES

TABLE 2.1 54

TABLE 2.2 55

TABLE 2.3 56

LIST OF APPENDICES

APPENDIX A 87

APPENDIX B 92

APPENDIX C 95

LIST OF ABBREVIATIONS

C5a - complement component 5a

CCD - charge-coupled device

DMSO - dimethyl sulfoxide

ERK - extracellular signal-regulated protein kinase

fMLP - N-formyl-methionyl-leucyl-phenylalnine

FPR - formyl peptide receptor

GEF - guanine exchange factor

GPCR - guanine nucleotide–binding protein (G protein)–coupled receptor

GTP - guanosine-5'-triphosphate

K_D - equilibrium dissociation constant

LSP1 - Leukocyte-specific protein 1

MAPK - mitogen-activated protein kinase

MAPKAPK2 - MAP kinase-activated protein kinase 2

MATLAB - Matrix Laboratory programming language

MEK - MAP kinase/ERK kinase

PI3K - phosphoinositide 3-kinase

PIP3 - phosphatidyl-inositol 3,4,5-trisphosphate

PKA - protein kinase A

pMLC2 - phospho-myosin light chain 2

CHAPTER ONE
Introduction

Acute inflammation: Neutrophil chemotaxis leads the charge

Bacterial invasion of the body occurs daily, even with routine activities such as tooth-brushing and chewing food [86]. Inflammation is the body's protective response [56] to such invasion, in which leukocytes (white blood cells) and blood vessels work together to eliminate the bacteria, remove necrotic cells and tissues, and initiate the process of repair [127]. Acute inflammation is the host's opening salvo: local blood vessels dilate [56] and become more permeable [24] so that the first responders of the leukocytes—neutrophils—may storm the injured tissue [127].

Neutrophils are the most abundant type of leukocyte in the human circulation [2]. In the setting of acute inflammation caused by bacteria, neutrophils deliver a targeted attack by following host-derived intermediary chemoattractants, such as interleukin-8 and leukotriene B4, to the general vicinity [49] of infection. Once on scene, neutrophils then pursue bacteria by interpreting gradients of end-target chemoattractants such as the bacterial peptide N-formyl-methionyl-leucyl-phenyalanine (fMLP) [49, 174]. If successful, this process will allow a neutrophil to engulf its prey into a phagosome [145, 97], which then fuses to a lysosome [53], thus exposing the bacterium to bactericidal agents such as reactive oxygen species, reactive nitrogen species, lysozymes, and hypochlorous acid [1, 71, 171, 91]. Clinically, acute inflammation has a fast onset of minutes to hours, and produces prominent, "cardinal" signs—defined by 1st century encyclopedist Aulus Cornelis Celsus as *calor* (heat), *rubor* (redness), *tumor* (swelling),

and *dolor* (pain) [37], and amended by 2nd century physician Galen to include *functio laesa* (loss of function) [121]. Once the inciting pathogens are removed by neutrophils, however, acute inflammation is usually resolved with little tissue injury or fibrosis [56]—vascular permeability falls to a normal state [64], thus shunting neutrophils away from the previous site of inflammation, and inflammatory cells and mediators within the tissue are cleared by lymphatic drainage [4].

Clinically, the importance of neutrophil chemotaxis is highlighted by the finding that neutrophil chemotaxis becomes hyperactive during infection; neutrophils isolated from the peripheral circulation of patients with active bacterial infections show significantly increased migration toward bacterial products in *in vitro* assays, as compared to neutrophils from healthy, age-matched donors, and the chemotactic overdrive persists until infection is treated with adequate antibiotic therapy [51]. In short: without effective neutrophil chemotaxis, bacteria remain at large [10, 52, 111, 100]. In such a setting, the host is at risk of unresolved acute inflammation, which will harm bystander cells, resulting in pus formation [56] and fibrosis [130, 27], and may even progress to chronic inflammation [56]. Chronic inflammation will produce severe and progressive tissue injury and fibrosis, as two other types of leukocytes—lymphocytes (B and T cells) and monocytes (which mature into macrophages)—infiltrate the area of infection [98, 142]. Uncontained bacterial infection may quickly evolve into systemic infection, sepsis, and death [159]. Therefore, neutrophil chemotaxis is essential to managing the daily bacterial invasions associated with normal life—clearing those pathogens with minimal harm to the body's own tissues.

Neutrophil chemotaxis relies on signal relay from external GPCRs to the cytoskeleton

In all eukaryotic cells, directional sensing is mediated by heterotrimeric guanine nucleotide–binding protein (G protein)–linked signaling pathways [72, 117, 140, 107, 25]. Formyl peptide receptors, the G protein-coupled receptors that bind fMLP, are essential for bacterial pursuit. A clinical example of the significance of formyl peptide receptors is Job's syndrome, in which neutrophils express far fewer formyl peptide receptors than normal [100]. In these patients, neutrophil chemotaxis toward fMLP is defective [52, 111], resulting in recurrent infections, pus-filled skin and lung lesions, and the need for lifelong treatment with antibiotics [52].

In normal human neutrophils, formyl peptide receptors remain uniformly distributed along the cell's perimeter, even when the neutrophil is exposed to a gradient [136, 165]. However, $G_{\beta\gamma}$ subunits become slightly biased toward the direction of higher fMLP concentration [165, 63]. This asymmetry is amplified at the level of phosphatidyl-inositol 3,4,5-trisphosphate (PIP3), which forms a sharp intracellular gradient, also toward the direction of higher fMLP concentration [151]. Thus, directional sensing in neutrophils occurs with high sensitivity, such that an fMLP concentration difference of even 1-2% across the cell's diameter can direct movement [173].

Formyl peptide receptors couple to both G_i and $G_{12/13}$ proteins, which initiate divergent pathways. G_i signaling mediates production of membrane PIP3 by phosphoinositide 3-kinase (PI3K) [135]. The GTPases Rac and Cdc42 are thus recruited

to the membrane and activated, and in turn promote formation of actin polymers [9]. Conversely, $G_{12/13}$ signaling promotes activation of RhoA GTPase [44], which in turn activates Rho-associated protein kinase [59]. Rho-associated protein kinase facilitates phosphorylation and activation of myosin II [31], both by stoichiometrically phosphorylating myosin regulatory light chain (MLC2) [3], and by phosphorylating the myosin-binding subunit of myosin light chain phosphatase, thereby inhibiting the phosphatase activity towards myosin [70].

Polymerized F-actin and contractile actomyosin are biochemically incompatible, and thus these two distinct cytoskeletal assemblies are mutually inhibitory [167]. This incompatibility is reinforced by mutual, upstream inhibitory links between the G_i-initiated and $G_{12/13}$-initiated pathways: PI3K and F-actin inhibit basal RhoA activity, and Rho-associated protein kinase inhibits fMLP-stimulated Rac activation (**Fig. 1.1**) [167]. As a result of this multilevel mutual inhibition, the respective components of the G_i-initiated and $G_{12/13}$-initiated pathways spatially segregate from one another. Thus, the initial signaling events that achieve directional sensing in turn drive the process of neutrophil polarization—the cell's morphological transformation from a rounded shape to an asymmetrical configuration with F-actin-rich pseudopods on one side, and an actomyosin-rich uropod on the other [167].

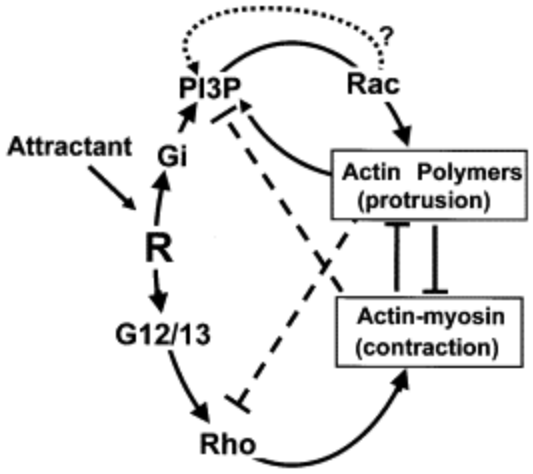

Figure 1.1. Abridged overview of fMLP-induced signaling through formyl peptide receptor (R) coupled to G_i and $G_{12/13}$. Reprinted from Xu et al., 2003 [167].

But, in this setting of an fMLP gradient, do the pseudopods or the uropod develop on the up-gradient side of the neutrophil? Although a tug-of-war is initiated through the mutual inhibition between the G_i-initiated and $G_{12/13}$-initiated pathways, positive feedback between PIP3, Rac (**Fig. 1.1**, dotted arrow) [157] and F-actin [57] downstream of G_i serves to ensure that actin-rich pseudopods win this up-gradient territory. $G_{12/13}$-initiated uropod formation is therefore constrained to the side of the neutrophil with lower external fMLP [160]. Consistent with the need for neutrophils to be fast-moving first responders, this process happens quickly: ruffled pseudopods [175] appear within 20 seconds of fMLP exposure [167], and the neutrophil becomes fully polarized by 2-3 minutes of fMLP exposure [76, 152, 167].

The morphological change seen in neutrophil polarization is accompanied by functional changes along the cell's diameter. The positive feedback between PIP3, Rac,

and F-actin [157, 57] downstream of G_i also serves to increase sensitivity. As a result, the side of the neutrophil that initially forms PIP3-, Rac-, and actin-enriched pseudopods will more easily foster *de novo* pseudopod formation—thus pushing the cell forward [167, 174]. In short, the G_i-initiated, F-actin-enriched, morphological "front" of the neutrophil serves as the leading edge.

The downstream myosin II of the $G_{12/13}$ pathway does not provide sensitizing positive feedback as seen in the case of PIP3, Rac, and F-actin in the G_i pathway [167]. Myosin II does, however, regulate the spatial localization of its upstream activator PDZRhoGEF [161], such that PDZRhoGEF, RhoA, Rho-associated protein kinase, myosin II, and actomyosin spatially reinforce one another. This regulation further enriches the uropod with actomyosin [161], thereby creating a spatially concentrated incompatibility for actin-rich pseudopod formation. Meanwhile, myosin contraction promotes retraction of the uropod across its substrate [31]. Thus, the $G_{12/13}$-initiated "back" of a neutrophil becomes the trailing edge.

Experimentally, these morphological and functional changes of neutrophil polarization can be seen by placing a micropipette filled with fMLP in the vicinity of a previously unstimulated neutrophil. The neutrophil will break its symmetry by forming a pseudopod in the direction of the micropipette, and migrate toward the micropipette with the protrusion and retraction of more pseudopods [174, 167]. If the micropipette is then abruptly moved to the uropod at the now-established back of the neutrophil [167, 174], the cell cannot produce a pseudopod at that position [167, 174]. Instead, the neutrophil will either collapse to an unpolarized, rounded shape before repolarizing in the direction

of the micropipette, or perform a U-turn toward the micropipette [167, 174]. Therefore, the spatial segregation of cytoskeletal assemblies, which belies morphological polarization of the neutrophil, also informs the cell's chemotactic behavior.

This functional significance of polarization and chemotaxis, downstream of receptor-mediated directional sensing, can also be clinically observed in neutrophil actin dysfunction: a disease caused by overexpression of a leukocyte-specific [83] intracellular actin-binding protein, LSP1 [54], which results in poor actin polymerization in neutrophils [141]. Neutrophils from neutrophil actin deficiency patients show a normal to increased reactive oxygen species burst in response to fMLP, suggesting that formyl peptide receptor signaling is intact [21]. Instead, downstream of directional sensing by formyl peptide receptors, the neutrophils display a complete lack of polarization when exposed to fMLP [21] and profoundly impaired chemotaxis [10, 21]. As a result of these defects in polarization and chemotaxis, patients suffer recurrent bacterial infections [10, 54].

Envisioning migration: Mathematics in both experimental analysis and modeling of cell behavior

From the vantage point of the tremendous body of work above, a current challenge is to understand how these many signaling components receive and coordinate signals to produce productive chemotaxis. Mathematics has often been viewed as an endpoint for experimental studies: experimentally measured biochemical constants for known interactions are incorporated into equations, which can then be tested for their

ability to recapitulate observed behavior. Recent advances have, however, allowed the emergence of a complementary approach: mathematics may be used to enhance experimental resolution and analysis. While traditional biological assays will continue to reveal important facets of neutrophil chemotaxis, chemotaxis is also a particularly suitable subject for mathematically fine-tuned experimental methods, for reasons which I discuss below.

Spatial coordination

Although the segregation of signaling components is critical for chemotaxis, this spatial process is difficult to analyze; traditional methods such as Western blots [167], light scattering [114], and standard flow cytometry cannot provide spatial information. Recent complementary approaches allow quantitative characterization of this spatial information. Spatial cross-correlative analyses, for example, have allowed measurement of the distance from the cell edge at which GTPase activity peaked [90], showed that PI3K reinforces rather than produces protrusions in fibroblasts [158], and that N-BAR proteins are directly recruited to the plasma membrane by membrane-curving forces [39]. Analysis of the spatial compactness of cytoskeletal readouts of polarizing primary neutrophils identified differential paths of information flow [76] and the insulation of the back signaling from the front signaling by the microtubules [152]. Quantifying spatial parameters allows trends in probe localization to be not only identified, but also tested for statistical significance, thus opening a new arena of study.

Meanwhile, clever image analysis has further been used to extract much more quantitative spatial information from the cell shape itself. Driscoll et al. used kymographs to study the evolution of cell shape, and found that *Dictyostelium discoideum* cells change shape *via* traveling curvature waves, possibly due to actomyosin dynamics [29]. Barnhart et al. [7] tracked contours and created edge velocity maps of keratocytes on substrates of different adhesion strengths. They found that keratocyte speed and shape have a biphasic dependence on adhesion strength, and that adhesion strength (without long-term adaptation) is sufficient for switching the migration behavior of cells. These authors' methods transform cell shape itself into a rich resource for the study of cell migration.

Timescales and cell-to-cell asynchrony

An additional difficulty in studying cell migration is achieving adequate temporal resolution, as the characteristic timescales of cell migration are very short. For example, neutrophils can rapidly transform extracellular cues into protrusive changes, creating actin ruffles within 20 seconds of initial chemoattractant exposure [175], and undergoing shape oscillations with a period of roughly 8 seconds [34]. This is in stark contrast to studies of other periodic behavior such as circadian clocks or stages of the cell cycle, where timescales may be on the order of hours to days. An offset of seconds between two migrating cells can be equivalent to a half-period shift. Readouts across a population of cells will thus be heterogeneous and hard to interpret in absolute time. Further, unlike cell cycle studies, in which cells may be synchronized with methods such as serum starvation,

the protrusion-retraction cycles of separately migrating cells are not synchronized with one another. Traditional biochemical assays may demonstrate whether one protein activates, inhibits, or does not affect another protein. However, to further explore the signaling behavior and functional implications of a biochemical circuit, the temporal coordination of the components must be studied. The study of migrating cells thus requires high temporal resolution and resourceful computational methods that circumvent the difficulty of interpretation caused by cell-to-cell asynchrony within a population.

Recent studies have addressed the issue of asynchrony with an elegant computational multiplexing approach: the activity of a probe and the edge movement of the membrane are read out from the same cell, and the relative time and distance between probe activation and cell edge movement is recorded. This approach thus allows one readout from many individual cells to be pooled, and pools may be compared for multiple probes to uncover the coordination of the proteins represented by the probes. This approach has recently uncovered the relative timing of GTPases within protrusions of fibroblasts [90], demonstrated the role of RhoGDI in the temporal regulation of RhoA[147], and predicted fluctuations of intracellular forces from the F-actin network [61]. Meanwhile, Marco et al. [92] developed a mathematical model to characterize the relations of several parameters of cell polarization, and then designed an experiment that tied in closely with their model. This model-directed experiment allowed extraction of different parameters, which are experimentally difficult to measure independently, and preserved context by allowing simultaneous measurement from the same timepoints and

individual cells. Specialized application of mathematics can permit both computational alignment of asynchronous events and synchronous extraction of parameters, and is thus especially powerful for the study of chemotaxis.

Applying quantitative image analysis to current questions in neutrophil chemotaxis

In this work, I apply quantitative image analysis to two questions within the field of neutrophil chemotaxis. First, I address the question of front/back insulation within polarizing neutrophils. Neutrophil polarity relies on local, mutual inhibition to segregate incompatible signaling circuits to the leading and trailing edges [167]. Mutual inhibition alone should lead to cells having strong fronts and weak backs or vice versa. However, analysis of cell-to-cell variation in human neutrophils revealed that back polarity remains consistent despite changes in front strength. How is this insulation achieved? Pharmacological perturbations and mathematical modeling revealed a new functional role for microtubules to insulate back phospho-myosin light chain 2 (pMLC2) localization from front F-actin fluctuations, by mediating positive, long-range crosstalk from front to back; loss of microtubules inhibits this insulation and results in anti-correlation between front and back signaling [152, 148]. Further, a systematic, computational search of network topologies found that a long-range, positive front-to-back link is necessary for back insulation. Thus, quantitative image analysis and modeling were used in this work to suggest a design principle that can be employed by polarity networks: short-range mutual inhibition establishes distinct signaling regions, after which directed long-range activation insulates one region from variations in the other.

Another question that I explore is the regulation and role of ERK (extracellular signal-regulated protein kinase) in neutrophil chemotaxis. The mitogen-activated protein kinases ERK1/2 have recently been implicated in switching fMLP-concentration-dependent migration from directional to circuitous. Recent controversy has further arisen over whether ERK1/2 are necessary for [103] or inhibit [85] neutrophil migration. Here, I used the selective inhibitors PD0325901 and SCH772984 to demonstrate that ERK1/2 are absolutely required for neutrophil migration. Additionally, I showed with BIRB-796, VX-702, and SB203580 that p38 modulates the response of ERK to fMLP, but that p38 by itself is dispensable for directional migration. Together, my data demonstrate that fMLP activates ERK1/2 in gradated responses, that p38 modulates the decay of these responses back toward baseline, and that ERK1/2 support neutrophil chemotaxis toward fMLP.

CHAPTER TWO

Identifying network motifs that insulate front-to-back signaling in polarized neutrophils

Introduction

Neutrophils are fast-moving first responders of the immune system that are essential for the innate response against invading pathogens. Upon stimulation with chemoattractant, neutrophils adopt a polarized morphology by forming a protrusive F-actin-enriched leading edge ("front") and a contractile myosin-enriched trailing edge ("back"). A large body of work has identified many biochemical components and interactions within the neutrophil polarity network and placed them into distinct G_i-mediated "front" and $G_{12/13}$ back signaling modules (**Fig. 2.1A**) [144, 167] whose activities regulate the behaviors of the morphological front and back. These studies suggest a core network motif in which local mutual inhibition between front and back establishes spatially segregated domains [167], whereas front positive feedback is a driving force in maintaining polarity [57, 157].

How might this core motif of mutual front-back inhibition and positive front feedback affect the relation between front and back signaling? On the one hand, the positive feedback loop in the front should permit front signals to overpower and strongly

diminish back signals in their inhibitory "tug of war" within the cell [148, 160]; this suggests an anticorrelated trend between the back and front (**Fig. 2.1B**, top) [148]. On the other hand, a long-range positive link from the front module to the back module has been observed (**Fig. 2.1B**, bottom, blue arrow) [79, 148] and has been proposed to promote front-back balancing by creating proportionate increases in the back signaling pathway, following activations in the front signaling pathway [148]; this suggests a positively correlated trend between the front and back activation (**Fig. 2.1B**, bottom right).

Here, we explored these possibilities by studying the natural variation of downstream readouts of the front (F-actin) and back (pMLC2) modules in populations of polarized primary human neutrophils. We performed quantitative image analysis to extract measures of signaling phenotypes (activity and localization) of each of these readouts. We found that the relation between front and back signaling neither anticorrelated nor positively correlated, as originally postulated. Instead, back signaling is surprisingly constant across a wide range of front signaling levels (**Fig. 2.2** and **fig. 2.S1**), i.e., the back is insulated from the front.

How is this insulation achieved? Past experimental studies have uncovered evidence that microtubules could act as an intermediate for long-range communication between the front and the back of polarized neutrophils [79, 118]. We analyzed neutrophils with pharmacologically disrupted microtubules and found that microtubules additionally play a strong role in insulating back signaling from front signaling. However, they appear to do so predominantly via their effect on the localization but not the activity

of phosphorylated myosin. Experimental disruption of microtubules uncovered an anticorrelated trend between front activity and back localization. These data suggest that pMLC2 insulation depends on the role of microtubules in positively regulating transport [148, 168] rather than the inhibitory sequestration of back activators [168]. Thus, although the importance of microtubules in front-back communication has been established, we demonstrate here an unanticipated role of microtubules in protecting the localization of $G_{12/13}$-mediated pMLC2 activation from variations in G_i-mediated front signaling.

To computationally test whether microtubule-mediated regulation is sufficient to create insulation of pMLC2 localization, we developed a conceptual mathematical model of the core neutrophil network motif of front-module positive feedback coupled with front-back mutual inhibition. Our model of this core motif recapitulated the anticorrelated trend between front and back observed in microtubule-disrupted neutrophils, but the addition of a microtubule-mediated positive link from front to back helped to restore pMLC2 insulation. Finally, because the core motif of front positive feedback and front-back mutual inhibition is a conserved topology among various types of migrating cells [20, 146], we asked what additional links to the core motif could insulate back signaling. We systematically searched over network topologies [20, 89] containing the core motif and found within this collection that all topologies that recapitulated back insulation necessarily contained a positive long-range link from front to back. Together, our work demonstrates that (1) back signaling in neutrophils is surprisingly insulated from

variations in front signaling, (2) microtubules play an essential role in insulating the localization of back signaling and achieve this insulation primarily via back activation, and (3) a long-range positive link might be a general design principle for insulating spatially segregated signaling domains created via mutual inhibition.

Results

Front and back signaling phenotypes in polarized neutrophils

Previous studies have shown that analysis of cell-to-cell variability can reveal topological properties of signaling networks [15, 60, 73, 77, 120]. Here, we used this approach to examine how the back module (as read out by pMLC2) varies with respect to the front module (as read out by F-actin) within populations of polarized neutrophils. To reduce experimentally induced variability, we made use of primary human neutrophils, which exhibit a higher synchrony of chemotactic responses than cell lines like neutrophil-like HL-60s, and we studied natural fluctuations rather than using genetic or pharmacological disruptions [167, 148] to the front or back modules.

The strength and the spatial localization of signaling components of the neutrophil polarity network are regulated in different orders [76]. Thus, we measured cell-averaged intensities of F-actin and pMLC2 (**Fig. 2.2A** cartoon, horizontal axis) and also quantified the spatial localization patterns of F-actin and pMLC2 by computing their "spreadness,"

defined as the degree to which the brightest pixels for each marker were close together (low spreadness value) or far apart (high spreadness value) within each individual cell (**Fig. 2.2A** cartoon, vertical axis; see also supplementary methods for mathematical definition) [75]. Spreadness corresponds to the amount of area that within the cell that a marker takes up; in general, a measurement of low spreadness indicates a more polarized state, whereas a measurement of high spreadness indicates a less polarized state. Together, measurement of intensity and spreadness provided readouts of activity and polarity phenotypes for front and back modules.

Neutrophils produce and retract transient, actin-rich pseudopods as they explore their environments [174]. How does the back respond to these constant changes in the front? From our thousands of individually measured cells, we created density plots for simultaneously measured intensity and spreadness measures for both the pMLC2 and F-actin readouts. To assess front influence on the back, we calculated and plotted regression lines (**Fig. 2.2A**, top; **figs. 2.S1A** and **2.S1B**, black lines). Inspection of one of the four readout pairs, namely front spreadness versus back spreadness, showed a positive correlation. However, for the other three readout pairs, pMLC2 signaling appeared remarkably constant across the natural range of F-actin signaling. This observation raised the question of what network interactions within chemotactic neutrophils enable this insulation of pMLC2 from F-actin variations, despite known inhibitory interactions of F-actin on the back signaling module [167].

A functional role for microtubules in insulating pMLC2 localization from F-actin fluctuations

Previous studies have demonstrated crosstalk between microtubules and the front and back modules [76, 79, 118, 168, 148]. We therefore wondered whether microtubules play a role in creating the insulation we observed in the back module. To investigate this possibility, we pretreated neutrophils with nocodazole, a microtubule-depolymerizing drug, for 30 min before fMLP stimulation and searched for front-back relations that showed significant changes upon drug treatment (**Figs. 2.2A and 2.2B**). To only partially disrupt microtubule functions, we chose a nocodazole concentration (9 μM) that is lower than typical treatment conditions previously used to study neutrophil chemotaxis [168] and only partially reduces tubulin-staining intensity [76].

We quantified the effects of microtubule disruption in two ways. First, we compared the regression slopes between back and front signaling in control and nocodazole-treated cells. We found that disruption of microtubules via nocodazole significantly altered the correlation between back (pMLC2) spreadness and front (F-actin) intensity (**Fig. 2.2C**), but not for the other three pairs of front-back phenotypes (**fig. 2.S1C**, top). Specifically, for nocodazole-treated cells, we observed a significant change in anticorrelation (5.7-fold change to slope) between F-actin intensity and pMLC2 spreadness. Second, we measured variability based on the scatter of back phenotypes for given values of front phenotypes (i.e., the dispersion of back phenotypes along the regression line; **Fig. 2.2C**, gray vertical arrow). Variability increased significantly in the

nocodazole-treated condition for both F-actin intensity and F-actin spreadness versus pMLC2 spreadness (2.72- and 2.64-fold changes, respectively) (**Fig. 2.2C**, bottom; **fig. 2.S1C**, bottom). We noted that these trends were not due to increased variability in fMLP response times (**fig. 2.S2A**; in fact, nocodazole-treated cells had a tighter distribution of peak response times than control cells), nonuniform drug effects (**fig. 2.S2B**), morphological changes, or the number of bins used in computing slope (data not shown). Nocodazole treatment therefore highlighted a role for microtubules in keeping pMLC2 insulated from the inhibitory interactions of F-actin on pMLC2 and its upstream activators.

We further confirmed this loss of pMLC2 insulation with two other microtubule inhibitors, vinblastine and taxol (n = 6 replicates each; **fig. S3**; **Table 2.1**). Although vinblastine and taxol work quite differently from one another—vinblastine destabilizes microtubules and blocks microtubule-based transport, while taxol hyperstabilizes microtubules and leaves transport intact [81]—both drugs disrupted insulation of pMLC2 localization against variations F-actin intensity, while maintaining the insulation of pMLC2 intensity (from variations in either F-actin readout) (**Fig. 2.2C** and **fig. 2.S1C**). Reassuringly, no apparent loss of pMLC2 insulation was observed for cells treated with Akt1/Akt2 inhibitor (Akti), a drug that does not target microtubule machinery (**Fig. 2.2C** and **fig. 2.S1C**). Taken together, our data suggest that microtubules play a role in keeping the localization of back signaling consistent across the physiological range of F-actin signaling variations.

Next, we examined our control (non-drug-treated) cells to see whether natural variation in microtubule properties could reveal similar trends. We reanalyzed our images of non-drug-treated cells, ranked the control cells by the intensity or spreadness of microtubule staining, and studied the degree of insulation seen in the top and bottom 5% of the ranked cells. Cells in the top and bottom 5% of microtubule intensity showed similar abilities to insulate back pMLC2 localization from changes in front F-actin levels (**Fig. 2.2D**, bottom). However, the 5% of cells with the lowest microtubule spreadness showed remarkably consistent back localization, whereas the 5% of cells with the most microtubule spreadness showed dramatically increased variability (**Fig. 2.2D**, top). Taken together, our analysis of both natural and drug-induced perturbations of microtubules was consistent with the conclusion that the localization of microtubules is more important than the total mass of microtubules for creating back pMLC2 insulation.

An intriguing and unresolved question posed by previous work is whether microtubules predominantly act positively or negatively on the back module [168]. In the case of an activating role, microtubules were speculated to direct the transport of GEFs to the back; whereas in the case of an inhibiting role, microtubules were speculated to sequester these GEFs. In case of inhibitory sequestration of back-activating GEFs, a loss of microtubule mass would be expected to cause an increase in pMLC2 intensity by releasing GEFs throughout the cell. However, loss of microtubule mass via nocodazole treatment did not significantly alter the average pMLC2 intensity (**Fig. 2.2A**, left side), even though this dose of nocodazole was sufficient to cause a severe disruption in

pMLC2 localization (**Fig. 2.2A**, right side). This lack of change in pMLC2 intensity in nocodazole treatment argues against the sequestration model, and is consistent with our natural variation data, which showed that variations of microtubule mass (within a natural range) do not affect pMLC2 insulation (**Fig. 2.2D**, bottom). Together, these data suggest a positive and spatial role for a microtubule-mediated link in regulating back localization, consistent with transport of back-activating factors.

A conceptual mathematical model for investigating the role of microtubules in insulating back signaling localization

Is the network topology suggested by the experimental findings (mutual inhibition between front and back, a positive feedback loop in the front, and microtubules acting positively in a spatially dependent manner on the back) sufficient to produce the experimentally observed insulation of back polarity against front intensity? On one hand, one may see intuitively that microtubule-mediated activation of the back (implicated above) may counter mutual inhibition between the front and back. On the other hand, it is not clear whether the addition of this positive long-range link is sufficient to explain the observed insulating effect. Therefore, we made use of mathematical modeling to investigate the behavior that emerges from links among the front, back, and microtubules.

We chose a conceptual and phenomenological rather than a mechanistic and data-driven approach for modeling network interactions (see also **Appendix A** for discussion of conceptual versus data-driven modeling) because many detailed network parameters

are still unknown, and our primary goal was to understand the fundamental behaviors emerging from our identified network interactions [125, 172]. We note that this modeling effort is not intended to build an "end-to-end" model of neutrophil chemotaxis that predicts the entire process from chemoattractant sensing to symmetry breaking to motility. Rather, we focused on how neutrophils stabilize their asymmetry once asymmetry is established.

Many mathematical models have been proposed to investigate potential mechanisms underlying the initial symmetry breaking that establishes polarity in a cell [40, 58, 62, 67, 82, 94, 110, 116, 115, 109, 166, 156]. To model the core motif, we chose as our starting point a previously developed model for neutrophils in which front and back distributions evolve via a system of mass-conserved, reaction-diffusion equations (**Fig. 2.3A**, top left, gray-shaded background) [116]. This model captured the establishment of polarization for front and back signaling domains on a cell membrane represented as a one-dimensional interval, with stimulant presented in a spatial gradient. We modified this model as follows (**Table 2.2**). First, we simplified the model to capture interactions between a single front and a single back component. Second, we extended the model so that the spatial distributions of front and back were simulated on a one-dimensional circular (rather than an interval) cell membrane. Third, to mimic the conditions of our experiments conducted on human neutrophils, we allowed cells to spontaneously polarize in a uniform but noisy stimulation field rather than a gradient.

To simulate naturally occurring variability, we generated populations of "virtual" cells by randomly sampling parameters of the core motif within a small (1.5-fold) range of their nominal values [116] (**Table 2.2**). We additionally varied the total concentration of the front module over a larger (4-fold) concentration range to mimic variation to front signaling. In total, we generated 6,000 cells (1,000 per each of six front concentrations). As proxies for front intensity and back polarity, we computed the area under the front concentration curves (front area) and the width at half-maximal range of the back concentration curves (back width), respectively. Based on these simulations, we found that increased front concentrations resulted in decreased back widths, which led to a pronounced anticorrelation between front and back (**Fig. 2.3C**). These results were consistent with our experimental observations of cells with disrupted microtubules (**Fig. 2.2B**, bottom right; **Fig. 2.2D**, right).

A large body of computational work has also proposed detailed mathematical models of microtubules [30, 38, 101, 149] and examined their functions in different contexts, such as chromosomal spindle organization [42, 88] and the establishment of polarity in leukocytes [6, 58]. For our phenomenological model, we focused on experimental findings related to the distribution of microtubules and the role of microtubules in transporting back activators. First, in unstimulated primary human neutrophils, microtubules are uniformly distributed, but after neutrophils are stimulated with chemoattractant, microtubules are rapidly excluded from the front and reorient to the sides and backs of cells [32]. Second, microtubules are involved in the activation and

spatial distribution of back signaling components. As mentioned previously, microtubules locally deliver GEFs, some of which regulate localization of RhoA signaling activity [8, 126, 161]. Based on these experimental findings, we modeled two interactions between microtubules and the core polarity motif: exclusion of microtubules from the front, and microtubule-based activation of the back (**Fig. 2.3A** and **fig. 2.S4A**). Together, these two interactions constituted a long-range, positive link from front to back.

Our inclusion of microtubule interactions required an additional six parameters: exclusion, the strength of front-driven exclusion of the microtubules (θ); activation, the strength (k_M) and the spatial range (σ) of microtubule-based back activation; and microtubule distribution, the total number of microtubule cables (N_{MT}), the rate of microtubule repositioning (λ), and the minimum separation between individual microtubules (δ). In our model, the locations of microtubule cables were represented simply by the positions of their tips on the cell membrane (**Fig. 2.3A**, top right, blue circles).

Could our extended model with microtubule interactions recapitulate the experimentally observed insulation of back pMLC2 (**Fig. 2.2B**)? In our simulations, we started with uniform distributions for front and back and uniformly randomly chosen microtubule tip positions. During the simulation, cells rapidly underwent random symmetry breaking: front and back components self-organized into distinct signaling domains on the cell membrane, whereas microtubule tips also broke their uniform distributions to reorganize themselves toward the back (**Fig. 2.3B**, top). We found that in

the presence of microtubules, the slope decreased by ~46%, and variability decreased by ~35%. (In general, decreasing model parameters that helped deliver or spread back activation decreased back insulation [data not shown].) Thus, consistent with our experimental findings, our numerical studies suggested that the addition of a positive, long-range link mediated by microtubules could help to insulate back localization from front intensity variations within a cell and reduce variability of back signaling localization from cell to cell.

Systematic search for network topologies that insulate back from front

An intriguing question is whether the ability to insulate the back could be obtained by adding different links, or combinations of links, to this motif. The segregation of polarity network proteins to opposite poles in various migratory cells is regulated by a circuit containing positive feedback and mutual inhibition [20, 146]. We performed a systematic computational search of network topologies [20, 89, 73] to gain insight into how combinatorial additions of links to the core motif could insulate back polarity (**Fig. 2.4A** and **fig. 2.S4B**).

To identify general principles (and to make this search computationally tractable), we simplified and abstracted mechanisms of feedback and crosstalk. We again began with our modified model of the core motif. We implemented both positive and negative long-range interactions between front and back, using either a direct or indirect long-range link. We additionally considered local positive or negative feedback at the back.

We excluded network topologies that would have simply altered the strength of any existing link within the core circuit such as combining negative and positive links at the front. The set of all possible nonredundant additions to the core topology contained 6 topologies with one additional link, 12 topologies with two additional links, and 8 topologies with three additional links (**Fig. 2.4B** and **fig. 2.S4C**). We chose interaction strengths for these additional links that were large enough to have a noticeable effect compared with the reference model yet not so large as to eliminate polarization or overpower the original core topology (**Table 2.3**).

As before, we randomly generated virtual cells (n = 1,000) and measured the width of back signaling in polarized cells. To compare insulation performance, we again extracted the regression slope of front area versus back width from the scatterplots and the variability of back width along the regression line. We then computed the relative regression slopes or variabilities as measured by the logarithm of the ratio between these values for an extended model and the core motif. A value of zero meant that the model offered no change to regression slope or variability. A positive value indicated increased insulation capabilities, while a negative value indicated diminished insulation capabilities. Interestingly, we found that only the topology containing a long-range front-to-back positive interaction improved back insulation based on both metrics (**Fig. 2.4B**, topologies with green-shaded background). For certain network topologies, the front component overwhelmed the back by occupying a large portion of the cell membrane and

restricting the back to a small area regardless of parameter; we discarded these topologies from further analysis changes (**Fig. 2.4B**, topologies with gray-shaded background).

Our study also revealed that the directionality of the additional long-range link is important: the addition of a reversed long-range positive link from back to front did not insulate back width. This was due to pre-existing asymmetries in the core motif, namely positive feedback at the front, and a greater total amount of front than back components (based on existing literature [99]; **Table 2.2**, u_2 versus u_4). As a consequence, models with symmetric topologies (with respect to front and back) need not have similar insulation performance in our simulations. We further observed that the network with an additional back negative feedback link resulted in a significant loss of polarization. In this case, an inhibitory strength that was relatively weak (compared with the positive feedback link) was required to achieve a reasonable polarization rate; hence, the insulation performance of this topology was similar to that of the reference model. Finally, we observed that similar results were obtained regardless of whether we modeled the long-range links as direct (**Fig. 2.4C**) or indirect (**Fig. 2.4D**) connections between front and back. Taken together, all topologies in our computational search that recapitulated back insulation necessarily contained a positive long-range link from front to back. Thus, short-range negative crosstalk establishes spatially segregated front and back signaling domains, whereas long-range positive crosstalk insulates the back from changes in front signaling.

Discussion

Although mutual inhibition has been established as a front-back signaling network motif responsible for symmetry breaking, several unexplored questions have remained, including how the front and back modules vary with respect to one another and how cellular asymmetry is maintained despite those variations. To investigate these questions, we analyzed naturally occurring variation in the relations between downstream readouts of front (F-actin) and back (pMLC2) signaling observed within tens of thousands of individually polarized primary human neutrophils. We found (for three out of our four phenotype pairs) that back signaling is insulated across a wide range of naturally varying front signaling levels. However, disruption of microtubules by nocodazole revealed significant increases in anticorrelation and/or variability of back signaling localization with respect to front signaling. This result shows that front-back mutual inhibition operates as a core motif in microtubule-disrupted cells and that the presence of microtubules is required to insulate back polarity.

Microtubules are known to be essential for proper regulation of the back module. However, it has been unclear what signaling behaviors of the front and back module emerge from microtubule regulation of the back—or even whether this regulation is primarily activating [118, 148, 168] through mechanisms such as spatially localized microtubule delivery of GEFs [112] or whether this regulation is suppressing [168] through polymerized tubulin acting as a passive, global sink for GEFs. Our studies of natural variation in polarizing primary human neutrophils show that microtubules insulate

the localization but not the global intensity of pMLC2 signaling, with microtubules primarily activating rather than suppressing the back. Computational studies of a conceptual polarity circuit, in which microtubules are excluded by the front and transport Rho activators to the back, recapitulate the insulation that we experimentally observed. Together, these studies provide a model for how microtubules could mediate a positive, long-range link from front to back.

How does this specific role of microtubules fit in with previous reports of neutrophil chemotaxis after microtubule disruption? We note that, in our nocodazole-treated cells, we did not observe a global change in pMLC2 intensity after 3 min of fMLP exposure, whereas an increase was previously reported for RhoA-GTP after 1 min of fMLP exposure [168]. This may be due to our choice of a further downstream readout (pMLC2 versus RhoA-GTP) or our lower dose of nocodazole (9 μM) compared to higher [43] doses previously used (25 μM [161] or 20 mM [168]). Depolymerization of microtubules with a high dose of nocodazole could release a global "cloud" of activating GEFs, altering both the intensity and localization of front and back readouts. Such an alteration could produce a dramatic phenotype, but the cause of the phenotype may be hard to dissect because both sequestration and delivery would be simultaneously lost.

Does the addition of a positive, long-range front-to-back link to the neutrophil core polarity motif provide a general solution to insulate back signaling? Could other combinations of links provide similar insulating? Previous systematic searches through network topologies have provided a powerful approach for identifying network design

principles and guiding future experimental searches [43, 89, 150]. Our computational studies predicted that the addition of a long-range front-to-back link insulates back localization from variation of front activity and that other topologies that insulate back signaling also contain this link. Importantly, in the absence of a long-range front-to-back link, back signaling was predicted to be anticorrelated with front signaling, which is not experimentally observed in control neutrophils but is observed in microtubule-disrupted neutrophils. The complete set of signaling components and measured parameters responsible for this phenomenon are not yet fully known. Thus, the modeling approach we took was conceptual. More refined models, incorporating larger numbers of components and measured parameters, can be used in the future to guide experimental investigations of mechanisms in neutrophils as well as in other cell types that create spatially segregated signaling domains through mutual inhibition.

The design of a molecular network constrains signaling behaviors. Here, in polarized human neutrophils, we have taken a reverse-engineering approach: we inferred network topology by observing cell-to-cell variation and asking which networks permit observed ranges of behavioral variability. Such analysis may reveal trends that may not be visible by studying one component alone, one phenotype alone, or population averages. Similar reverse-engineering analyses will be useful for identifying core network motifs operating in other biological systems and understanding their behavioral consequences.

Materials and methods

Isolation of primary neutrophils from human blood

Human neutrophils were isolated as previously described [11]. In brief, neutrophils from venous blood of a single healthy donor were purified by dextran sedimentation and density-gradient centrifugation with Ficoll (GE Healthcare; #17-5442-02). Contaminating red blood cells were removed by hypotonic lysis.

Chemotactic assay for drug-treated cells

Purified human neutrophils were plated into 96-well Nunc glass plate (Fisher; #12-566-35), precoated with fibronectin (BD Bioscience; #354008), at a density of ~10,000 cells per well. Cells were incubated at 37°C with 5% CO_2 for 20 min before adding drugs. The concentrations for each drug were as follows: 9 μM for nocodazole (Sigma-Aldrich; M1404), 5 μM for taxol (Sigma-Aldrich; T1912), 20 μM for vinblastine (Sigma-Aldrich; V1377), and 10 μM for Akti (Fisher; #124018). These concentrations were chosen based previous titration curves [76], performed to determine the lowest dose at which a noticeable change was seen in the drug target. All experiments had multiple repeats (nocodazole, n = 10; taxol, n = 6; vinblastine, n = 6; Akti, n = 6) that were performed on at least 3 different days, including four repeats on a single day for each condition. Each replicate experiment had two replicate wells, which were pooled for subsequent analysis. After incubation with drugs for 30 min at room temperature (RT), cells were uniformly stimulated with 10 nM fMLP for 2 or 3 min at 37°C before formaldehyde fixation.

Immunofluorescence assay

Human neutrophils were fixed and permeabilized after fMLP stimulation. The primary antibodies, anti-pMLC2 (Cell Signaling Technology; #3675) and anti-α-tubulin (Cell Signaling Technology; #2144), were added to each well for overnight incubation at 4°C. After three washes, cells were incubated with secondary antibodies conjugated with Alexa Fluor 488 (Invitrogen; A11055) and Alexa Fluor 546 (Invitrogen; A10040) for 2 hr at RT to fluorescently label pMLC2 and α-tubulin, respectively. To label F-actin and DNA, cells were incubated with Alexa Fluor 647-conjugated phalloidin (Invitrogen; A22287) and Hoechst 33342 (Invitrogen; H1399), respectively, for 30 min at room temperature followed by three washes.

Image acquisition for fixed-cell assay

All fluorescence images were acquired using a BD Pathway 855 Bioimager (BD Biosciences) equipped with laser autofocus system, Olympus 40× objective lens, and high-resolution Hamamatsu ORCA ER CCD camera using 1 × 1 camera binning. Image acquisition was controlled by AttoVision v.1.5 (BD Biosciences).

Image quality control

We manually inspected all fluorescence images and discarded those presenting obvious anomalies (e.g., focus issues and abnormal fluorescence staining). Images with

poorly segmented cells were resegmented with manually optimized segmentation parameters.

Identification of cellular regions

Image background correction was done using the National Institutes of Health ImageJ software [134]. Cellular regions were determined using a watershed-based segmentation algorithm that first retrieved nuclear regions using DNA staining, and then combined multiple cytosolic region markers to identify cellular boundaries. To account for the polymorphonuclear nature of neutrophil nuclei, we used a segmentation algorithm that automatically merged multiple segmented regions into one cell to avoid oversegmentation [75]. Cellular regions located at the edge of an image or sharing long boundaries with neighbor cells were also discarded to avoid erroneous characterization of polarization patterns.

Supplementary methods

Validation of drug-response synchrony

To capture response synchrony (**fig. 2.S2A**), freshly harvested human neutrophils were plated into 96-well Nunc glass plates pre-coated with fibronectin. Cells were incubated at 37°C for 20 min followed by 30 min treatment with nocodazole or DMSO at room temperature before imaging under a Nikon Ti-E inverted microscope (Nikon) equipped with a Nikon Plan Apochromat 20x objective lens, Photometrics Cool-SNAP HQ camera using 1x1 camera binning, and Nikon Elements software. A temperature-control chamber set at 37°C with 5% CO_2 was installed on the microscope for live-cell imaging. After addition of 10 nM fMLP, differential interference contrast images of cells were captured for 3 minutes at 6-second intervals.

To track morphology of individual neutrophils during polarization, manual segmentation was performed using Fiji TrakEM2 plug-in [17, 133, 129]. We followed cells from all locations in the image that satisfied the following criteria: (i) the entire cell remained visible across all movie frames; and (ii) the cell was not in a crowded area with many neighbors that could affect its morphological change and motility. After determining the location of a cell (by identifying its boundary) across all time frames, we extracted the coordinates of its geometric center.

To verify that increased phenotypic variability in nocodazole-treated cells was not simply due to uneven responses to drug treatment, control and nocodazole-treated cell

populations were partitioned into *p* equal-size bins of increasing total microtubule intensity. The coefficient of variation for each phenotype was then computed within each partitioned group. In general, the coefficients of variation for almost all phenotypes were higher for the nocodazole-treated population than the control population, regardless of the number *p* of groups into which the cells were partitioned (**fig. 2.S2B**).

Z-sections of polarized neutrophils

To confirm that the spatial pattern of both front and back readout markers in epifluorescent images are representative of their actual distribution inside the whole cell, confocal images were taken at sequential z-sections with 2μm intervals from the top to bottom of each sample (**Fig. 2.S2C**). We observed that most of the signal was concentrated within the region z_3 to z_5 (central sections of the cell) where epifluorescent images are normally taken.

Cellular Feature Extraction

Single-cell analysis was performed on thousands of cells (**Table 2.1**). For each segmented cellular region and readout for front (F-actin) or back (pMLC2), we extracted the average intensity and the spreadness. Average intensity was defined as the sum of all pixel values within a cell, divided by the area of that cell [75, 76]. Spreadness was defined based on the average pairwise distances among the brightest pixels, D_α, as defined in previous work [75]. After visually inspecting images of fMLP-stimulated neutrophils, we empirically defined spreadness of F-actin based on the top 10% brightest

pixels, as these most closely matched the size of the F-actin enriched region. Similarly, we used the top 25% brightest pixels to define spreadness of pMLC2. To normalize spreadness, we defined its upper and lower bounds, s_U and s_L, respectively. The variable s_U is the average distance among the same number of pixels uniformly distributed along the cellular boundary. On the other hand, s_L is the average distance among the same number of pixels when they are all clustered together. For simplicity, we estimated s_L by arranging the pixels as much as possible into a square form. The normalized spreadness was computed as:

$$s = \frac{(D_\alpha - S_L)}{(S_U - S_L)}.$$

Computing slope and variability of back versus front phenotypes

Given a pair of front and back phenotypes, p_F and p_B, cells were sorted by increasing values of p_F and partitioned into Q (=5) bins (m_1, m_2, ..., m_Q) with equal numbers of cells. This process was repeated for each of the R replicate experiments per condition:

$$\left(m_1^{(r)}, m_2^{(r)} \cdots m_Q^{(r)}\right) for\ r = 1 \ldots R$$

The bins were normalized so that the middle (third) bin had unit value:

$$m_q^{(r)} \rightarrow \frac{m_q^{(r)}}{m_{\frac{Q}{2}}^{(r)}} \text{ for } q = 1 \ldots Q,\ r = 1 \ldots R$$

For slope, the mean value of each bin was computed, and the MATLAB built-in function "regress.m" was then used to compute a regression line through these means.

We estimated variability by (1) sorting all values by their height difference to the regression line; (2) shifting the height of the best-fitting regression line up or down to coincide with the two data points at the 90th or 10th percentiles of this height measure, respectively; then (3) reporting the height difference between the two shifted lines.

Mathematical model of the core polarity network

Our model used mass-conserved, reaction-diffusion equations, modified from a previously proposed [116] mathematical model based on Bourne's qualitative model of neutrophil polarization by mutual inhibition between divergent "front" and "back" pathways [167]:

$$\frac{\partial u_1}{\partial t} = D_1 \frac{\partial^2 u_1}{\partial x^2} + k_{a1} u_2 - k_{i1} u_1 - k_{13} u_1 u_3 + k_{11} S u_1 u_2 + k_{S1} S u_2$$

$$\frac{\partial u_2}{\partial t} = D_2 \frac{\partial^2 u_2}{\partial x^2} - k_{a1} u_2 + k_{i1} u_1 + k_{13} u_1 u_3 - k_{11} S u_1 u_2 - k_{S1} S u_2$$

$$\frac{\partial u_3}{\partial t} = D_3 \frac{\partial^2 u_3}{\partial x^2} + k_{a3} u_4 - k_{i3} u_3 - k_{31} u_1 u_3 + k_{S3} S u_4$$

$$\frac{\partial u_4}{\partial t} = D_4 \frac{\partial^2 u_4}{\partial x^2} - k_{a3} u_4 + k_{i3} u_3 + k_{31} u_1 u_3 - k_{S3} S u_4$$

where variables were defined as follows:

S: stimulus concentration

u_1: concentration of active front signaling component

u_2: concentration of inactive front signaling component

u_3: concentration of active back signaling component

u_4: concentration of inactive back signaling component

D_1, ... , D_4: the diffusion coefficient for these four signaling components

k_{i1}: deactivation rate of front signaling component

k_{i3}: deactivation rate of back signaling component

k_{S1}: activation rate of front signaling component

k_{S3}: activation rate of back signaling component

k_{11}: positive feedback rate of front signaling component

k_{13}: inhibition rate of front module by back module

k_{31}: inhibition rate of back module by front module

Mathematical model of microtubule-mediated activation of back module

To test the sufficiency of microtubule-mediated transport of back-activators, the above core model was extended to an "M-network" via the modifications below:

$$\frac{\partial u_1}{\partial t} = D_1 \frac{\partial^2 u_1}{\partial x^2} + k_{a1} u_2 - k_{i1} u_1 - k_{13} u_1 u_3 + k_{11} S u_1 u_2 + k_{S1} S u_2$$

$$\frac{\partial u_2}{\partial t} = D_2 \frac{\partial^2 u_2}{\partial x^2} - k_{a1} u_2 + k_{i1} u_1 + k_{13} u_1 u_3 - k_{11} S u_1 u_2 - k_{S1} S u_2$$

$$\frac{\partial u_3}{\partial t} = D_3 \frac{\partial^2 u_3}{\partial x^2} + k_{a3} u_4 - k_{i3} u_3 - k_{31} u_1 u_3 + k_{S3} S u_4 + k_M M u_4$$

$$\frac{\partial u_4}{\partial t} = D_4 \frac{\partial^2 u_4}{\partial x^2} - k_{a3} u_4 + k_{i3} u_3 + k_{31} u_1 u_3 - k_{S3} S u_4 - k_M M u_4$$

Here, the microtubule-mediated back activation, *M*, was defined by:

$$M(x; t, \sigma, \alpha, \lambda, \theta, u_1(x,t)) = \sum_{n=1}^{N_{MT}} \exp\left(- \left(\frac{\mathrm{mod}\left(x - x_n(t), \frac{L}{2} \right)^2}{2\sigma^2} \right) \right)$$

where variables were defined as follows:

N_{MT}: number of microtubule cables, set initially at 30, and randomly varied from 5-60, based on reports that the number of microtubules in polarizing human neutrophils varies from 25-40 [32, 132].

k_M: strength of microtubule-mediated back activation

σ: extent of local activation of the back signaling circuit by each individual microtubule tip. (The zone of activation was modeled by a Gaussian distribution, centered on the location of the microtubule tip, and σ was defined as the standard deviation of that distribution.)

λ: fall-off rate (modeled exponentially) of microtubules from their sites of attachment

δ: minimum distance between microtubule tips

θ: nonlinearity exponent of the actin-driven exclusion of microtubules from the

front of the cell

General network topology search

The mathematical model was further modified to include long-range, activating links. Links could be "direct," modeled into "D-networks" with the below equations:

$$\frac{\partial u_1}{\partial t} = D_1 \frac{\partial^2 u_1}{\partial x^2} + k_{a1} u_2 - k_{i1} u_1 - k_{13} u_1 u_3 + k_{11} S u_1 u_2 + k_{S1} S u_2 + \eta k_{153} U_3 u_2$$

$$\frac{\partial u_2}{\partial t} = D_2 \frac{\partial^2 u_2}{\partial x^2} - k_{a1} u_2 + k_{i1} u_1 + k_{13} u_1 u_3 - k_{11} S u_1 u_2 - k_{S1} S u_2 - \eta k_{153} U_3 u_2$$

$$\frac{\partial u_3}{\partial t} = D_3 \frac{\partial^2 u_3}{\partial x^2} + k_{a3} u_4 - k_{i3} u_3 - k_{31} u_1 u_3 + k_{33} S u_3 u_4 + k_{S3} S u_4 + \eta k_{351} U_1 u_4$$

$$\frac{\partial u_4}{\partial t} = D_4 \frac{\partial^2 u_4}{\partial x^2} - k_{a3} u_4 + k_{i3} u_3 + k_{31} u_1 u_3 - k_{33} S u_3 u_4 - k_{S3} S u_4 - \eta k_{351} U_1 u_4$$

$$U_1 = \int_{\Omega} u_1 dx$$

$$U_3 = \int_{\Omega} u_3 dx$$

(where k_{351} is the front-to-back activation rate, k_{153} is the back-to-front activation rate, and η is a scalar controlling the strength of the link)

or "indirect," through a fast-diffusing intermediate, and modeled into "I-networks" as below:

$$\frac{\partial u_1}{\partial t} = D_1 \frac{\partial^2 u_1}{\partial x^2} + k_{a1} u_2 - k_{i1} u_1 - k_{13} u_1 u_3 + k_{11} S u_1 u_2 + k_{S1} S u_2 + \eta k_{15} u_5 u_2$$

$$\frac{\partial u_2}{\partial t} = D_2 \frac{\partial^2 u_2}{\partial x^2} - k_{a1} u_2 + k_{i1} u_1 + k_{13} u_1 u_3 - k_{11} S u_1 u_2 - k_{S1} S u_2 - \eta k_{15} u_5 u_2$$

$$\frac{\partial u_3}{\partial t} = D_3 \frac{\partial^2 u_3}{\partial x^2} + k_{a3} u_4 - k_{i3} u_3 - k_{31} u_1 u_3 + k_{33} S u_3 u_4 + k_{S3} S u_4 + \eta k_{35} u_5 u_4$$

$$\frac{\partial u_4}{\partial t} = D_4 \frac{\partial^2 u_4}{\partial x^2} - k_{a3} u_4 + k_{i3} u_3 + k_{31} u_1 u_3 - k_{33} S u_3 u_4 - k_{S3} S u_4 - \eta k_{35} u_5 u_4$$

$$\frac{\partial u_5}{\partial t} = D_5 \frac{\partial^2 u_5}{\partial x^2} + k_{51} u_1 + k_{53} u_3 - k_{i5} u_5$$

where variables are defined as:

u_5: concentration of the fast-diffusing intermediate

D_5: diffusion rate of the intermediate

k_{i5}: deactivation rate of the intermediate

k_{15}: activation rate of the front by the intermediate

k_{51}: activation of the intermediate by the front

k_{35}: activation of the back by the intermediate

k_{53}: activation of the intermediate by the back

Simulation based on these equations allowed systematic assessment of the insulation performance of different network topologies.

Figures

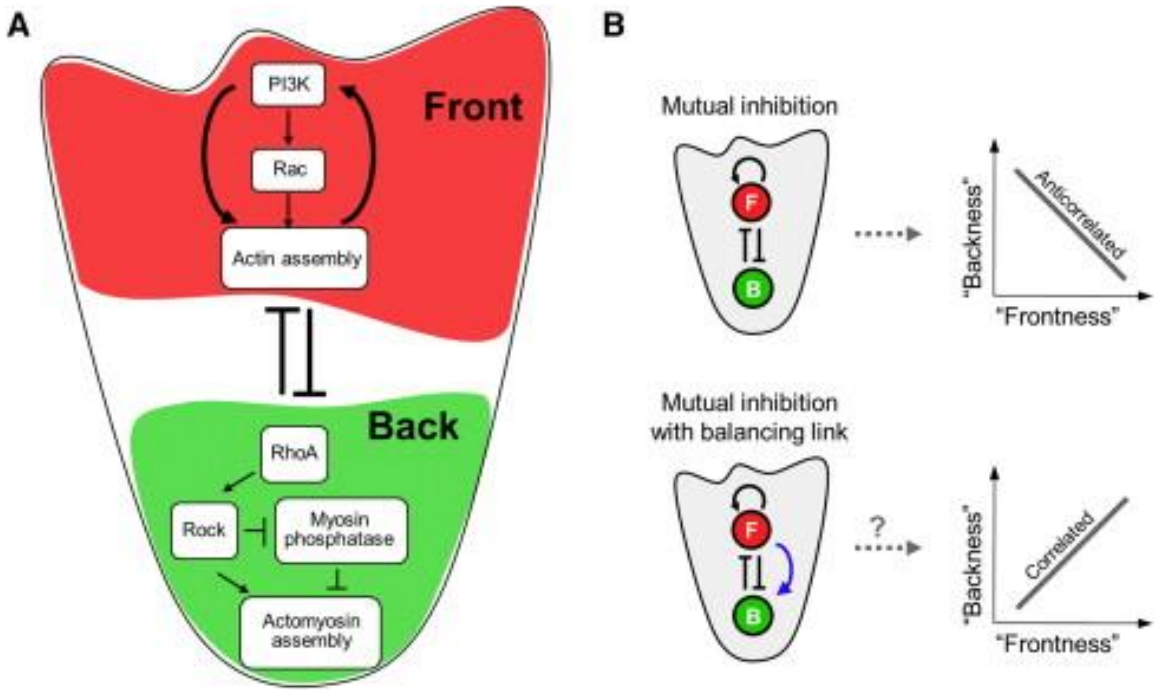

Figure 2.1. Neutrophil polarity network. (**A**) Simplified schema of the core neutrophil network motif of mutual inhibition between the front (red-shaded region) and back (green-shaded region) signaling modules together with positive feedback at the front. (**B**) Cartoon illustration of potential relationships between front (F) and back (B) signaling for the core network motif without (top) or with (bottom) a long-range positive link from front to back (blue arrow).

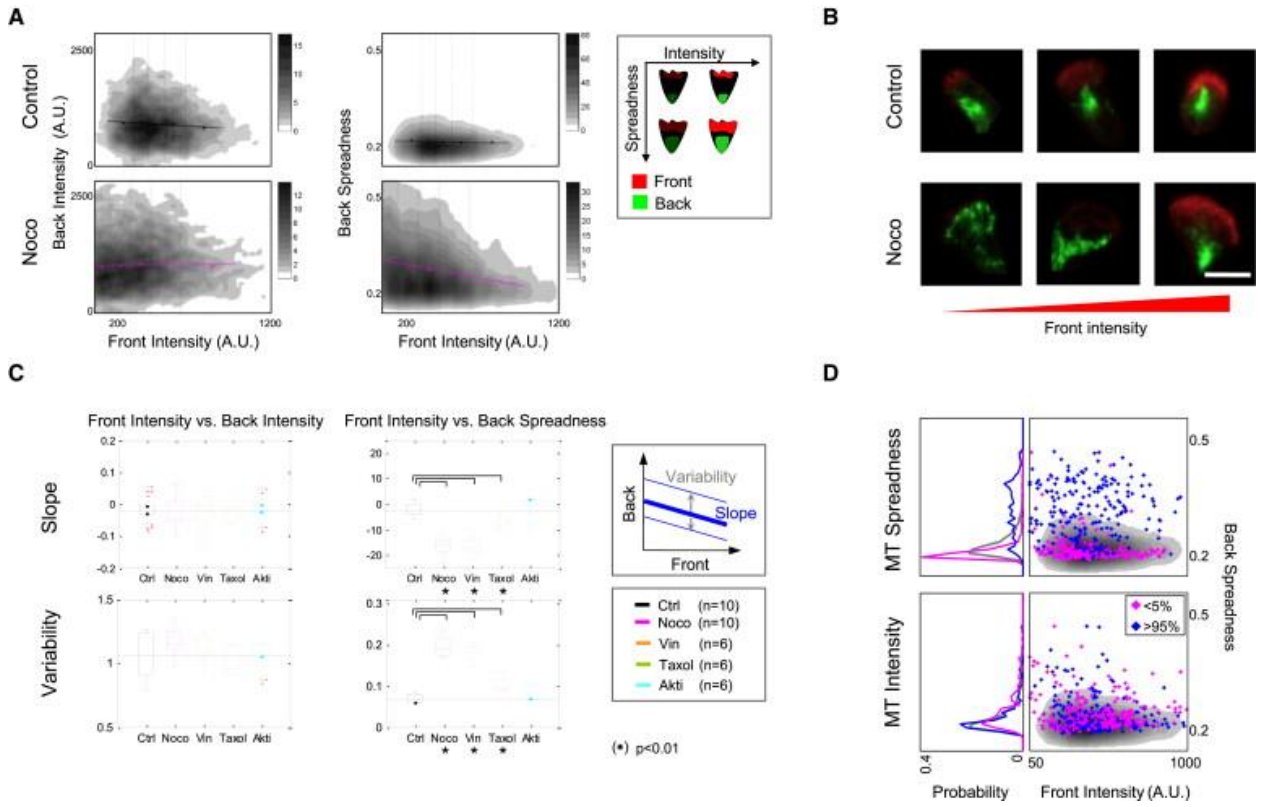

Figure 2.2. Microtubules insulate back pMLC2 localization against varying front F-actin levels in polarized human neutrophils. (**A**) Density plots suggest that depolymerization of microtubules with nocodazole (Noco) reduces the ability of back spreadness to be insulated from changes in front intensity in fMLP-stimulated human neutrophils. (**B**) Representative images of neutrophils treated with or without nocodazole (left to right, low-to-high F-actin intensity). Red indicates F-actin, and green shows pMLC2. Scale bar, 10 μm. (**C**) Summary of regression slope (top) and variability (bottom) between front intensity and back spreadness in replicates of control (Ctrl) and drug-treated cells. Box plots illustrate median values (center lines) and 25th and 75th percentiles (box edges) across replicate experiments. The vertical lines extend to the most extreme data points not

considered outliers (minima and maxima whiskers). Outliers are plotted individually (red "+"). $^{*}p < 0.01$, Wilcoxon's two-sided rank sum test. Vin, vinblastine. (**D**) Density plots (right column) of non-drug-treated control cells (as in A, top right) overlaid with scatterplot of cells ranked in the bottom 5% (magenta points) or top 5% (blue points) based on intensity (bottom) or spreadness (top) of microtubule staining (MT). Probability plots (left column) reflect densities of scatterplots at right. Gray curve reflects overall population density.

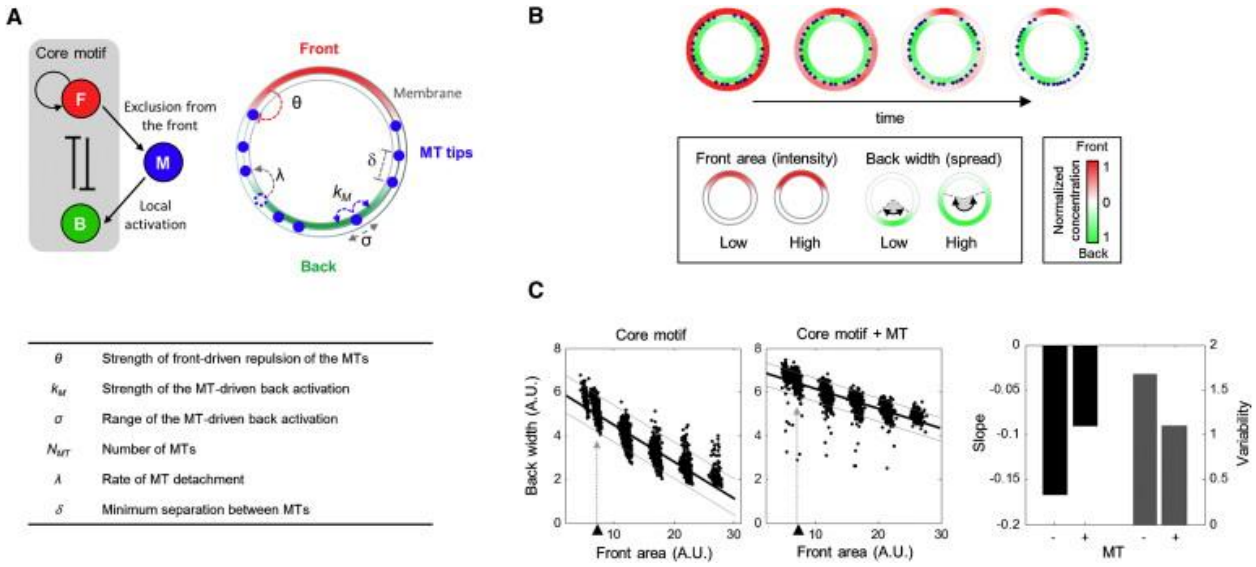

θ	Strength of front-driven repulsion of the MTs
k_M	Strength of the MT-driven back activation
σ	Range of the MT-driven back activation
N_{MT}	Number of MTs
λ	Rate of MT detachment
δ	Minimum separation between MTs

Figure 2.3. A mathematical model of microtubule interactions with front and back modules reveals a role for insulating localization of back signaling. (**A**) Illustration of the neutrophil polarity model featuring interactions among front (red), back (green), and microtubules (M; blue). Top-left view shows that two additional interactions were added to the "core" motif accounting for the exclusion of microtubules from the front and

microtubule-mediated activation of the back. Top-right view and table present the parameters used to model microtubule-mediated front-to-back interaction. (**B**) Sample outcome of polarization from simulated model. Cell membrane is visualized with an annulus; blue dots represent the location of microtubule tips on the membrane. Red and green indicate spatial distribution of active front and back components, respectively. For visualization, the maximum values of front and back concentrations are both normalized to one. For each polarized cell, the front area and back width were measured as proxies of the front intensity and back spreadness. (**C**) Scatterplots of back width versus front area obtained by sampling parameters. Top-left and middle panels are without and with microtubules, respectively. Thick black lines represent regression lines. Lower and upper gray lines indicate variability around regression line. Triangles and dotted lines refer to data points obtained by varying the front amount around its nominal value. Bar graph illustrates regression slope and variability of back width versus front area.

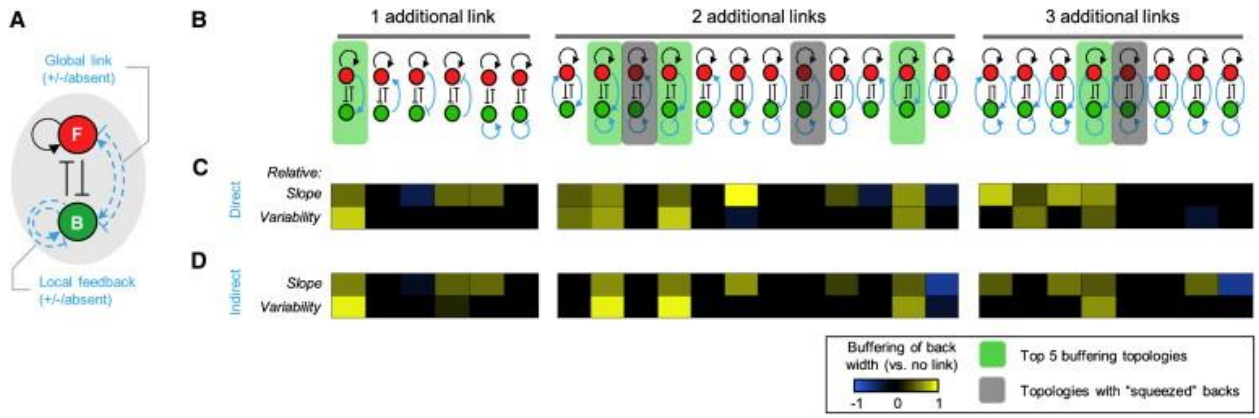

Figure 2.4. Systematic assessment of the performance of different polarity network topologies in insulating the localization of back signaling. (**A**) Set of possible additional links (blue dashed lines) to the core topology (black lines). (**B**) Schema of additions including one, two, or three positive or negative links. (**C and D**) Heatmap of changes to the insulation performance upon addition of direct (C) or indirect (D) links. The heatmap color scale illustrates the change to the insulation between the new and the original topologies (i.e., link versus no link). Cyan or yellow indicates decreased or increased, respectively, insulation capability compared to the core topology. Green-shaded background shows topologies with the best overall insulation performance for both direct and indirect model implementations. Gray-shaded background presents topologies where the back was excessively "squeezed" into a narrow region.

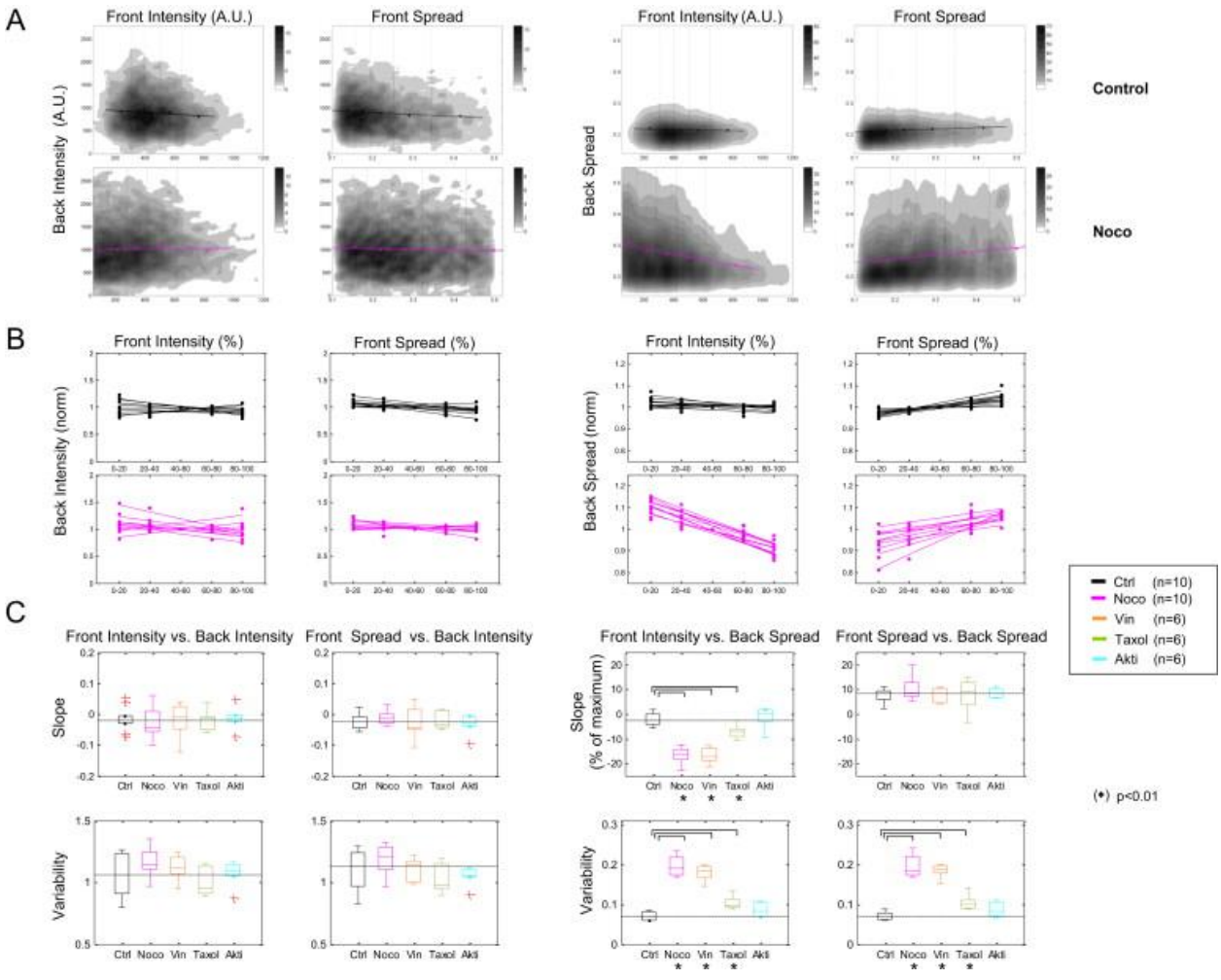

Figure 2.S1. Back signaling is constant across a wide range of front readouts. (**A**) Density plots (using MATLAB function scattercloud.m) of the front-versus-back feature distribution in fMLP-stimulated (10 nM, 2-3min) neutrophils for different combinations of cellular phenotypes. We examined the intensity and the spreadness of F-actin (readout for the front) and pMLC2 (readout for the back). Data outside the 1-99th percentile range were discarded. Cells were partitioned into five equal-size groups with increasing front phenotype. Average values of back phenotypes were plotted for each group and fitted by

a regression line as in Fig. 2.2A. (**B**) Regression lines between different pairs of front/back phenotypes across replicate experiments, normalized to have the center mean equal to one. Black/magenta: control and nocodazole-treated conditions. (**C**) Distribution of the regression slope and variability between different pairs of front/back phenotypes across control and drug conditions. Boxes and vertical lines are defined as in Fig 2.2C. (+): outliers. (*) Wilcoxon's two-sided rank sum test p-value < 0.01 against the control condition.

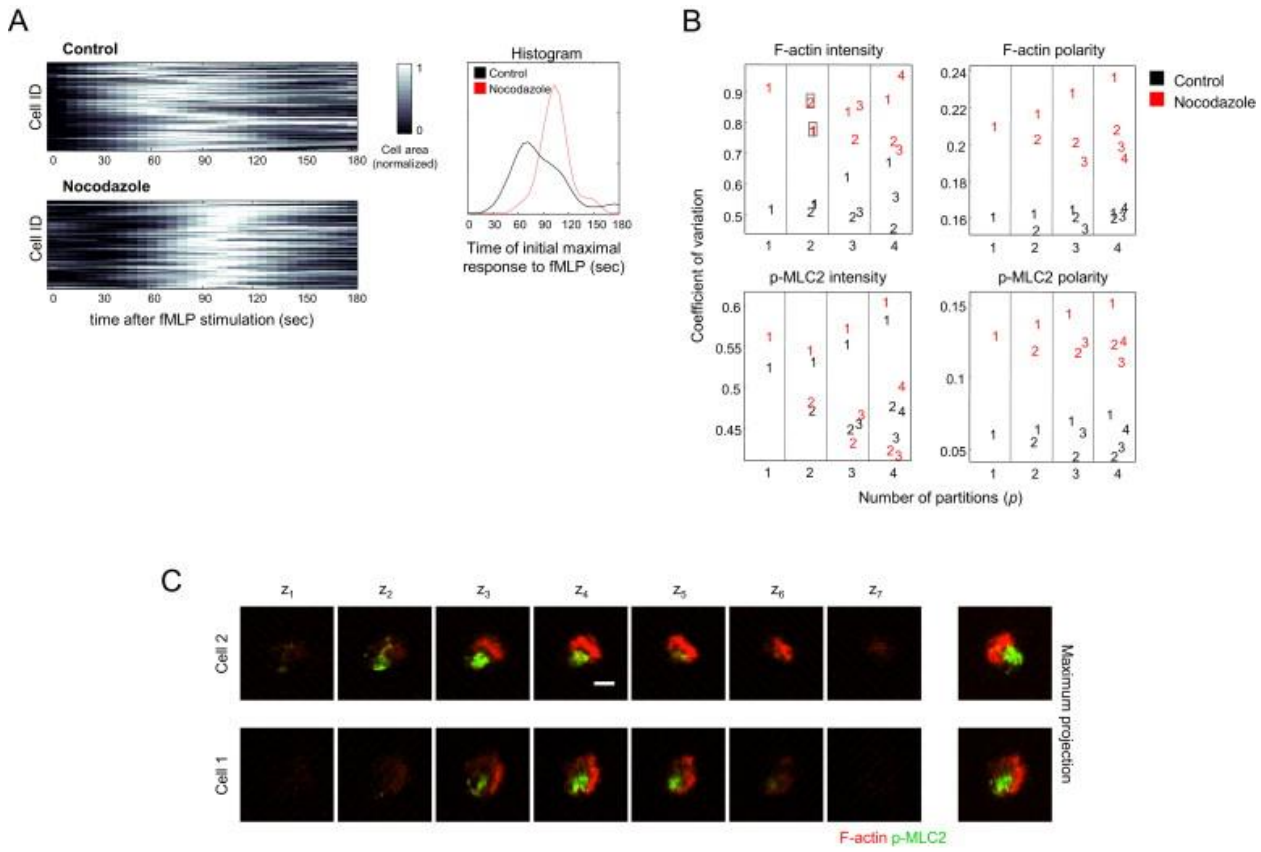

Figure 2.S2. Validation of response synchrony and microscopy methods. (**A**) Characterization of response synchrony among primary human neutrophils to fMLP stimulation. (Left) Upon fMLP (10 nM) stimulation, the cell area of individual cells was tracked over time as a readout of chemotactic response. Each row corresponded to the normalized area of a given neutrophil over time (observed at 6 s intervals). Each time series was smoothed using the MATLAB built-in function *smooth.m*. Top: control; bottom: nocodazole. Each condition was repeated twice. (Right) Histogram of the time points of maximal response to fMLP stimulation (maximal cell area) under each of the two conditions. (**B**) Increased phenotypic variability in nocodazole-treated cells was not

due to potential unevenness of responses to drug treatment. Control and nocodazole-treated populations of polarized human neutrophils were partitioned into equal-size bins with increasing levels of total microtubule intensity. Four readouts were examined in these cells: F-actin average intensity, F-actin polarity, pMLC2 average intensity and pMLC2 polarity. The coefficient of variation for each phenotype was then computed within each partitioned group, under both nocodazole-treated (red) and control (black) conditions. We tested four values of *p*, from one to four (e.g., two framed red numbers in left-most figure, p = *2*). When nocodazole-treated cells were partitioned into two groups (two framed red numbers; p = 2), the coefficient of variation of F-actin intensity was approximately 0.79 within the first group (lower microtubule intensity) and 0.88 within the second group (higher microtubule intensity). In general, the coefficients of variation for almost all readouts were higher in nocodazole-treated conditions (red) than in control conditions (black) regardless of the grouping of cells. (**C**) Z-sections of polarized human neutrophils stained with front and back readout markers. Human neutrophils were fixed and stained with phalloidin (for F-actin, red) and anti-pMLC2 antibodies (for pMLC2, green) after 3 min fMLP stimulation. Confocal images were taken at sequential z-sections with 2 μm intervals from top to bottom. Rightmost column: maximum projection across all z-sections. Scale bar: 5 μm.

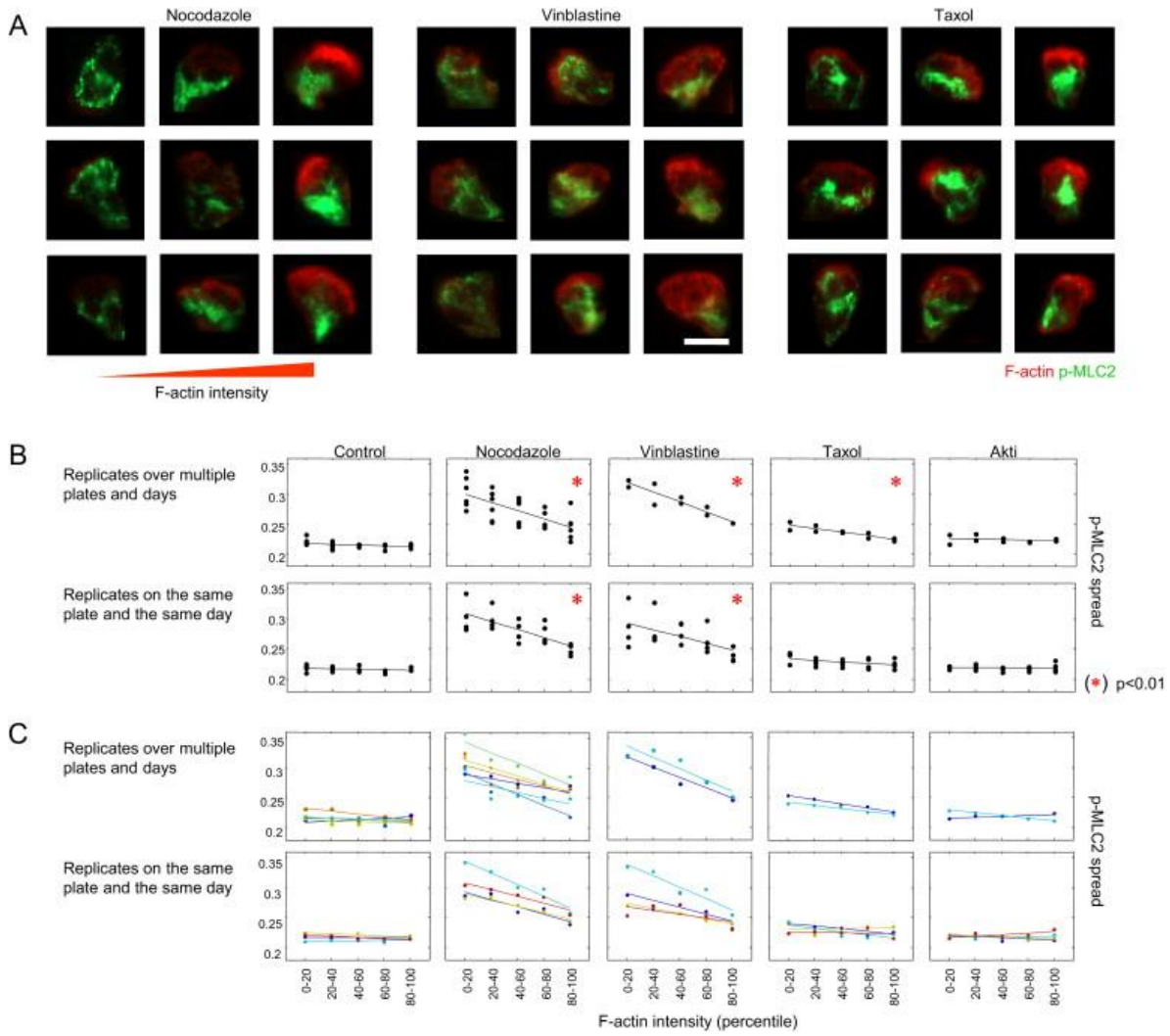

Figure 2.S3. Replicates of different drug-treatment conditions. (**A**) Representative images of neutrophils treated with different microtubule-inhibiting drugs. Left/middle/right panel: nocodazole/vinblastine/taxol. Each panel contains three columns of images illustrating cells with low (left), intermediate (middle) or high (right) level of F-actin intensity (columns: three representative images per condition). Scale bar: 10 μm. (**B** and **C**) Results of analyzing replicates obtained across different days versus a single day are compared. For each condition and replicate experiment, cells were partitioned

into five groups based on the average F-actin intensity. The average value of pMLC2 spread was plotted for each partitioned group. Results of regression are shown for all data points pooled together (B) and for individual replicates (C). Top row: replicates data gathered over multiple days. Bottom row: replicates data generated on the same day from one single imaging plate. From left to right: control, nocodazole, vinblastine, taxol and Akt inhibitor (Akti). Dots: mean feature value within each group of cells; different colors indicate individual replicates. Lines: linear regression computed using MATLAB function *regress.m*. Stars: statistical significance of linear regression (versus no trend) with p-value < 0.01.

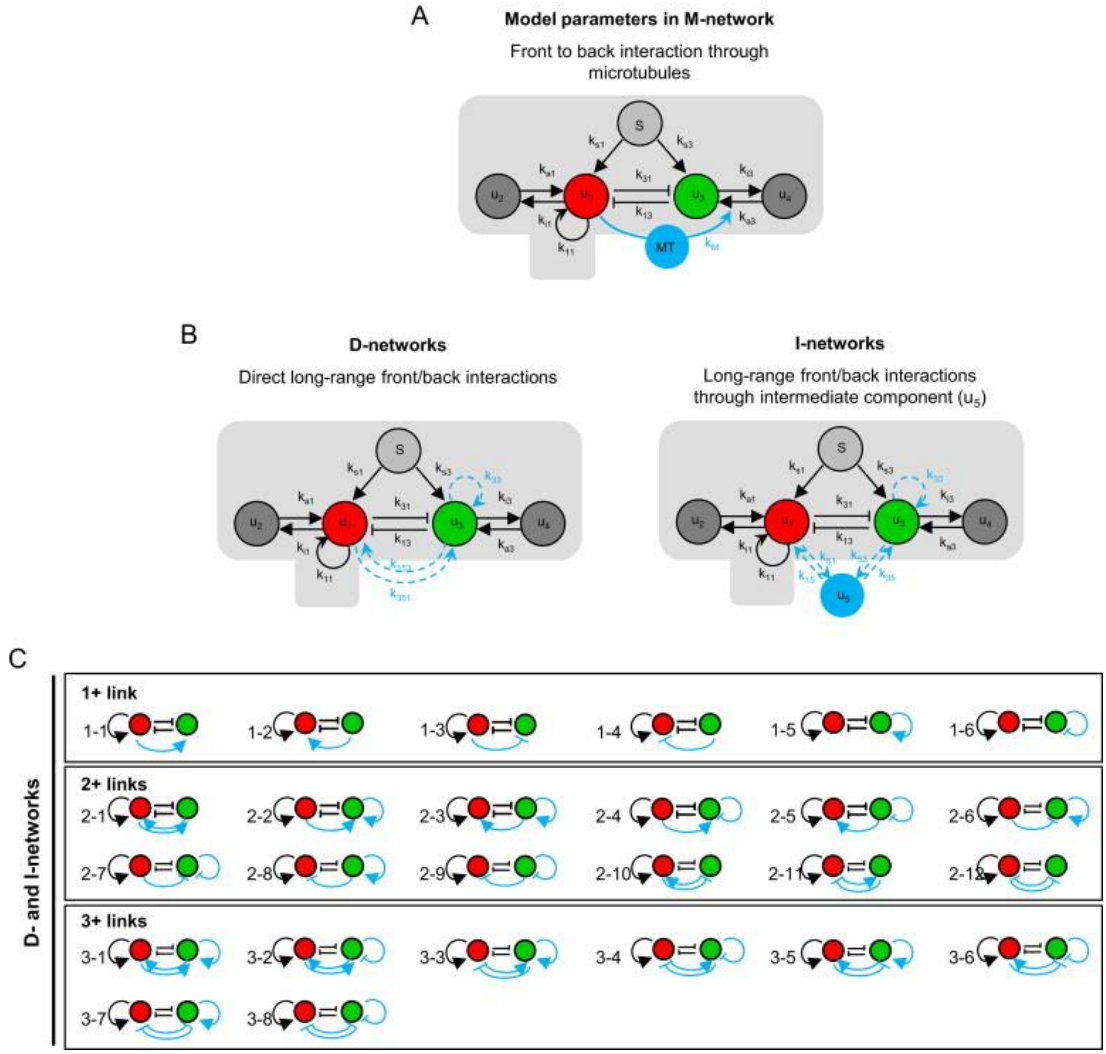

Figure 2.S4. Schema of different network topologies used in studies. (**A**) Microtubule-mediated front-to-back detailed model (M-network). (**B**) General network topologies with Direct (D-model) or Indirect (I-model) links between front and back. A-B: Gray shaded background: core motif (reference model). Blue links: additional local feedback or long-range front/back interactions. S: stimulation; u_1,u_2: active/inactive front components;

u_3,u_4: active/inactive back components; u_5: intermediate component. The long-range interactions between the active front and back components were implemented either through direct interaction (left, D-networks) or indirect interaction via a fast-diffusing intermediate component (right, I-networks). (**C**) Incremental network configurations generated by adding one or more links to the reference model in D- and I-networks. For simplicity, the inactive components, the stimulation and the associated interactions were not drawn.

Tables

Table 2.1. Total numbers of cells analyzed per condition.

Fixed cell assay	Nocodazole	Taxol	Vinblastine	Akti	Control
Multiple days	6915	2600	2253	2892	12207
Single day	1646	1206	1308	1376	1816
Live cell assays	Control	Nocodazole			
Multiple days	75	119			

Table 2.2. Nominal parameter values used in the polarity models.

(i)	Parameter	Interpretation	Value	Reference/Basis
	S_0	Offset (basal level) of the stimulation profile	0.4 (A.U.)	[Otsuji, PLoSCompBio2007]
	L	Cell size (perimeter)	10μm	[Otsuji, PLoSCompBio2007]
	Δx	Difference interval in space	0.1μm	Empirically selected
	Δt	Difference interval in time	0.04s	Empirically selected
	D_1, D_3	Diffusion rate of membrane (active) species	$0.04\mu m^2/s$	[Otsuji, PLoSCompBio2007]
	D_2, D_4	Diffusion rate of cytosolic (inactive) species	$3\mu m^2/s$	[Otsuji, PLoSCompBio2007]
	u_2	Total amount of front component	1 (A.U.)	[Otsuji, PLoSCompBio2007]
	u_4	Total amount of back component	0.6 (A.U.)	[Otsuji, PLoSCompBio2007; Michaelson, JCB2001]
	k_{S1}	Stimulation-driven front activation rate	$1s^{-1}$	[Otsuji, PLoSCompBio2007]
	k_{S3}	Stimulation-driven back activation rate	$1s^{-1}$	[Otsuji, PLoSCompBio2007]
	k_{a1}	Front activation rate	$0.2s^{-1}$	[Otsuji, PLoSCompBio2007]
	k_{i1}	Front deactivation rate	$0.4s^{-1}$	[Otsuji, PLoSCompBio2007]
	k_{a3}	Back activation rate	$0.2s^{-1}$	[Otsuji, PLoSCompBio2007]
	k_{i3}	Back deactivation rate	$0.4s^{-1}$	[Otsuji, PLoSCompBio2007]
	k_{13}	Local back-to-front inhibition rate	$3s^{-1}$	Empirically selected
	k_{31}	Local front-to-back inhibition rate	$3s^{-1}$	
	k_{11}	Local front positive feedback rate	$4s^{-1}$	[Otsuji, PLoSCompBio2007]
(ii)	D_5	Diffusion rate of the fast-diffusing intermediate component	$40\mu m^2/s$	Empirically selected
	u_5	Total amount of intermediate component	0.2 (A.U.)	Empirically selected
	k_{i5}	Deactivation rate of intermediate component	$0.2s^{-1}$	Empirically selected
	k_{33}	Local back positive feedback rate	$4s^{-1}$	[Otsuji, PLoSCompBio2007]
		Local back negative feedback rate	$-1s^{-1}$	Empirically selected
	k_{15}	Intermediate-to-front activation/inhibition rate	$\pm1.5s^{-1}$	Empirically selected
	k_{51}	Front-to-Intermediate activation/inhibition rate	$\pm1.5s^{-1}$	
	k_{35}	Intermediate-to-back activation/inhibition rate	$\pm1.5s^{-1}$	Empirically selected
	k_{53}	Back-to-Intermediate activation/inhibition rate	$\pm1.5s^{-1}$	
	k_{351}	"Direct" front-to-back activation/inhibition rate	$\pm0.3s^{-1}$	Empirically selected
	k_{153}	"Direct" back-to-front activation/inhibition rate	$\pm0.3s^{-1}$	
(iii)	N_{MT}	Number of microtubules	30	[Irimia, BioPhyJ2009; Schliwa, Cell1982]
	k_M	Strength of the MT-driven back activation	$1s^{-1}$	Empirically selected
	σ	Standard deviation of the MT-driven back activation zone	0.5μm	Equivalent of cytosolic 1-D diffusion rate ($\sim3\mu m^2/s$)
	δ	Minimum distance between adjacent MT tips	0.15μm	At least 45% coverage of the cell membrane
	λ	Microtubule fall-off rate	$0.1s^{-1}$	[Irimia, BioPhyJ2009]
	θ	Strength of the front-driven repulsion of the microtubules	2	Empirically selected

Table 2.3. Parameter ranges used when simulating natural variability.

		Interpretation	Nominal value	Variation range
Existing parameters	u_2	Total amount of front component	1 (A.U.)	0.817 – 1.225s^{-1}
	u_4	Total amount of back component	0.6 (A.U.)	0.490 – 0.735s^{-1}
	k_{S1}	Stimulation-to-front activation rate	1s^{-1}	0.817 – 1.225s^{-1}
	k_{S3}	Stimulation-to-back activation rate	1s^{-1}	0.817 – 1.225s^{-1}
	k_{a1}	Front activation rate	0.2s^{-1}	0.163 – 0.245s^{-1}
	k_{i1}	Front deactivation rate	0.4s^{-1}	0.327 – 0.490s^{-1}
	k_{a3}	Back activation rate	0.2s^{-1}	0.163 – 0.245s^{-1}
	k_{i3}	Back deactivation rate	0.4s^{-1}	0.327 – 0.490s^{-1}
	k_{11}	Local front positive feedback rate	4s^{-1}	3.266 – 4.899s^{-1}
	k_{13}	Local back-to-front inhibition rate	3s^{-1}	2.450 – 3.674s^{-1}
	k_{31}	Local front-to-back inhibition rate	3s^{-1}	2.450 – 3.674s^{-1}
	u_5	Total amount of intermediate component	0.2 (A.U.)	0.2 – 0.2
	k_{i5}	Deactivation rate of intermediate component	0.2s^{-1}	0.163 – 0.245s^{-1}
Additional parameters	k_{33}	Local back positive feedback rate	4s^{-1}	3.266 – 4.899s^{-1}
		Local back negative feedback rate	-1s^{-1}	-1.225 – -0.817s^{-1}
	k_{15}	intermediate-to-front activation rate	1.5s^{-1}	Interaction strength modulated by a multiplicative scalar s
		Inhibition rate	-1.5s^{-1}	
	k_{51}	front-to-intermediate activation rate	1.5s^{-1}	
		Inhibition rate	-1.5s^{-1}	
	k_{35}	intermediate-to-back activation rate	1.5s^{-1}	
		Inhibition rate	-1.5s^{-1}	
	k_{53}	back-to-intermediate activation rate	1.5s^{-1}	
		Inhibition rate	-1.5s^{-1}	
	k_{351}	direct front-to-back activation rate	0.3s^{-1}	
		Inhibition rate	-0.3s^{-1}	
	k_{153}	direct back-to-front activation rate	0.3s^{-1}	
		Inhibition rate	-0.3s^{-1}	

CHAPTER THREE

Concentration-dependent tuning of ERK dynamics in neutrophils and neutrophil-like HL-60 cells

For the final version of this work, please see: Zhang, E. R., Liu, S., Wu, L.F.*, Altschuler, S.J.*, Cobb, M.H.* Chemoattractant concentration–dependent tuning of ERK signaling dynamics in migrating neutrophils. Sci. Signal. 9.458 (2016): ra122-ra122.

Introduction

Neutrophil chemotaxis toward the bacterial peptide N-formyl-methionyl-leucyl-phenylalanine (fMLP) is a crucial process in the immune system's defense against invading bacteria. While navigating through an increasing gradient of fMLP, neutrophils switch from directional migration at low fMLP concentrations to circuitous migration at high fMLP concentrations [85]. The mitogen-activated protein kinases ERK1/2 have recently been implicated in switching fMLP-concentration-dependent migration from directional to circuitous [85]. However, the regulation and role of ERK in chemotactic neutrophils remain unclear.

Although it has long been established that ERK1/2 and p38 are activated downstream of fMLP binding to receptors FPR1 and FPR2 [28, 176, 35] , ERK1/2 have recently been reported to display an all-or-none, 'plateaued' activation profile [85] in response to increasing (50-1000 nM) concentrations of fMLP. Here, we conduct single-cell analysis across time and fMLP concentration to explore this apparent concentration-independence. In particular, such plateaued behavior could be due to bimodal activation

of the protein or due to saturation of the input signal. We find that ERK has gradated, rather than bimodal, responses to fMLP concentration, with saturation occurring at approximately 100 nM fMLP.

Recent controversy has further arisen over whether ERK1/2 are necessary for [103] or inhibit [85] neutrophil migration. Here, we use the specific inhibitors PD0325901 and SCH772984 [106] to demonstrate that ERK1/2 are absolutely required for neutrophil migration. Additionally, we show with VX-702 and BIRB-796 that p38 modulates the response of ERK to fMLP, but that p38 by itself is dispensable for directional migration. Together, our work demonstrates that fMLP activates ERK1/2 in gradated responses, that p38 modulates the decay of these responses back toward baseline, and that ERK1/2 support neutrophil chemotaxis toward fMLP.

Results

Neutrophil chemotaxis saturates at 100 nM fMLP

Previously, it has been found that neutrophil-like HL-60 cells are unable to complete migration through steep gradients of fMLP (500 nM and 1000 nM) [85]. However, the concentration of fMLP at which HL-60 cells ceased directional migration was not known. To answer this question, we visualized a gradient of a labeled fMLP derivative, fluorescein-formyl-Nle-Leu-Phe-Nle-Tyr-Lys, within the ibidi Chemotaxis^{3D} microfluidic device (**Fig. 3.1A** and **fig. 3.S1**). Known concentrations of the probe were imaged (**Fig. 3.1B**) to relate fluorescence to concentration (**Fig. 3.1C**). A 500 nM

gradient of fluorescein-formyl-Nle-Leu-Phe-Nle-Tyr-Lys across the observation chamber was then visualized over several hours and quantified (**Fig. 3.1D** and **fig. 3.S1A**). Tracks from microscopy videos of cells migrating in gradients of fMLP were overlaid on the visualized gradient of fluorescein-formyl-Nle-Leu-Phe-Nle-Tyr-Lys (**Fig. 3.1E**), using the distinctive ends of the observation area as fiducials (**Fig. 3.1A**). We found that cells cease directional migration well within the 3-hour interval of live-cell imaging, and that the concentration of fMLP at which they wander circuitously is approximately 100 nM fMLP (**Fig. 3.1E** and **fig.3. S1B**).

ERK1/2 have graded responses to fMLP concentration, with concentration-dependent decay

A confounding factor in studying HL-60 chemotaxis within a gradient is that both of the parameters of concentration and time vary as a cell migrates (**Fig. 3.1F**). To disentangle these two variables, we exposed cells to a range of uniform concentrations of fMLP, and observed the consequences of this stimulation at various times between 0 and 10 minutes (**Fig. 3.2A**, and **fig. 3.S2A**). Concentrations of 10, 100, and 500 nM were chosen based on the result that cells lose directionality at about 100 nM fMLP, and the fact that the formyl peptide receptors FPR1 and FPR2 have dissociation constants of 10 nM and ~500 nM fMLP, respectively [169]. Consistent with previous studies, the morphological polarity of the cells plateaued [76, 152] within this timeframe (Fig. 2B), and the ERK response saturated at 100 nM at the single timepoint of 2 minutes (that is, the peak ERK response was the same for 500 nM as 100 nM) [85]. However, response

behaviors beyond 2 minutes were not so simple. Notably, the ERK responses at 10 minutes were reverse-ordered by concentration (**Fig. 3.2C**, and **fig. 3.S2B**). The response to 100 nM fMLP appeared intermediate—significantly separating from the 10 nM fMLP response by 10 minutes, and significantly separating from the 500 nM response by 7 minutes and continuing this trend at 10 minutes. This sustained phenotype is not shared by all signaling components downstream of FPR, as co-staining images for phospho-p38 showed that p38 activation similarly peaks at 2 minutes, but response curves for all (10, 100, and 500 nM) concentrations of fMLP fall sharply to or past baseline and do not significantly separate from one another (**fig. 3.S3**, A to D). Thus, at late (10 minutes) times, ERK1/2, but not p38, show concentration-dependent decay that transitions around 100 nM fMLP.

An attractive explanation for the sharp transition between directional and circuitous migration at approximately 100 nM fMLP (**Fig. 3.1E**) is that ERK is bimodal in certain biological systems. ERK has been characterized to exhibit an all-or-none, ultrasensitive response [124, 36] to external agonists. For example, in maturing *Xenopus laevis* oocytes [36], cells switch between no ERK activation or complete ERK activation, and no intermediate states are observed. In fact, ERK in chemotactic neutrophils was recently characterized as having a "plateaued" activation curve [85]. However, we plotted histograms from the individually analyzed cells, and found that the response distributions were gradated rather than bimodal (**fig. 3.S2C**). The response histograms, together with the noted lower stimulated peak activity and slower decay of ERK at 10 nM fMLP, lead us to conclude that the previous report of an apparently concentration-independent,

'plateaued' activation curve of ERK [85] was due to observing activity at a single timepoint of 2 minutes.

ERK, but not p38, is required for migration toward fMLP

ERK and p38 have been characterized as "stop" and "go" signals in neutrophil chemotaxis based on migration experiments with the inhibitors PD98059 and SB203580 [85]. Since PD98059 has been shown to deplete cellular calcium, we assessed the migration of HL-60s treated with the MEK inhibitor PD0325901 or the ERK inhibitor SCH772984. Both inhibitors completely block migration (**Fig. 3.3**, A to C and F). Consistent with previous work [85], we found that the p38-inhibitor SB203580 causes early cessation of directional migration (Fig. 3, D and F). However, the more specific [5] p38-inhibitor BIRB-796 does not replicate this phenotype (Fig. 3, E and F), which suggests that p38 may be dispensable for directional migration. The discrepancy between results from these two p38-inhibitors may be explained by several off-target effects of SB203580 [5], including its inhibition of Raf [47] and therefore of ERK1/2 (**fig. 3.S4**, A, D, and E). Together, our data demonstrate that ERK1/2, but not p38, are required for fMLP-directed migration (**Fig. 3.3G**).

p38 decreases ERK sensitivity to fMLP

p38 has recently been shown to phosphorylate FPR1 [85]. To ask whether p38 in turn alters signaling from FPR1 to ERK, we stimulated p38-inhibited cells with uniform concentrations of fMLP before fixation at various timepoints between 0 and 10 minutes

(**fig. 3.S2A**). Under these conditions, we found that ERK responses to 100 nM fMLP no longer fall cleanly below ERK responses to 10 nM fMLP. The ERK responses to 10 and 100 nM fMLP are indistinguishable in VX-702-treated cells (**Fig. 3.4A** and **fig. 3.S4C**). Meanwhile, the 100 nM fMLP response is in fact greater than the 10 nM fMLP response in BIRB-796-treated cells (**Fig. 3.4B** and **fig. 3.S4B**). This stronger phenotype in BIRB-796-treated cells may reflect the ability of BIRB-796 to inhibit p38δ, which is the most abundant p38 isoform in neutrophils [74] and inhibits ERK1/2 in other systems [33]. Comparison of response curves to 100 nM fMLP, normalized by fold change, reveals that both inhibitors of p38 cause a sustained ERK activation at 10 minutes (**Fig. 3.4C**) — suggesting that there may be time-varying network effects [76], and that p38 may inhibit fMLP-stimulated ERK activation specifically at late times (10 minutes).

To search for this trend within natural variations, we plotted co-stained control cells by their pERK and p-p38 intensities. We note that p38 and ERK display covariation at the peak time of 2 minutes, filling the upper right quadrant of the plots (**Fig. 3.4D**, left side). However, consistent with inhibitor data, we found that the cells with high pERK at late times (10 minutes) had low p-p38 (**Fig. 3.4D**, right side). Although p38 and ERK were previously reported not to alter one another's activation by fMLP [85], this conclusion was based on data from a single timepoint of 2 minutes. Our drug and natural variation data demonstrate that, across a broader time course, p38 appears to inhibit ERK—though it is unclear whether this inhibition occurs via protein phosphatase 2A [102] as in other systems, or at a different signaling level.

Discussion

Upon exposure to fMLP, a neutrophil will break its symmetry, establishing a polarized front and back, and begin migration. Although the molecular underpinnings of this initial cell polarization and directional sensing have been extensively characterized [167, 26, 143], it is less clear what signals are important for the behavior of neutrophils once they have migrated into high concentrations of fMLP. Recently, p38 and ERK1/2 have been implicated as "go" and "stop" signals [85], respectively, in this later phase of migration into saturating concentrations of fMLP. Here, we interrogated these molecular players with a wider array of specific inhibitors, and in the context of a characterized gradient.

Our results demonstrate that neutrophil migration saturates at approximately 100 nM fMLP (**Fig. 3.1E**), and that ERK1/2, but not p38, demonstrate concentration-dependence—transitioning around 100 nM fMLP—in the decay of cellular responses toward baseline after an initial peak (**Fig. 3.2D** and **fig. 3.S2**). ERK1/2 are activated in gradated responses (**fig. 3.S2B**), and appear to be absolutely required for migration in chemotactic neutrophils, as cells treated with the MEK inhibitor PD0325901 or the ERK inhibitor SCH772984 failed to migrate into an fMLP gradient (**Fig. 3.3**, B,C, and F).

These findings are consistent with other reports that ERK1/2 are necessary for adhesion and migration [16, 119], but contradict the model of p38 as a "go" signal and ERK1/2 as a "stop" signal for chemotactic neutrophils [85] moving within an fMLP gradient. Although we indeed replicated the early loss of directional migration [85] in cells treated with the p38 inhibitor SB203580 (**Fig. 3.3**, D and F), we note that

SB203580-treated cells showed inhibition [103] of ERK (fig. S4E) – perhaps due to the ability of SB203580 to inhibit Raf [47]. Further, we note that we found no such early loss of directional migration with BIRB-796 (**Fig. 3.3**, E and F) – which has higher specificity for p38, and blocks more isoforms of p38 [5]. Thus, our data suggest that, in chemotactic neutrophils, p38 plays the less direct role of modulating [103] ERK1/2, which in turn drive migration [103, 95] .

Materials and methods

Cell line and culture

HL-60 cells were cultured as previously described [87]. Briefly, cells were cultured in RPMI-1640 plus L-glutamine and 25 mM HEPES (Fisher Scientific) supplemented with antibiotic/antimycotic (Invitrogen) and 10% FBS (HyClone) in a 37°C / 5% CO_2 incubator. Cell differentiation was induced by adding 1.3% DMSO (endotoxin-free, hybridoma-tested; D2650, Sigma) to cell medium. Cells for all experiments were used at 5 days after initiation of differentiation.

Drug concentrations

Three p38 inhibitors (BIRB-796, VX-702, and SB203580) were used in our experiments. BIRB-796 and VX-702 were chosen for their selectivity [78, 5, 45]. Although BIRB-796 has few off-target effects even at a 1 μM dose [5], one of those few effects is its concerning inhibition of both the 46 kDa and 54 kDa isoforms of JNK (with IC_{50} values of 1 μM and 350 nM respectively, for a 2-hour incubation) [78]. A much lower BIRB-796 concentration of 10 nM was used for our experiments, as we

recapitulated the finding [78] that 10 nM BIRB-796 partially inhibits p38 within 90 minutes (**Figure 3.S5**). Meanwhile, VX-702 has been reported to inhibit p38 with an IC_{50} of 4-20 nM in gel-filtered platelets [78], and spares the JNK pathway more readily (with insignificant effects on JNK1 and a K_D of 2.6 μM for JNK2 [45]). In light of this increased selectivity, we chose and validated the on-target efficacy (**Figure 3.S5**) of a 100 nM concentration of VX-702. Finally, the SB203580 concentration of 10 μM was the same used within a recent study on the same cell line [85], for easy comparison.

Two inhibitors, PD0325901 and SCH772984, were used to decrease ERK activation in our experiments. PD0325901 inhibits MEK1, thereby inhibiting ERK, but has not been found to have significant off-target effects across a panel of 68 kinases, even at a dose of 10 μM [5]. Additionally, a dose of 500 nM PD0325901 has been shown not to alter cell calcium signaling [155]. A recent study of neutrophil migration in mice [103] administered 5 mg/kg doses of PD0325901 intravenously, during the course of *in vivo* imaging. Considering that a mouse weighs about 25 g and has a blood volume of about 2 ml [96], and that the molar mass of PD0325901 is 482.19 g, it is possible that this 5 mg/kg PD0325901 dose caused a circulating concentration of 130 μM PD0325901 upon injection. To fall within the safe bounds of the aforementioned off-target effect studies [155, 5], we instead chose a concentration of 100 nM PD0325901.

Finally, in choosing the concentration of the ERK inhibitor SCH772984, we considered that the IC_{50} value of SCH772984 has been found to be 1-4 nM in cell-free systems [106] and 60 nM *in vivo* [128], and that treatment with 100 nM SCH772984 has been shown to inhibit phosphorylation of ERK in cell studies [106]. However, the K_D

value of SCH772984 has been found to be ~200 nM, due to allosteric binding in which a glutamine gatekeeper within ERK accommodates the piperazine-phenyl-pyrimidine end of the SCH772984 molecule in a configuration that allows for key aromatic stacking interactions [19]. This binding promotes slower on-target off-rates and faster off-target off-rates [19]. For instance, the structurally similar JNK1, for which SCH772984 has an off-target IC_{50} of 1 μM, can only bind SCH772984 such that the piperazine-phenyl-pyrimidine end of SCH772984 is forced to point into the solvent, leading to few direct interactions between the drug and JNK1 [19]. In light of the reported IC50 and K_D values, we chose and validated the on-target efficacy of a 100 nM concentration of SCH772984 (**Figure 3.S5**).

Gradient migration assays

Live cells were imaged within an fMLP gradient generated by a sterile μ-Slide Chemotaxis^{3D} microfluidic device (ibidi, 80326) coated with fibronectin (50 μg/ml). Differentiated HL-60 cells were washed and resuspended in serum-free RPMI-1640 plus L-glutamine and 25 mM HEPES, in which either drug (10 μM SB203580, 10 nM BIRB-796, 100 nM VX-702, 100 nM PD0325901, or 100 nM SCH772984) or vehicle (DMSO) was dissolved. Each suspension was then seeded into the observation area and right reservoir of a chamber within the ibidi μ-Slide Chemotaxis^{3D} microfluidic device. After two hours of incubation in a 37°C / 5% CO_2 incubator, the chambers were carefully flushed with serum-free RPMI-1640 plus L-glutamine and 25 mM HEPES, with their respective drug dilutions. A gradient with a maximum value of 500 nM fMLP was created across the observation area of each chamber by gently pipetting chemoattractant

into the left reservoirs, in accordance with manufacturer instructions. Cells were immediately imaged in a heated chamber for 3 hours. Montage images of the entire observation area were recorded with a BD Pathway 855 Bioimager (BD Biosciences) equipped with a laser autofocus system, an Olympus 10× objective lens, and a high-resolution Hamamatsu ORCA ER CCD camera. Image acquisition was controlled by AttoVision v.1.5 (BD Biosciences). Cell tracks were then identified on ImageJ software [134] with the Manual Tracking plugin. Endpoints of cell tracks were overlaid on an image of a 500 nM gradient of fluorescein-conjugated formyl-Nle-Leu-Phe-Nle-Tyr-Lys (Invitrogen), using the distinctive ends of the observation chambers as fiducials.

Uniform field stimulation assays

As in the gradient migration assays, differentiated HL-60 cells were washed and resuspended in serum-free RPMI-1640 plus L-glutamine and 25 mM HEPES, in which either drug (10 μM SB203580, 10 nM BIRB-796, 100 nM VX-702, 100 nM PD0325901, or 100 nM SCH772984) or vehicle (DMSO) was dissolved. Cells were plated onto 96-well Nunc glass plates (Thermo Scientific, 164588) coated with fibronectin (100 μg/ml). After two hours of incubation in a 37°C / 5% CO_2 incubator, the wells were uniformly stimulated with fMLP (dissolved in their respective drug solutions) before formaldehyde fixation at the specified timepoints (Fig 3A). Immunofluorescent staining was then performed as previously described [76, 152], with phospho-Erk1/2 (Thr202/Tyr204) (Cell Signaling Technology, 9101) and phospho-p38 (Thr180 + Tyr182) (Abcam, ab45381) antibodies. Fluorescence images were acquired on the BD Pathway 855 Bioimager (BD Biosciences) with an Olympus 20× objective lens. Cellular features,

including cell-averaged signal intensity and eccentricity, were extracted using CellProfiler [18], and then plotted as response curves, histograms, 3-D surface plots, and scatterplots with custom-written MATLAB code. (See also **Appendix B** for sample scripts.)

Statistics

Statistical significance was assessed using the two-sample Kolmogorov-Smirnov test for generating P values. $P < 0.05$ was considered statistically significant.

Figures

Figure 3.1. Overview of gradient characterization. (**A**) The ibidi Chemotaxis[3D]

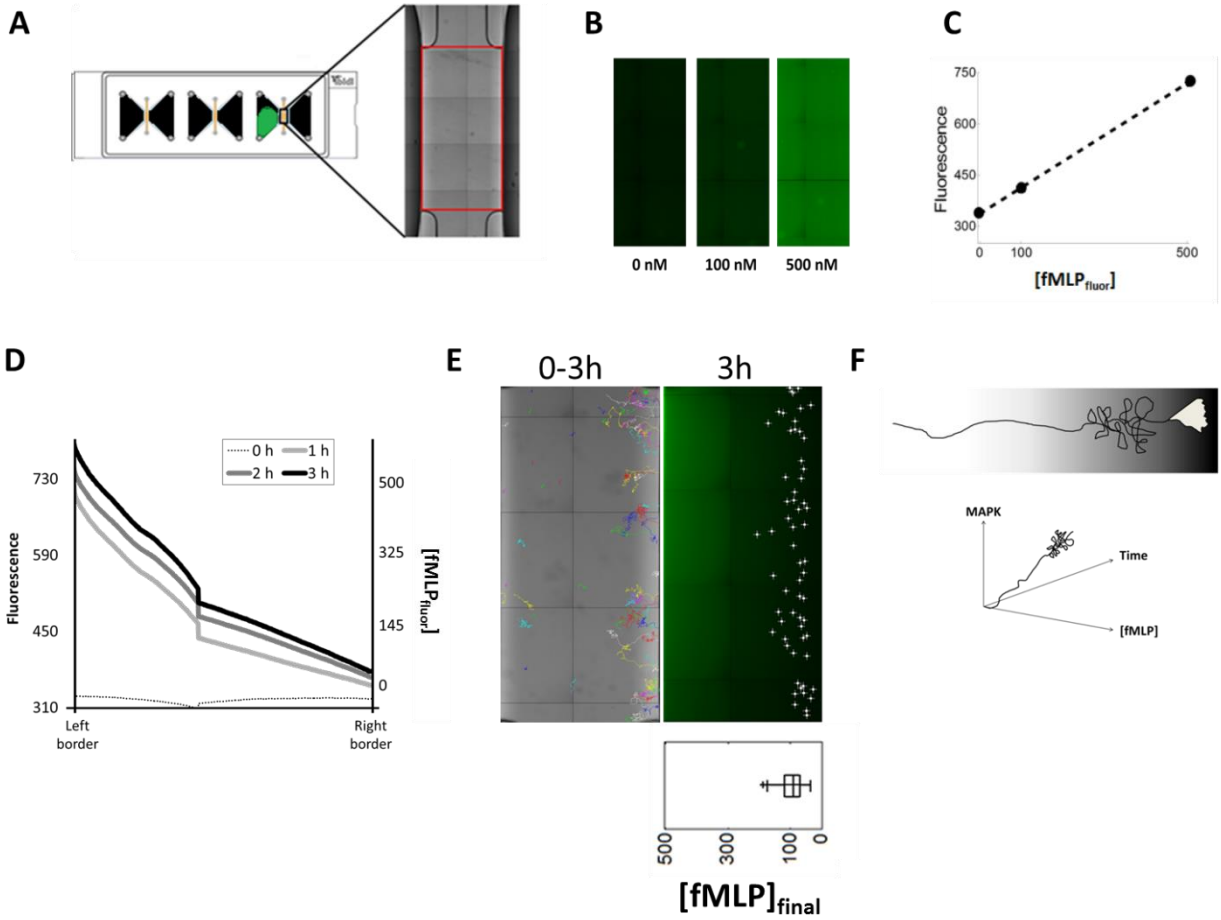

microfluidic device was used for visualization of the chemoattractant gradient. (**B**) Known concentrations of a labeled fMLP derivative, fluorescein-formyl-Nle-Leu-Phe-Nle-Tyr-Lys, were imaged. (**C**) The fluorescence of these images allowed us to relate fluorescence to concentration. (**D**) A gradient of 500 nM fluorescein-formyl-Nle-Leu-Phe-Nle-Tyr-Lys could then be characterized by both its fluorescence and concentration across the device's observation area. (**E**) Tracks (multicolored, left) were created from 3-hour microscopy videos of cells migrating in gradients of fMLP. The endpoint of each

track at 3 hours (white dots, right) were overlaid on the visualized gradient of fluorescein-formyl-Nle-Leu-Phe-Nle-Tyr-Lys, using the distinctive ends of the observation area as fiducials. Images are representative of three experiments. Boxplot contains data combined from three experiments. (**F**) Studies of chemotaxis within a gradient are confounded by the fact that both the parameters of concentration and time vary as a cell migrates.

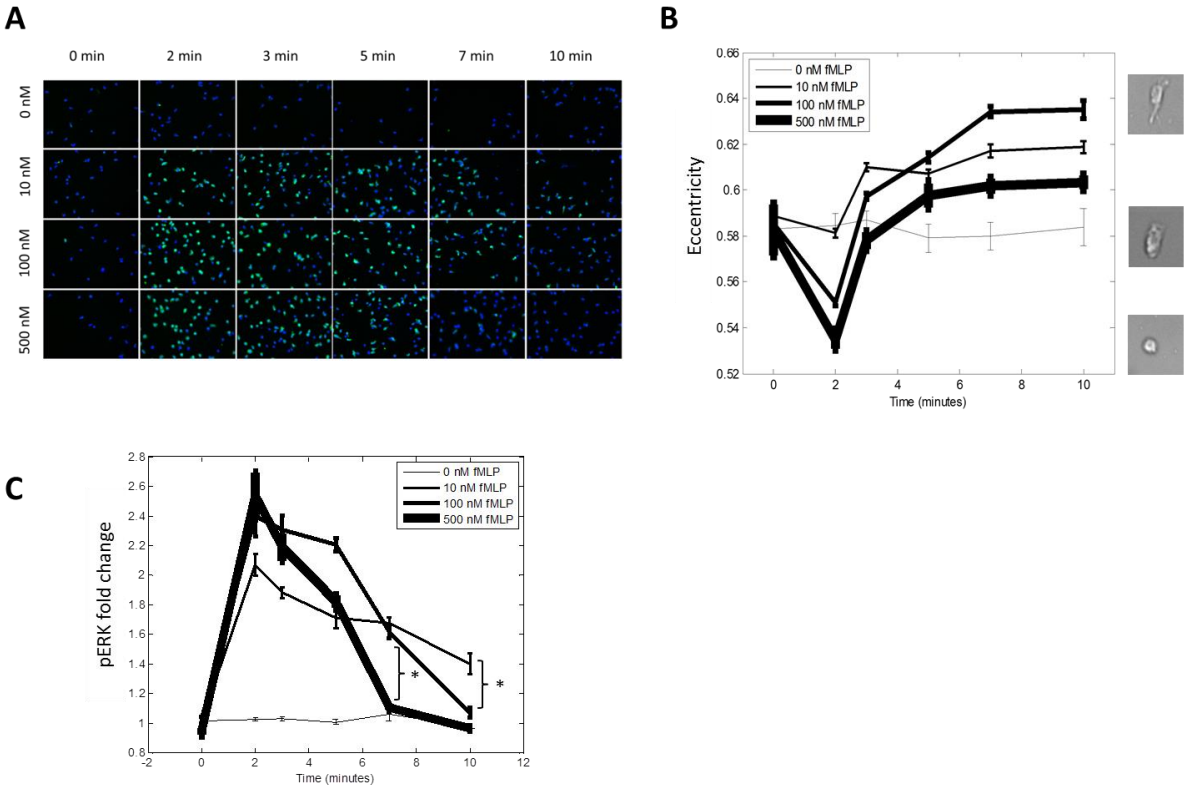

Figure 3.2. Morphology changes, but not ERK1/2 activation, terminate within 10 minutes. (**A**) Cell pERK intensities and eccentricities were extracted from fixed cell images (one frame representative of 36 frames per well, 4 replicate wells per condition). (**B**) The 10-minute timeframe was adequate for termination of morphology changes. (**C**) Within the 10-minute timeframe, however, pERK remained activated in cells stimulated with 10 nM fMLP, and response curves for the three concentrations of fMLP separated from one another. Data are means ± s.e.m. from four replicate experiments. *P < 0.05 compared to controls by two-sample Kolmogorov-Smirnov test.

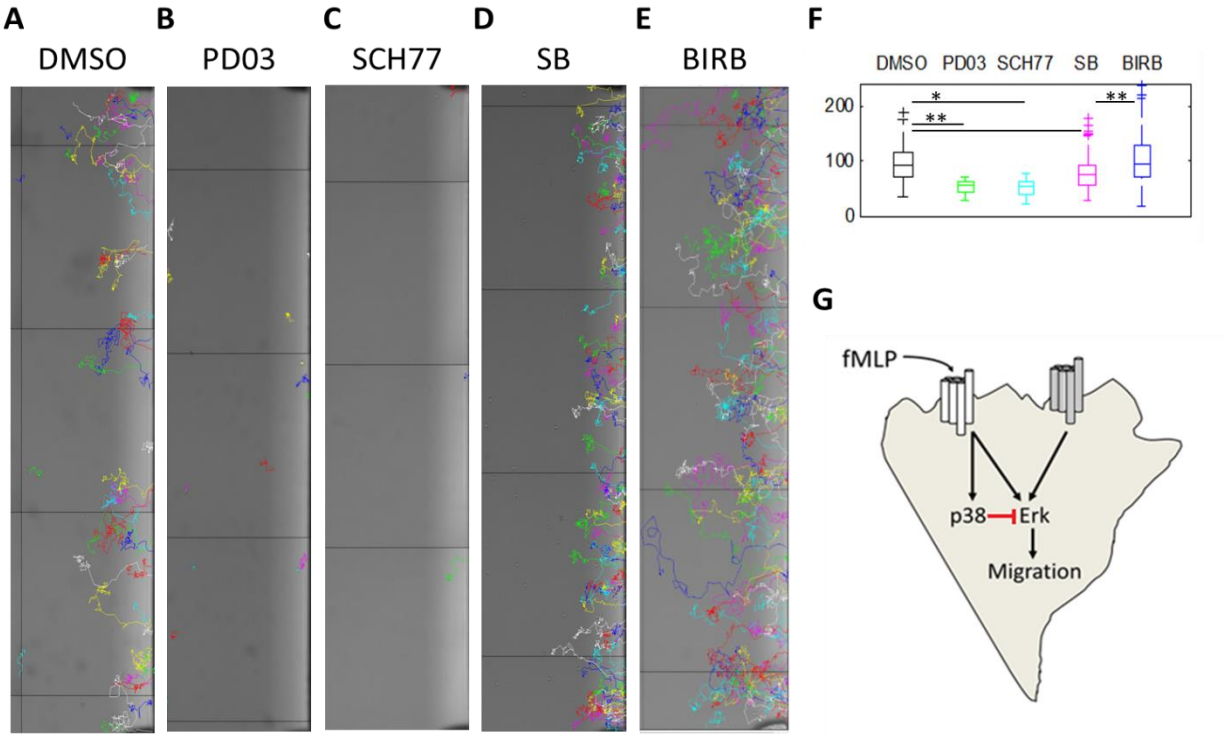

Figure 3.3. ERK, but not p38, is required for migration toward fMLP. (**A** to **E**) Representative migration tracks from cells treated with (A) DMSO, (B) 100 nM PD0325901, (C) 100 nM SCH772984, (D) 10 μM SB203580, and (E) 10 nM BIRB-796. (**F**) Quantification of migration tracks, with three replicate experiments combined within each boxplot. *P < 0.05 and **P < 0.01 compared to controls by two-sample Kolmogorov-Smirnov test. (**G**) Working model in which p38 inhibits ERK, which in turn drives migration. Red: interaction appearing at late times.

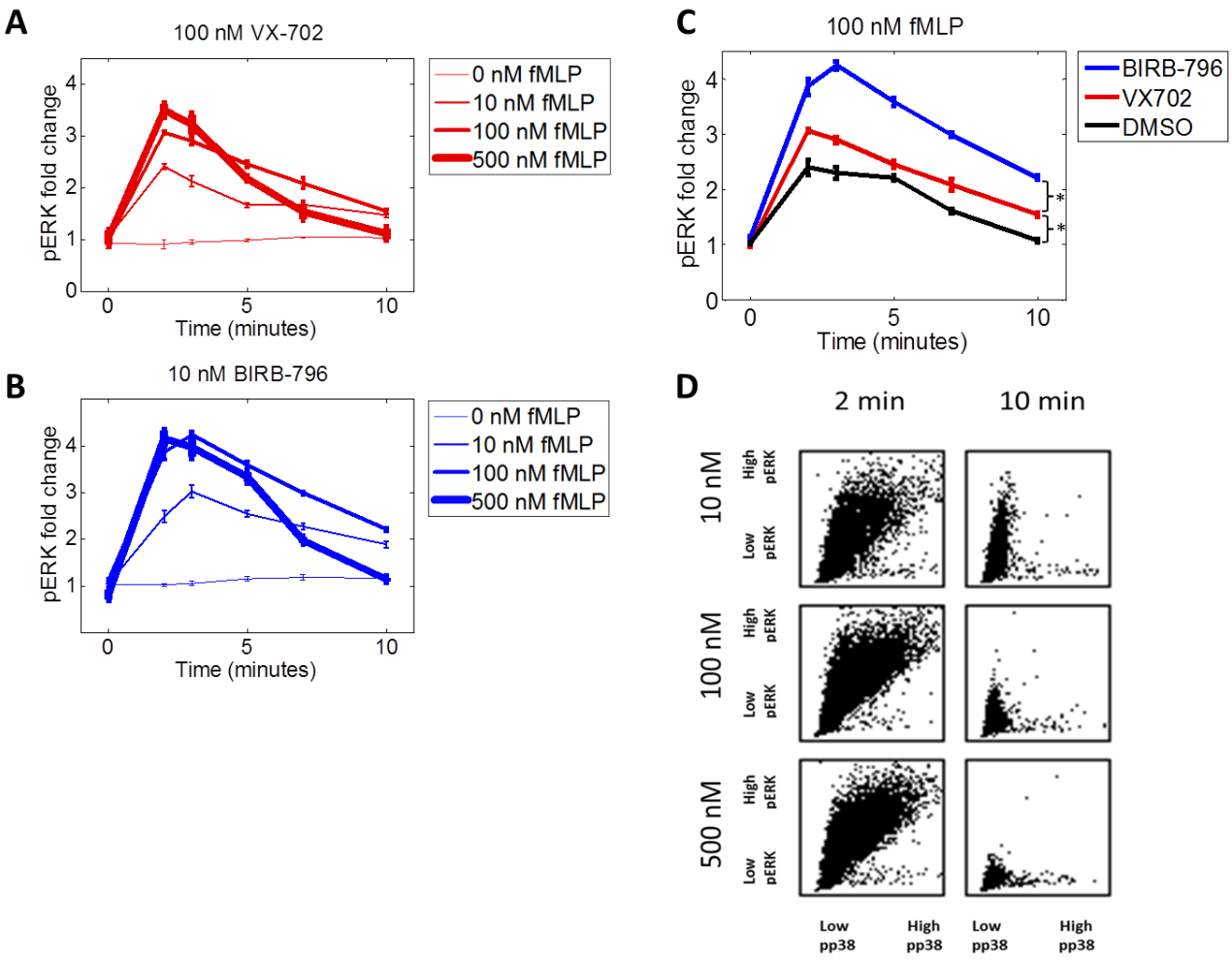

Figure 3.4. p38 inhibits ERK at late timepoints. (**A** and **B**) p38 inhibition by (A) VX-702 or (B) BIRB-796 results in the response curve for 100 nM fMLP rising up to meet or exceed the response curve for 10 nM fMLP at late (10 minutes) times. (**C**) Comparison of response curves to 100 nM fMLP reveals that both inhibitors of p38 cause a sustained ERK activation at 10 minutes, as compared to the 100 nM response curve of DMSO control. (**D**) Natural variations within DMSO control cells show that covariation of p-p38 and pERK at the peak time of 2 minutes, but that cells with high pERK at 10 minutes

have low p-p38. Data are means ± s.e.m. from four replicate experiments. *$P < 0.05$ compared to controls by two-sample Kolmogorov-Smirnov test.

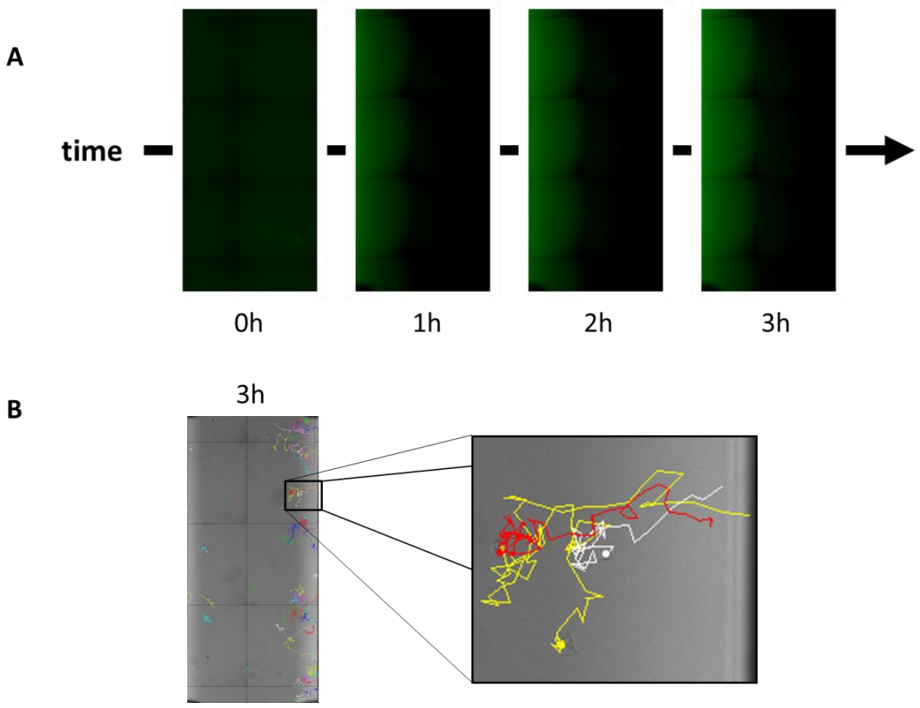

Figure 3.S1. Migration of cells across a linear fMLP gradient. (**A**) Chemoattractant gradients were found to be stable and linear throughout three hours of live-cell microscopy, as read out by of fluorescein-formyl-Nle-Leu-Phe-Nle-Tyr-Lys. (**B**) At approximately 100 nM fMLP within an fMLP gradient, cell migration remains in action but ceases to be productive.

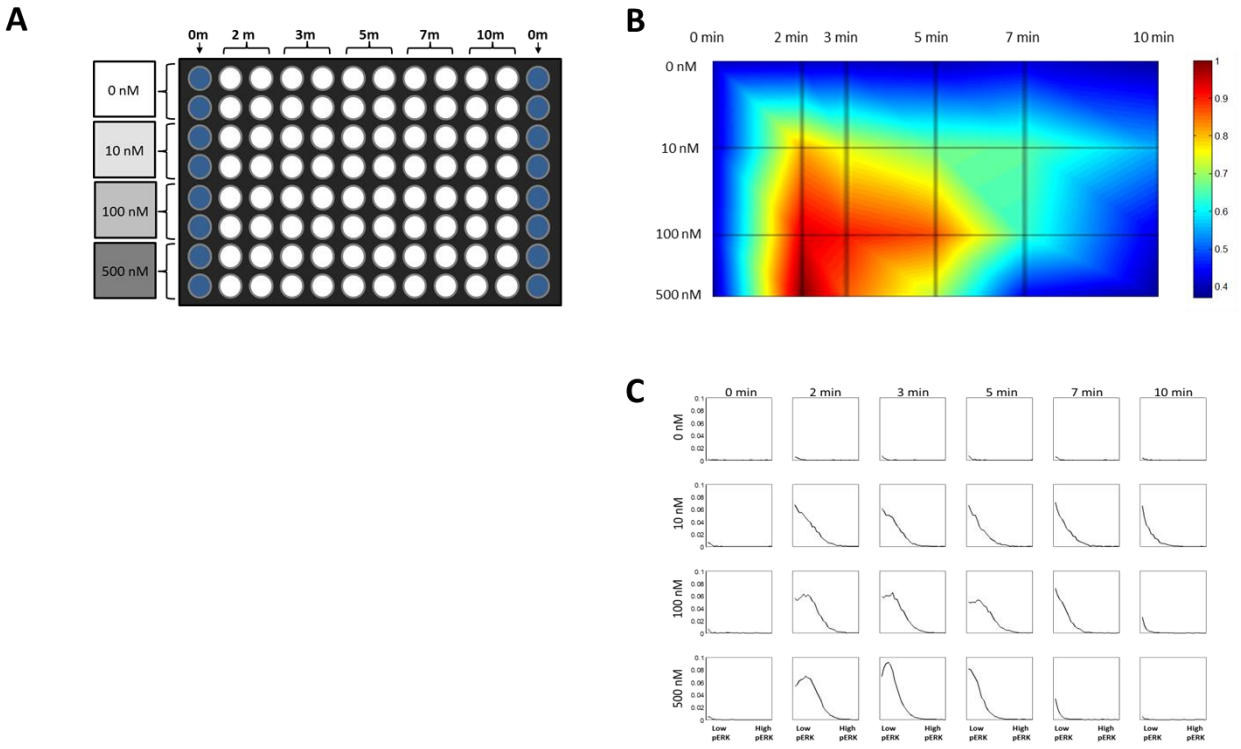

Figure 3.S2. ERK activation remains elevated in cells responding to 10 nM fMLP. (**A**) Cells were stimulated with concentrations of 0, 10, 100, or 500 nM for various times between 0 and 10 minutes. (**B**) Surface plot of cell-averaged pERK activity of cells (n=168,837) across fMLP concentrations and times. (**C**) pERK response histograms of cells across fMLP concentrations and times.

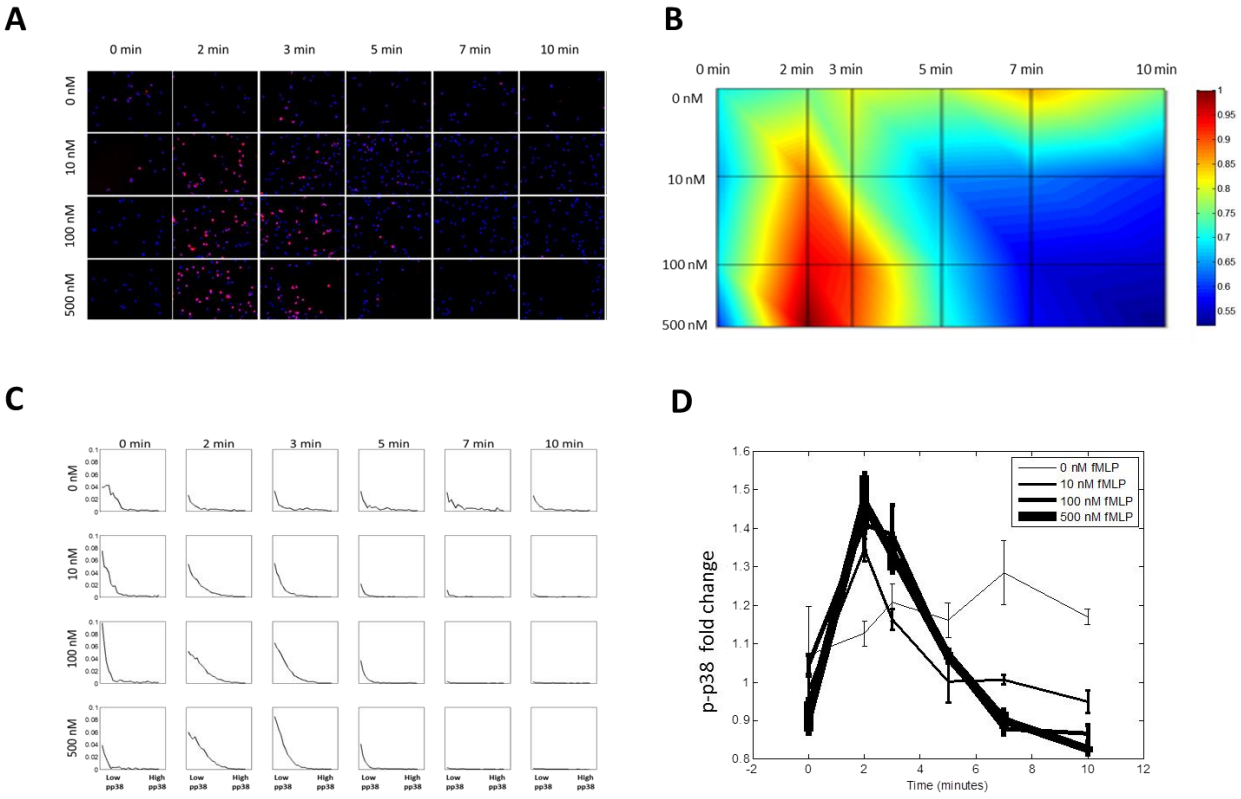

Figure 3.S3. p-p38 falls to or past baseline within 10 minutes of fMLP stimulation. (**A**) Cell p-p38 intensities were extracted from fixed cell images (one frame representative of 36 frames per well, 4 replicate wells per condition). (**B**) Surface plot of cell-averaged p-p38 activity of cells (n=168,837) across fMLP concentrations and times. (**C**) p-p38 response histograms of cells across fMLP concentrations and times. (**D**) p38 peaks at 2 minutes, but falls sharply to or past baseline for all concentrations of fMLP.

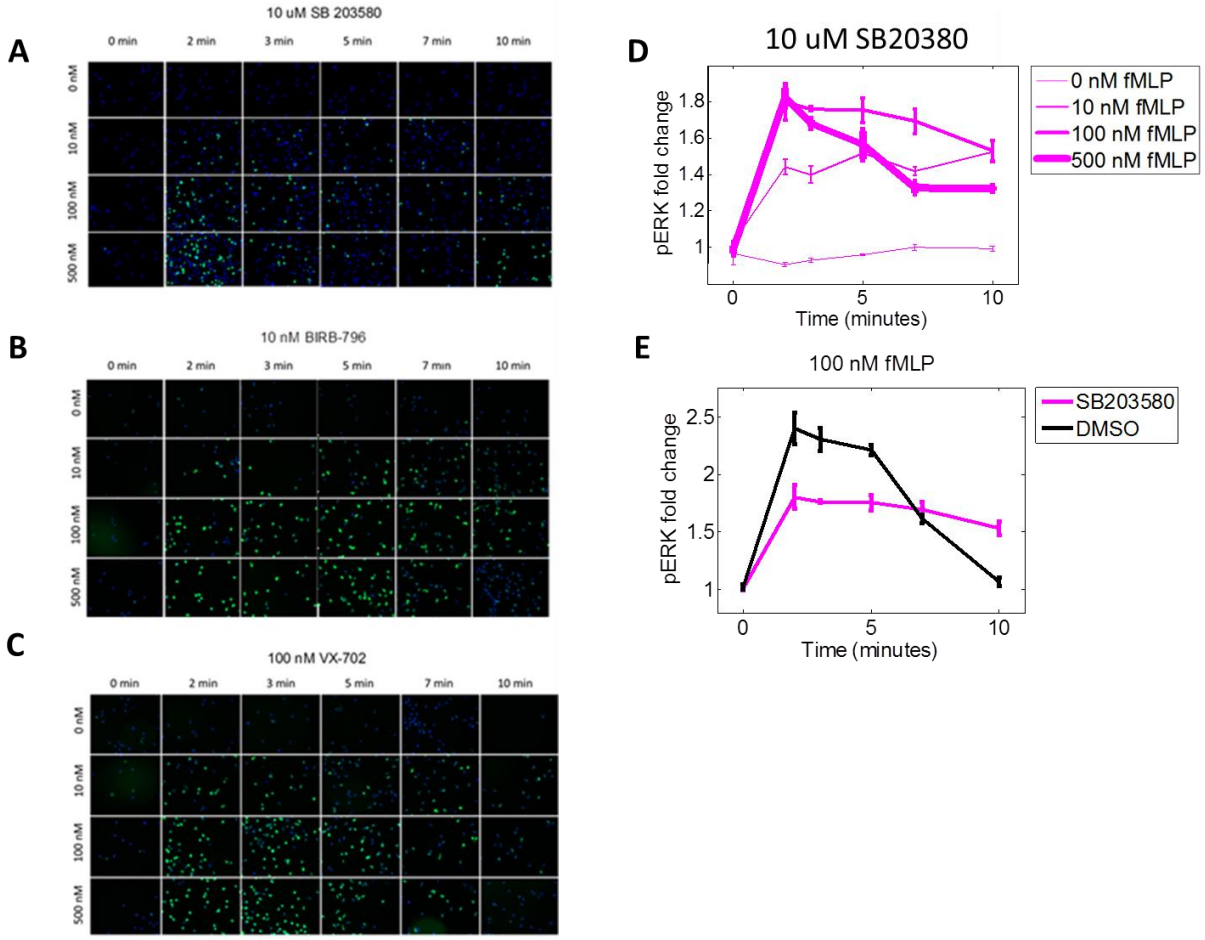

Figure. 3.S4. p38 inhibition results in elevated pERK at late timepoints after 10 or 100 nM fMLP exposure. (**A** to **C**) Within the 10-minute time-course, pERK intensity remained elevated in response to 10 or 100 nM fMLP when cells were p38-inhibited with (A) 10 μM SB203580, (B) 10 nM BIRB-796, or (C) 100 nM VX-702. One frame representative of 36 frames per well, 4 replicate wells per condition. (**D**) Quantification of ERK response curves of SB203580-treated cells. (**E**) Comparison of 100 nM fMLP response curves of SB203580-treated and DMSO control cells reveals that SB203580 causes a sustained ERK activation at 10 minutes—consistent with the phenotypes from

the other p38 inhibitors—but that SB203580 also produces an early inhibition of ERK as compared to DMSO control.

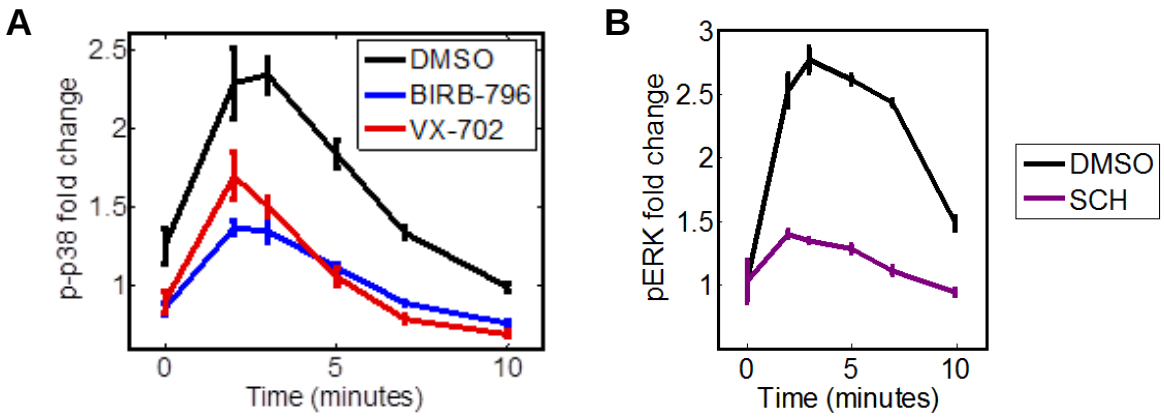

Figure 3.S5 On-target effects of MAPK inhibitors. (**A**) Test of p38 inhibition by 10 nM BIRB-796 and 100 nM VX-702. (**B**) Test of ERK inhibition by 100 nM SCH772984.

CHAPTER FOUR

Conclusions and Future Directions

Microtubule-mediated regulation of the $G_{12/13}$-initiated back module

The laboratory of Henry Bourne formalized the idea of front and back signaling modules in neutrophil polarization, and demonstrated that these modules are mutually opposing [167], which drives the initial symmetry-breaking and polarization of the cell. However, this mutual implication would imply negative dependence of the modules on one another, and thus the question arose of how stable polarity is maintained:

> In the form presented here, the simple competition hypothesis may not fully account for the stable asymmetry of neutrophils and dHL-60 cells, which remain completely polarized, with a single pseudopod as long as fMLP is present. The competition might result in triumph of one response over the other unless the cell can preserve a precise, potentially delicate balance between frontness and backness signals.
>
> —Wong et al., 2006 [160]

A candidate emerged when the Bourne lab discovered a role for microtubules in front/back regulation [168]. However, the regulatory nature of this link was left unclear. This work left two key questions open. First, does the microtubule-mediated link affect the back negatively or positively? Second, does this link affect the total activity or spatial distribution of the back? The assays in which signaling component activities were measured were performed on cell lysates and could not tease out spatial effects. We show experimentally that this microtubule-mediated regulation affects the spatial localization, but not the intensity of back signaling (pMLC2), and that this signaling link is a net positive regulator of the back polarity.

Later work reported the presence of a long-range positive link from front (Cdc42 and PIP3) to back (RhoA) [148], which was later shown to be mediated by microtubules [79]. However, the ramifications of such a microtubule-mediated link on signaling behaviors between the front and back signaling modules were unknown. The authors suggested that quantitative modeling would help elucidate the role of a long-range link in creating robust polarity:

> Finally, intuition must be converted into a model that quantitatively predicts the effects of perturbing specific signals on the initiation and stability of polarity.
>
> —Van Keymeulen et al., 2006 [148]

We address these questions with both quantitative analysis of imaging experiments, and with mathematical modeling. Experimentally, we find that back (pMLC2) activity and localization are surprisingly invariable—i.e., insulated—across the natural range of F-actin signaling. Pharmacological disruption of microtubules unveils the anticorrelation suggested by the competition model [160], demonstrating that microtubules insulate the front and back modules from their negative co-dependence. Covariation analysis of F-actin and pMLC2 in control cells confirm this role of microtubules, and implicates their localized transport, rather than global sequestration, of back activators. (**Fig. 4.1**) Our mathematical model, which simulates microtubule transport but excludes microtubule-based sequestration, is able to recapitulate the experimentally observed insulation of back signaling from front variations, and thus demonstrates the sufficiency of microtubule transport of back activators for achieving insulation. Meanwhile, our topological search of polarizing network topologies shows,

more generally, that a long-range positive link is necessary for insulation of back signaling localization from front intensity variations in chemotactic cells.

Future studies should be done to identify the microtubule-transported signal that mediates the insulation of back pMLC2 signaling. Additionally, since disruption of neutrophil microtubules can cause decreased directional persistence [168] as well as the phenotype in pMLC2 localization that we observed, it will be intriguing to connect pMLC2 insulation to migrational phenotypes. A potential next step may be knocking down back-activating GEFs to see if a phenotype emerges in either pMLC2 localization or directional persistence.

MAPK regulation of neutrophil chemotaxis

ERK and p38 have been implicated in determining the concentration of fMLP at which directional neutrophil chemotaxis saturates [85]. Through natural variation analysis, experimental perturbations with a wider array of specific inhibitors, and visualized gradients, we show that (i) neutrophils switch from directional to circuitous migration at approximately 100 nM fMLP, that (ii) ERK1/2 display fMLP-concentration-dependent dynamics that transition at 100 nM fMLP, and that (iii) ERK1/2, but not p38, are required for directional migration through an fMLP gradient.

An interesting finding that our submitted manuscript (Chapter 3) did not pursue was the increased final concentration of fMLP at which BIRB-796-treated HL-60 cells lost directionality (**Fig. 3.3**, A and E). With the rudimentary metric of final position, we did not observe a statistically significant difference between the BIRB-796 and control

conditions. However, I am now writing MATLAB code to further analyze the migrational tracks. If a statistically significant difference arises in other migrational parameters, the question then will be how p38 causes this phenotype.

p38 phosphorylates formyl peptide receptor [85], as mentioned in Chapter 3, and previous reports that receptor phosphorylation might not attenuate GPCR signaling in chemotaxis [50, 69, 12] have recently been refuted [14]. Therefore, it will be worthwhile to see if a migrational difference BIRB-796-treated cells is due to a role of p38 in formyl peptide receptor desensitization. Sensitivity can be tested by using the cell-permeable calcium indicator dye, Fluo-4-AM, to measure calcium responses to fMLP in p38-inhibited and DMSO control HL-60 cells [23]; intracellular calcium release is initiated downstream of formyl peptide receptor, separately from the pathway that triggers the polarization machinery [23, 162]. Alternatively, the salient effect of p38 may be further downstream, within the polarization pathway. For instance, the major substrate of p38-activated MAPKAPK2 in neutrophils is LSP1 [66], the actin-binding protein that is overexpressed in neutrophil actin dysfunction [10, 141, 21, 54, 83]. LSP1 is a negative regulator of neutrophil chemotaxis [65], which colocalizes with F-actin only when phosphorylated [164]. Quantitative image analysis of phospho-LSP1 staining can test this hypothesis.

C5a-mediated neutrophil dysfunction

Neutrophils navigate through multiple chemoattractants before reaching a final site of inflammation. How does historical exposure affect neutrophil polarization and

chemotactic behavior? Before prioritizing the research described in Chapter 3, I developed preliminary data on how Complement component 5a (C5a) changes fMLP-induced polarization.

Both fMLP and C5a are "end-target" chemoattractants, i.e. they lead neutrophils to the final site of infection [49]. Additionally, both fMLP and C5a are created by the presence of bacteria; fMLP is directly shed as a by-product bacterial protein synthesis [41], while C5a is produced when the host's complement cascade is triggered by bacterial surfaces [131]. Paradoxically, despite C5a's origin from a bactericidal cascade initiated by the host's own proteins, C5a-pretreated neutrophils are less able to kill bacteria and migrate less effectively toward fMLP [105, 22]. This loss of chemotaxis toward fMLP is not simply due to diminished fMLP-binding by the neutrophil's receptors [139, 138]. C5a-treated neutrophils also show defective activation of RhoA [105] and ERK1/2 [55].

Where in the chemotactic network is this dysfunction occurring? These questions may reveal not only fundamental principles of the core neutrophil polarity network, but also relevant insights into systemic inflammatory response syndrome (SIRS) and sepsis [55, 131, 22, 105, 46, 122, 123, 153]. For severely infected patients, C5a concentrations and bacterial load are both high; in fact, C5a levels in septic patients correlate with the degree of clinical severity[122, 108]. Thus, an understanding of the overlaps and conflicts in C5a- and fMLP-induced chemotaxis could elucidate how neutrophils make decisions in a critical, life-threatening setting for patients.

In our preliminary studies (**Fig. 4.2**), HL-60 cells had a dramatically different polarization response to fMLP when they were first pretreated with 10 nM C5a for 30 minutes (in patients with sepsis, chronic circulating C5a concentration may be 10-100 nM [139, 154]). Our observation of differences at 60 seconds of fMLP exposure also raises the question of whether C5a-pretreated neutrophils exhibit divergence not only in final outcomes, but also in early processing. Future analysis of this polarization defect would be of great clinical interest.

Conclusion

Chemotaxis is a multifaceted process, many pieces of which remain poorly elucidated. While the utility of mathematics in biology is often thought to be the creation of detailed models, mathematics may be incorporated throughout the iterative cycle of experiment and theory: to increase the resolution with which behaviors are observed and to predictively associate behaviors and networks. Importantly, these applications of mathematics may not only push the field closer to a whole-cell understanding of migration, but also reveal general principles utilized in chemotaxis, and perhaps across many other cell signaling processes. With the current availability of CellProfiler, a highly efficient, open-source, image analysis program [18] (see also **Appendix C** for single-cell analysis protocol), laboratories with and without quantitative image analysis experts can study this essential biological process with enhanced experimental resolution.

Figures.

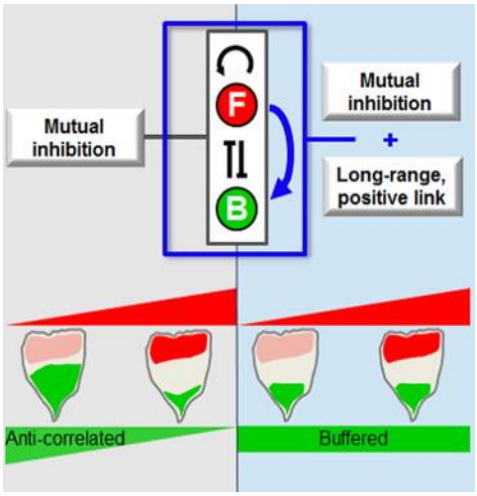

Figure 4.1. Graphical abstract of microtubule-mediated regulation of the $G_{12/13}$-initiated back module.

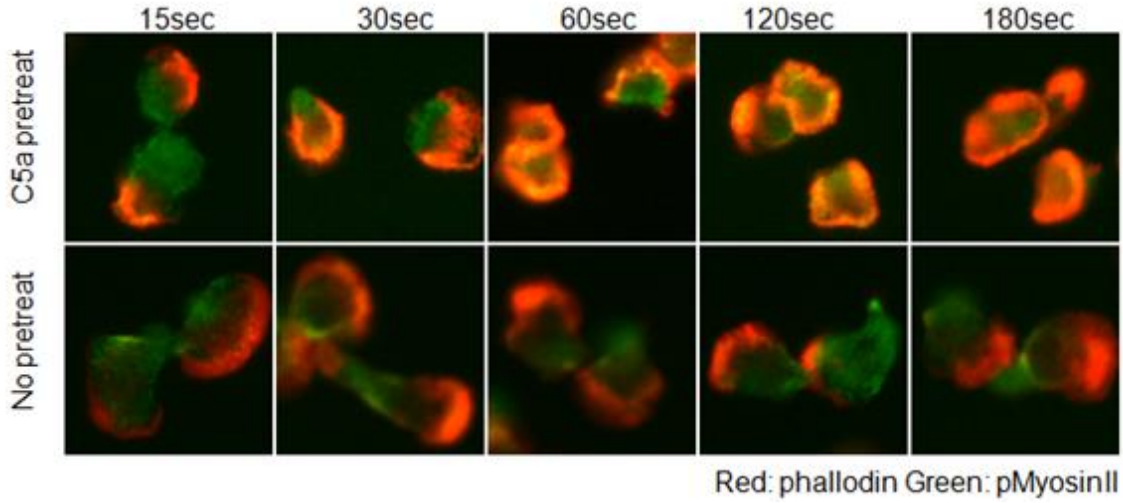

Figure 4.2. Neutrophil polarization response to 10 nM fMLP, with and without 30 minutes of 10 nM C5a pretreatment.

APPENDIX A

Extended discussion on conceptual versus data-driven modeling

Ab initio ad finem*: the spectrum of uses for math modeling*

Mathematical models vary widely in their levels of abstraction and biological detail [104]. At the one extreme are conceptual models, which may seek to identify minimal circuits and *ab initio* mechanisms underlying observed phenomena. At the other extreme are data-driven models, which incorporate experimental data in order to ask whether the resultant equations recapitulate, *ad finem*, experimentally observed behavior. What kind of models do we need to build to learn more about a behavior as complex as cell migration? Here, we argue that the path toward greater understanding of cell migration is not a straight shot through increasingly mechanistic territory.

Bird's eye view: conceptual modeling

Conceptual models can be used to capture the essence of what is currently known about a biological system. For instance, Ofer et al. [113] studied the simple migration system of keratocyte fragments, which lack cell bodies. The authors created force-balance equations to demonstrate the emergence of global shape and speed from underlying actin dynamics and membrane tension. This study elegantly highlighted the minimum requirements for coordinating retraction of the rear with protrusion at the front. Similarly, Neilson et al. [110] studied pseudopod formation in *Dictyostelium discoideum*.

The authors modified Meinhardt's discrete model of chemotactic orientation [94] to demonstrate that a cyclical internal process can be used to recapitulate both pseudopod formation and orientation bias. This simple conceptual model suggested a pseudopod-centered mechanism of chemotaxis. Conceptual models can identify minimal circuits, and thus reveal general principles at the heart of more complex circuits.

Conceptual models for zooming out and narrowing in

Conceptual modeling can also be used to survey minimal circuits capable of creating observed phenomena, which in turn can guide future studies—that is, zooming out can allow the field to narrow in. For example, perfect or near-perfect adaptation enables cells to respond to the gradient, rather than the average value, of a signal [82]. Ma et al. explored this property not by modeling the known signaling components of these networks, but by generalizing chemotactic and other biological networks into abstract three-node networks, and performing a topology search over all of the possible relations of the three nodes [89]. This search revealed that only two network designs, the negative feedback loop and the incoherent feed forward loop, are capable of achieving perfect adaptation.

This general finding may then guide future mechanistic studies of cell migration. A recent cross-correlative study of GTPases, actin, phosphoinositides, and edge velocity by Kunida et al. indicated adaptation of Rac1 activity in response to PI3K inhibition [80]. To search for a source of this behavior, Kunida et al. looked to the abstract, conceptual

search performed by Ma et al. for networks capable of adaptation. Of the two candidate topologies that Ma et al. identified, the negative feedback topology recapitulated Kunida et al.'s experimental findings. Kunida et al. thus searched for a negative regulator of actin and Rac1, and found that myosin light chain kinase acts as a node in the causative negative feedback loop for the observed adaptation. Although negative feedback between frontness signals such as Rac1 and backness signals such as myosin light chain kinase has long been established in migrating cells [167], the relevance of such feedback to adaptation is an unexplored area. Thus, mathematical modeling and constraints from an abstract topology search were used in this mechanistic study to find a new behavioral implication of a known biochemical link. More recent topology searches for networks capable of polarization [20] may provide similar guidance for future mechanistic efforts.

Data-driven models as predictors

Data-driven models may be used not only as final tests of understanding, but also as ways of picking up *in silico* where observation is limited *in vitro.* For instance, Shibata et al. [137] created kinetic equations to describe the reactions of phosphatidylinositol lipids in chemotactic cells. Their simulations and experiments both showed two types of behaviors for the localization of PIP3: traveling waves and the formation of transient domains. The authors explored ranges of variables in their simulations in a systematic manner that is not possible *in vitro*, and found that the traveling waves are induced by an instability of the stationary uniform state, while stochastic noise was important for transient domain-formation.

Similarly, Marée et al. [93] created a data-driven model to explore the effects of both biophysical and chemical feedback on cell polarization and motility. Their model suggested that cell shape is not just a downstream readout, but also feeds back by directly affecting the internal distribution of GTPases. Meanwhile, their model allowed them to test the effect of different values of phosphoinositide feedback; this allowed the authors to note that an intermediate level of phosphoinositide feedback creates normal migration. Lin et al. [84] expanded this model and predicted that a gradient of Rac activation can create a strong cell polarization response, that the timing of this polarization depended strongly on the gradient of Rac, and that antagonism between Rac and Rho could amplify polarization; *in vitro* creation of such a gradient with a rapamycin stimulation system confirmed their *in silico* prediction.

Finally, data-driven models have been used to predict not only outcomes, but also new hypotheses altogether. Wu et al. [163] created data-driven decision-tree models to analyze a 'cue-signal-response' data set from multipotent stromal cells. Similar to their work in fibroblasts [48, 68], the modeling classified responses to combinations of signals and conditions. Their decision trees revealed a non-intuitive prediction that decreasing ERK would promote cell migration, at least in multipotent stromal cells, which they then confirmed *in vitro*.

Conclusion

Conceptual modeling is commonly used when a circuit is poorly characterized. However, conceptual models can also be applied to well characterized systems to replace

the biological circuit's details with simpler functional units–much like the creation of Thévenin equivalent circuits [13] for electronic circuits. Meanwhile, data-driven models are often applied to well-known systems to identify missing pieces. For example, in the case of bacterial chemotaxis, ultrasensitivity of the system could not be explained by known components, and data-driven modeling was used to demonstrate that the motor itself adapts at the level of switch component subunit clusters [170]. However, a data-driven approach may also be used to guide our knowledge of which pieces of a poorly-characterized system are most important to its operation. Iteration between conceptual and data-driven models can identify design principles and constraints which may guide future experimental and modeling endeavors in cell migration.

APPENDIX B

Sample MATLAB code written for processing CellProfiler data in Chapter 3

Timecourses

```
figure
thicknesses=[0.5,2,4,8];
load('C:\Users\Ezhang\RPMI_2.mat')
feature=handles.Measurements.Cell_by_pERK.Intensity_MeanIntensity_pERK;
wells=handles.Measurements.Image.Metadata_Well;
feature=transpose(reshape(feature,12,8));
wells=transpose(reshape(wells,12,8));
sequential=horzcat(feature(:,12),feature(:,1:11));
sequential_wells=horzcat(wells(:,12),wells(:,1:11));
conc_timepoint_means=zeros(4,6);
conc_timepoint_stds=zeros(4,6);
times=[0,2,3,5,7,10];

[data_rows,data_cols]=size(conc_timepoint_means);

for r=1:data_rows
   for c=1:data_cols
      mean_vector=[nanmean(sequential{2*r-1,2*c-1}),nanmean(sequential{2*r,2*c-
1}),nanmean(sequential{2*r-1,2*c}),nanmean(sequential{2*r,2*c})];
      conc_timepoint_means(r,c)=nanmean(mean_vector);
      conc_timepoint_stds(r,c)=nanstd(mean_vector)/sqrt(length(mean_vector));
   end
end
normalize=nanmean(conc_timepoint_means(:,1));


for i=1:data_rows

errorbar(times,conc_timepoint_means(i,:)/normalize,conc_timepoint_stds(i,:)/normalize,'
Color',[0 0 0],'LineWidth',thicknesses(i))
   hold on
end
hold off
```

Histograms

```
load('C:\Users\Ezhang\RPMI_2.mat')
times=[0,2,3,5,7,10];
pERK=handles.Measurements.Cell_by_pERK.Intensity_MeanIntensity_pERK;
pERK=transpose(reshape(pERK,12,8));
pERK_sequential=horzcat(pERK(:,12),pERK(:,1:11));
pERK_conc_timepoint_pooled=cell(4,6);
[data_rows,data_cols]=size(pERK_conc_timepoint_pooled);
bins=[0:0.001:0.03];
i=1;
for r=2:data_rows
   for c=1:data_cols
      subplot(3,6,i)
      pERK_conc_timepoint_pooled{r,c}=vertcat(pERK_sequential{2*r-1,2*c-
1},pERK_sequential{2*r,2*c-1},pERK_sequential{2*r-
1,2*c},pERK_sequential{2*r,2*c});
bar=hist(pERK_conc_timepoint_pooled{r,c},bins)/sum(hist(pERK_conc_timepoint_pool
ed{r,c}));
      plot(bar,'k','LineWidth',1.5)
      i=i+1;
      axis([0 30 0 max(bar)])
   end
end
```

Covariation analysis

```
load('C:\Users\Ezhang\RPMI_2.mat')

feature=handles.Measurements.Cell_by_pERK.Intensity_MeanIntensity_pERK;
wells=handles.Measurements.Image.Metadata_Well;
feature=transpose(reshape(feature,12,8));
wells=transpose(reshape(wells,12,8));
sequential=horzcat(feature(:,12),feature(:,1:11));
sequential_wells=horzcat(wells(:,12),wells(:,1:11));
conc_timepoint_means=zeros(4,6);
conc_timepoint_stds=zeros(4,6);
times=[0,2,3,5,7,10];

[data_rows,data_cols]=size(conc_timepoint_means);

for r=1:data_rows
   for c=1:data_cols
```

```
      mean_vector=[nanmean(sequential{2*r-1,2*c-1}),nanmean(sequential{2*r,2*c-
1}),nanmean(sequential{2*r-1,2*c}),nanmean(sequential{2*r,2*c})];
      conc_timepoint_means(r,c)=nanmean(mean_vector);
      conc_timepoint_stds(r,c)=nanstd(mean_vector)/sqrt(length(mean_vector));
   end
end
normalize=nanmean(conc_timepoint_means(:,1));

%%
times=[0,2,3,5,7,10];

pERK=handles.Measurements.Cell_by_pERK.Intensity_MeanIntensity_pERK;
pERK=transpose(reshape(pERK,12,8));
pERK_sequential=horzcat(pERK(:,12),pERK(:,1:11));
pERK_conc_timepoint_pooled=cell(4,6);

pp38=handles.Measurements.Cell_by_pERK.Intensity_MeanIntensity_pp38;
pp38=transpose(reshape(pp38,12,8));
pp38_sequential=horzcat(pp38(:,12),pp38(:,1:11));
pp38_conc_timepoint_pooled=cell(4,6);


[data_rows,data_cols]=size(pERK_conc_timepoint_pooled);
i=1;
for r=2:data_rows
   for c=1:data_cols
      subplot(3,6,i)
      pERK_conc_timepoint_pooled{r,c}=vertcat(pERK_sequential{2*r-1,2*c-
1},pERK_sequential{2*r,2*c-1},pERK_sequential{2*r-
1,2*c},pERK_sequential{2*r,2*c});
      pp38_conc_timepoint_pooled{r,c}=vertcat(pp38_sequential{2*r-1,2*c-
1},pp38_sequential{2*r,2*c-1},pp38_sequential{2*r-1,2*c},pp38_sequential{2*r,2*c});

scatter(pp38_conc_timepoint_pooled{r,c}/normalize,pERK_conc_timepoint_pooled{r,c}
/normalize,'k.')
      axis([0 7 2 6])
      axis square
      set(gca,'XTick',[])
      set(gca,'YTick',[])

      i=i+1;
   end
end
```

APPENDIX C

A general protocol for quantifying single-cell fluorescence with CellProfiler

Author's note: I include these pages with the hope that easy access to this protocol via the university's Electronic Theses and Dissertation Portal will encourage other UT Southwestern students to incorporate quantitative image analysis into their projects.

Prerequisites: Immunofluorescent images of nuclei + protein that fills cell + protein of interest. Download CellProfiler from cellprofiler.org.

0. Go to "View output settings." Choose where to save your output.

INPUT MODULES

1. **Images**: Drag over your image files to your file list. Note: You can drag sets of whole folders.

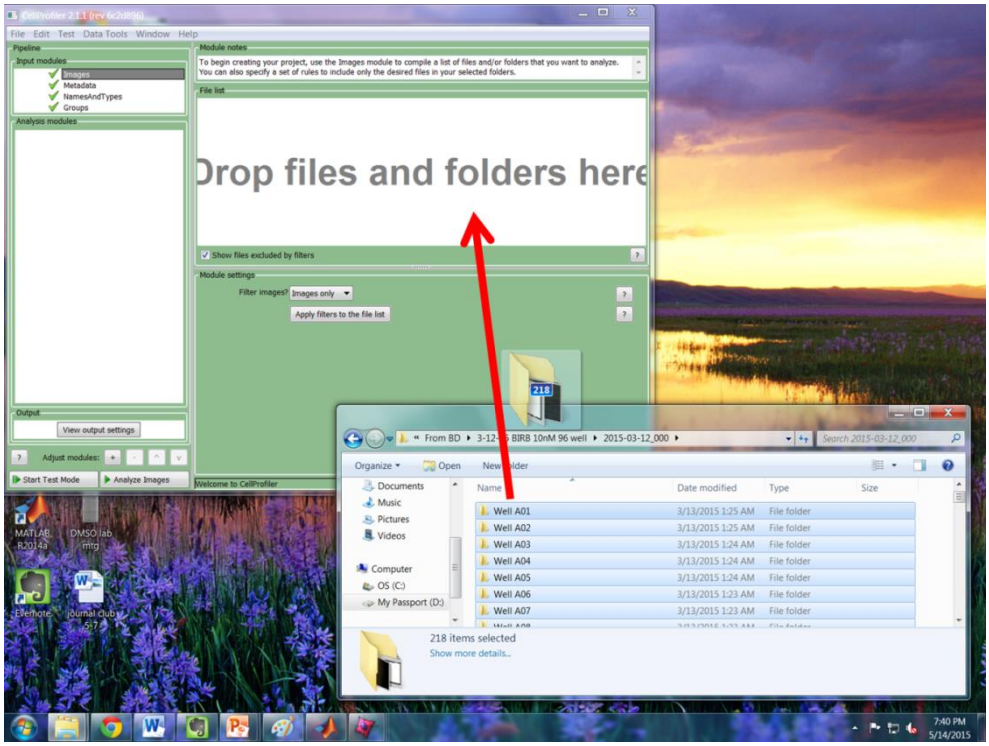

If you have more files in your folders than just the image files that you want to process, you can specify that in "Filter images?" For instance, if I had a bunch of files, but I only wanted to process the images with names like "Alexa 488 - n000000" or "DAPI - n000000," I could tell CellProfiler to grab only the files that had "n000" in their file names:

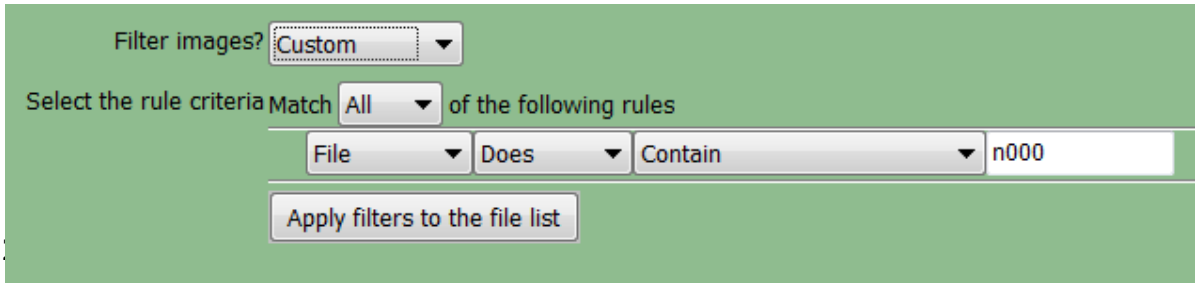

of which folders or files had which cells. This is useful if you've organized your images into folders for each well, as shown in the image for Step 1. Or, you could use

it if you don't have well folders, but your images themselves have information that you want to track, e.g. 'pERK_timepoint_1.jpg', 'pERK_timepoint_2.jpg', 'pERK_timepoint_3.jpg', etc..
(Otherwise, skip Metadata and proceed to NamesAndTypes.)

If you clicked "Yes," then, in "Metadata source," select "Extract from file/folder names"

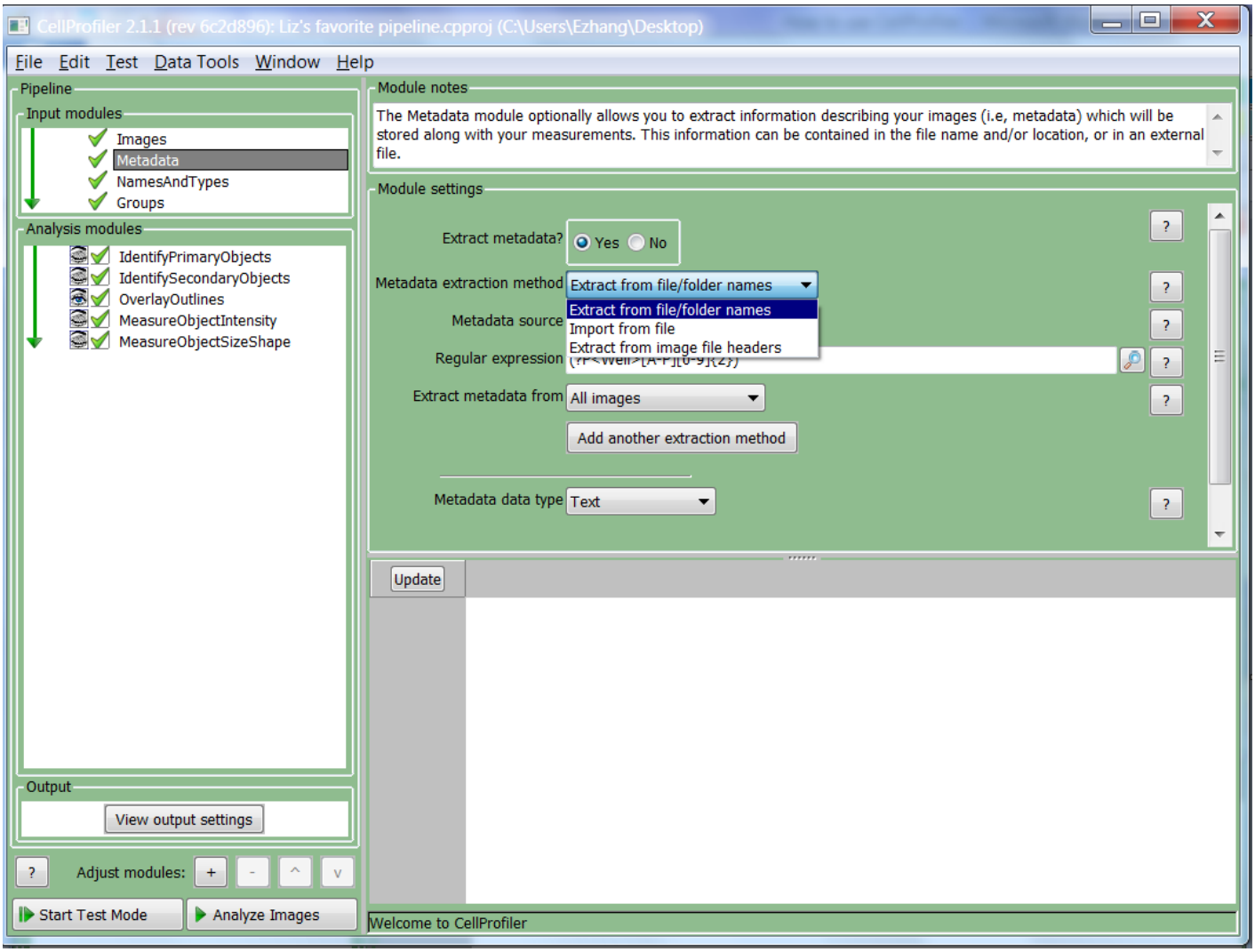

- Select whether you want your images tracked by their file names or the names of the folders they are in.

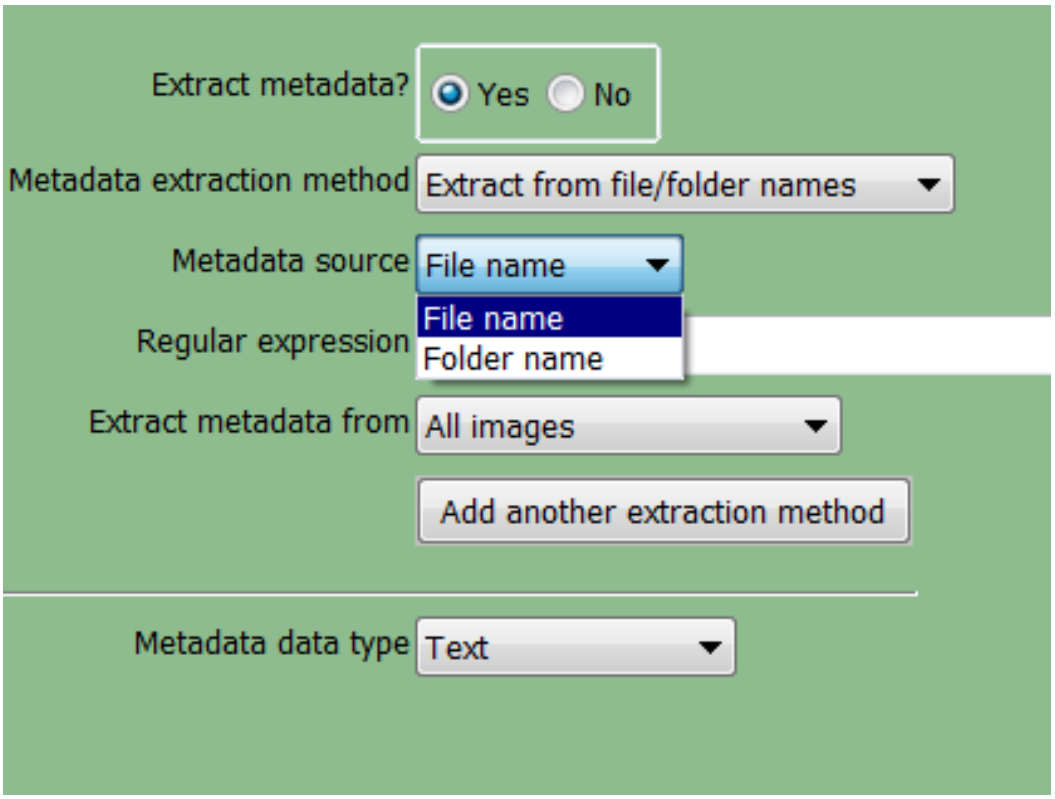

- In "Regular expression," tell CellProfiler how you named this information.
  - For instance, if you have a bunch of folders named by well like A01, A02, …, A12, B01, B02,…,B12, etc., your regular expression would be (?P<Well>[A-P][0-9]{2}).
  - Or, if you have a bunch of image files together, and they are named with some common name plus a trackable name like 20140164_ 00001, 20140164_ 00002, 20140164_ 00003…, and you wanted to track your images by the unique (so, the last 5) digits of that name, your regular expression would be 20140164_(?P<Site>[0-9]{5}).

NamesandTypes: Now tell CellProfiler how to relate your file names to proteins. In this example, I was telling CellProfiler that my naming convention was such that all of my files that had “647” in the file name were images of actin by phalloidin-647 staining, and all of my files that had “488” in the file name were images of pERK staining, etc.. Note that I also loaded and named my brightfield images – this will allow me to check my segmentation later.

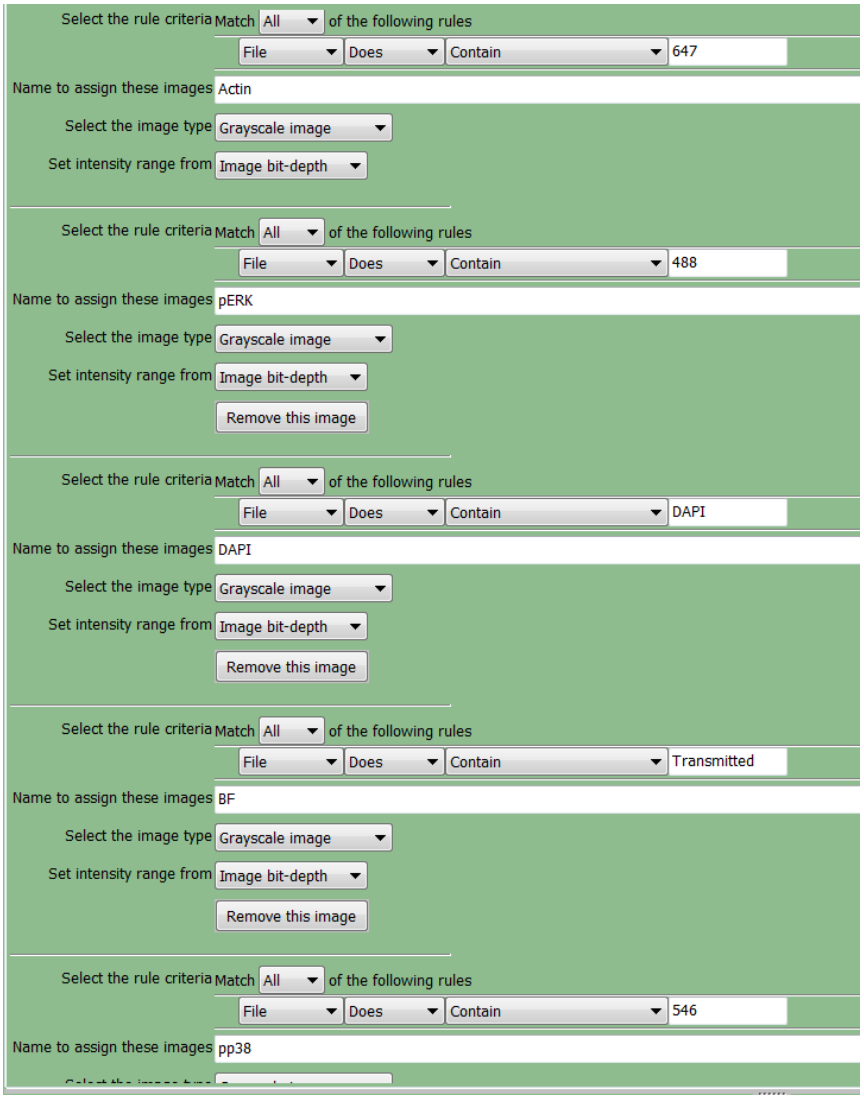

3. Continue on to making your Analysis Modules (skip “Groups.”)

ANALYSIS MODULES

1. Right-click on the empty modules list, and add "**IdentifyPrimaryObjects**"

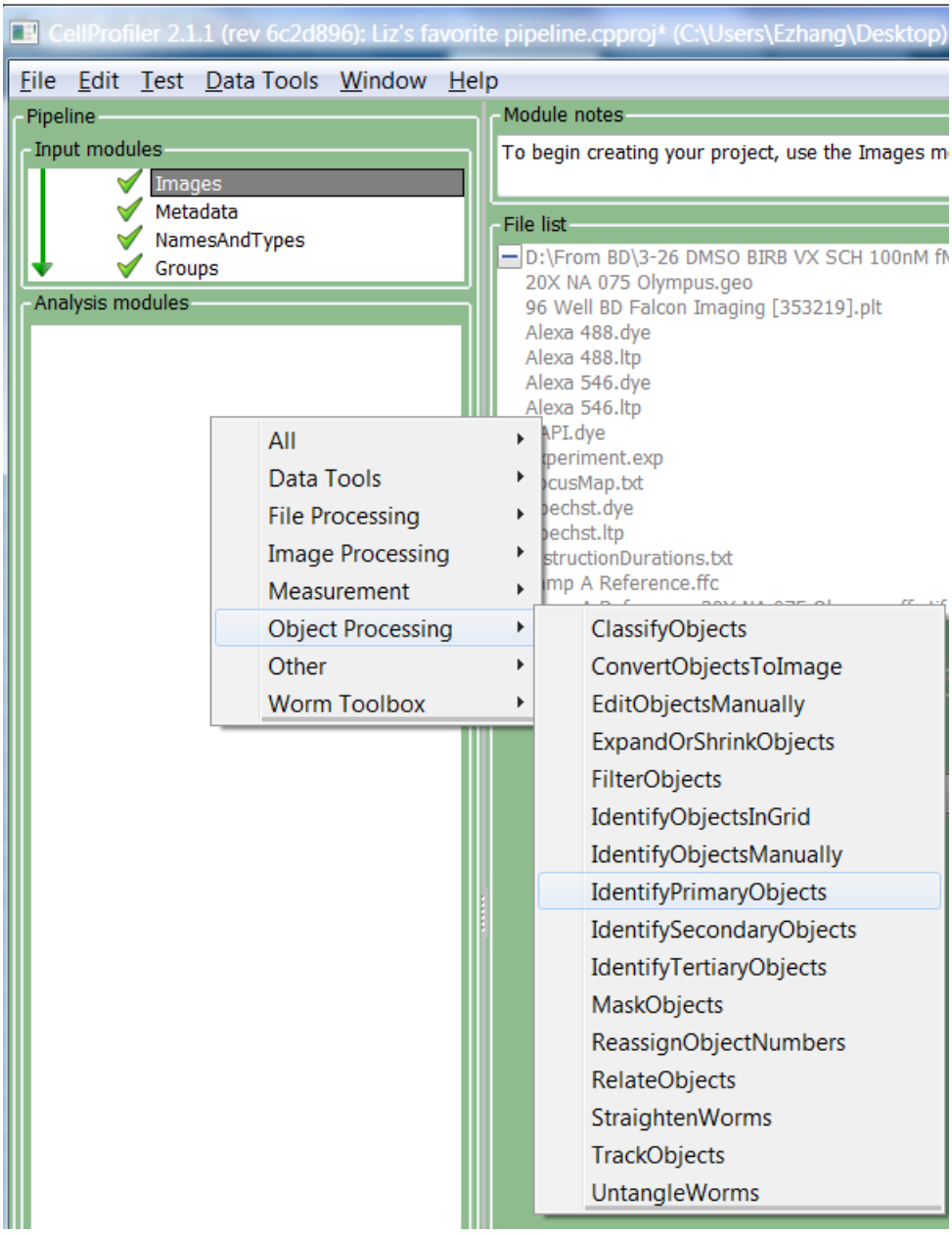

2. Use this module to tell CellProfiler to use your images of nuclear staining to identify the primary objects. Choose the typical diameter of nuclei based on your cell size and magnification. In this example, I was giving a ballpark range for nuclei of differentiated (neutrophil-like) HL-60 cells at 20x magnification. The below thresholding strategy works fine in my experience, but you can play around with the parameters, and see how well they work on this step by using the program's "test mode."

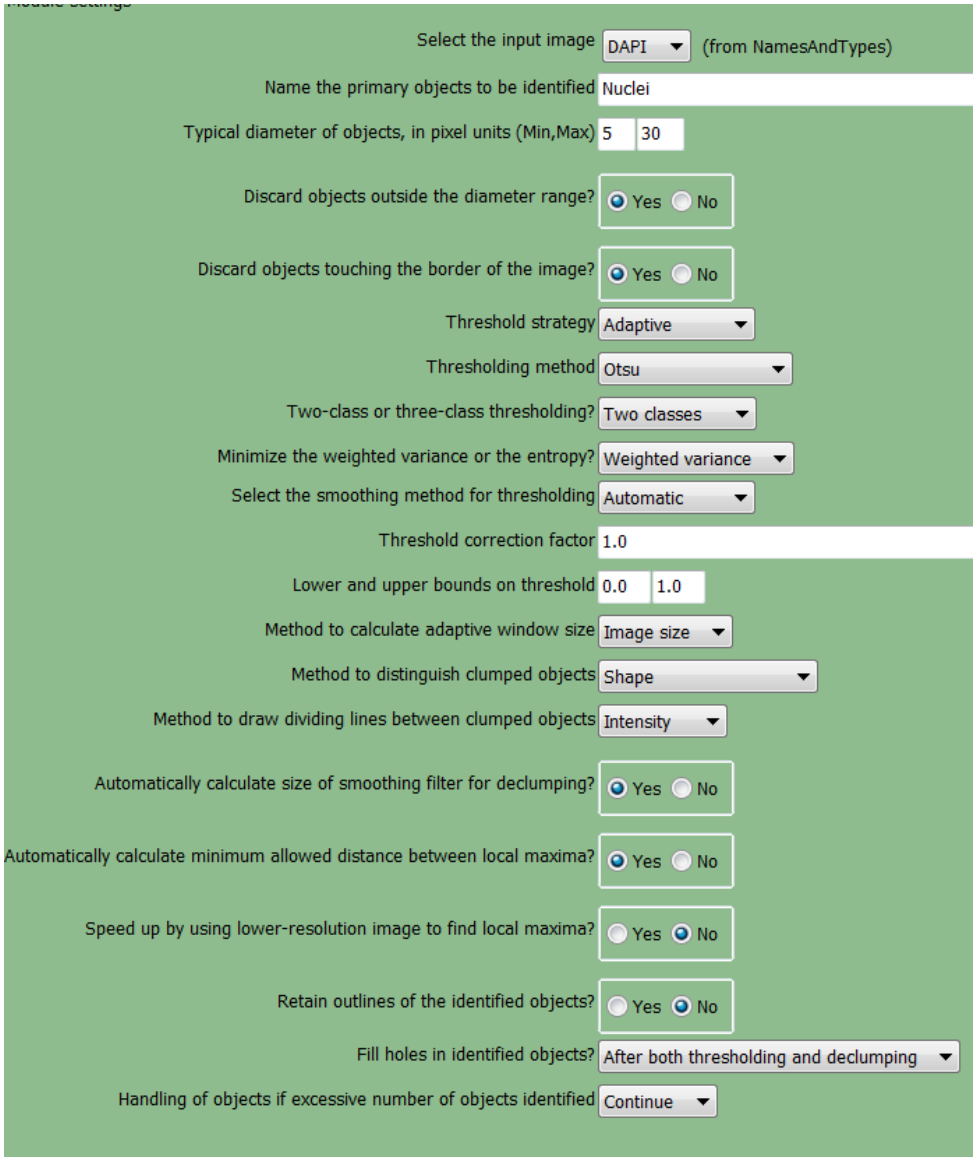

CellProfiler will in turn circle all bright spots meeting those criteria in the image:

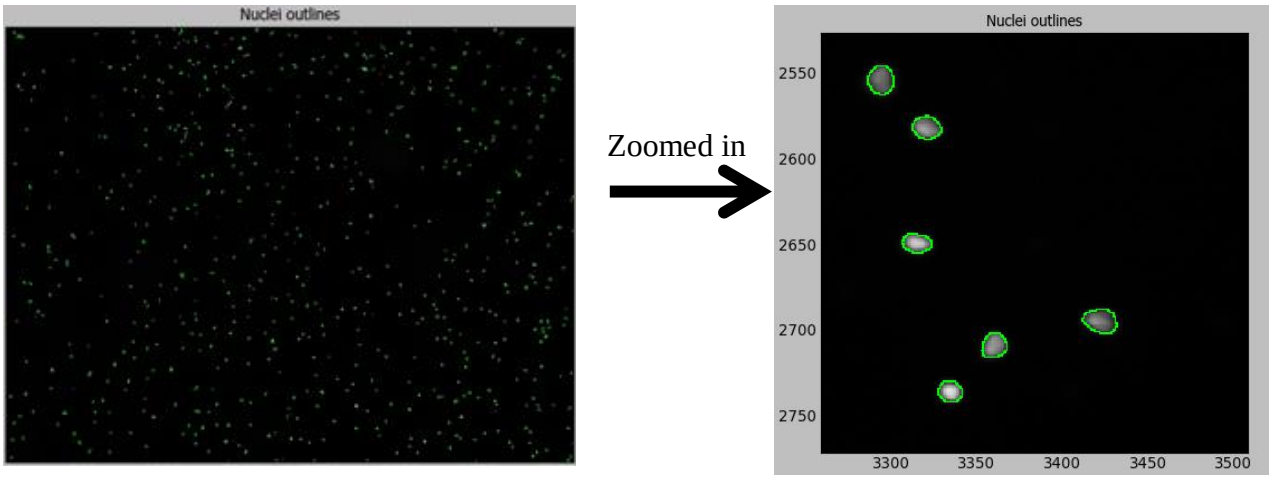

3. Add the module "**IdentifySecondaryObjects**" to tell CellProfiler to expand outward from these primary objects (nuclei) based on a marker that fills the cytoplasm. Here, I used my actin staining:

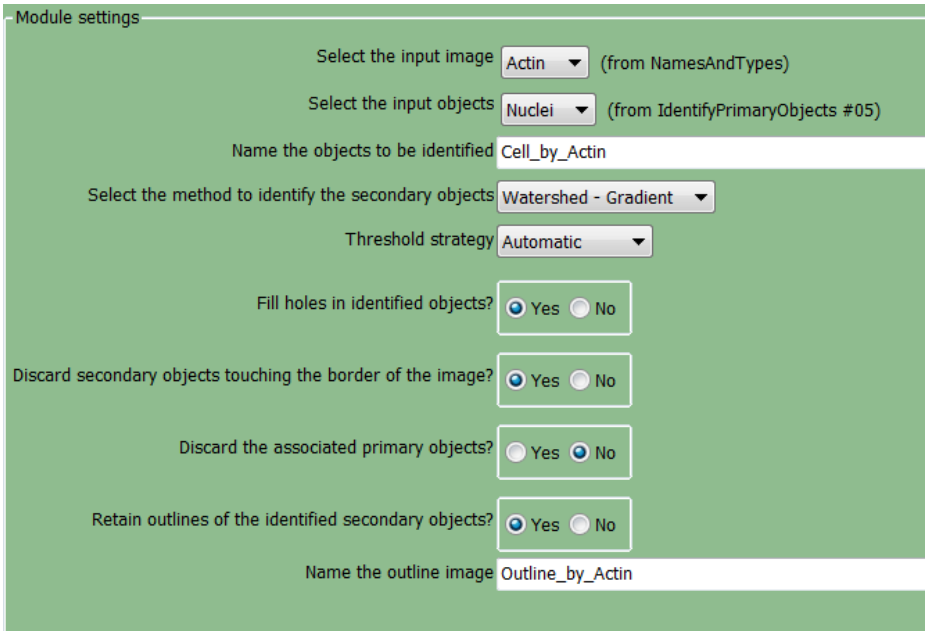

And this was the result:

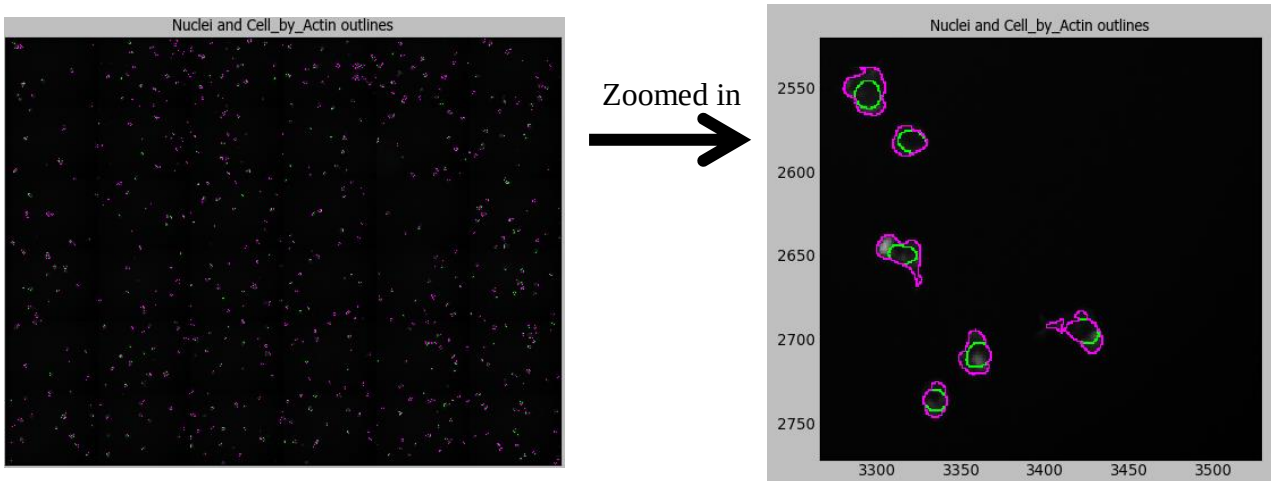

4. If you want to measure the cytoplasmic signal, excluding the nucleus of each cell, you can add the module "**IdentifyTertiaryObjects**" to define a tertiary object to fit that need – the cell found by actin signal in "IdentifySecondaryObjects" minus its corresponding nucleus from "IdentifyPrimaryObjects."

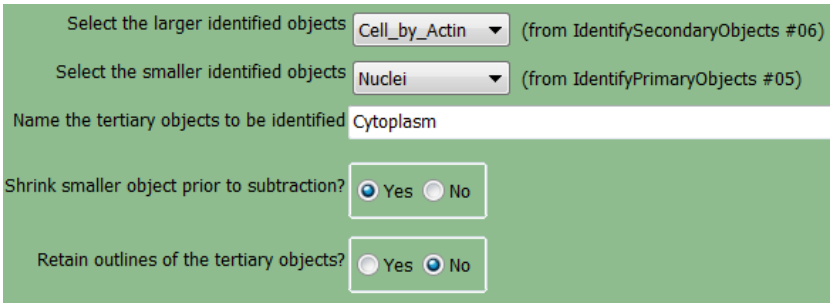

And this will be the result:

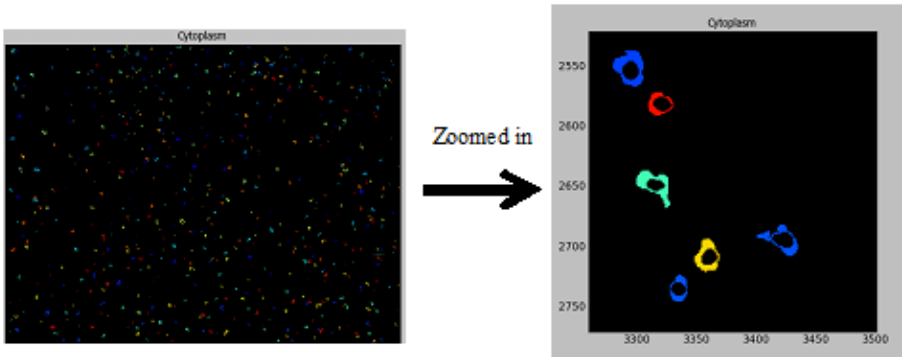

5. If you want to check the accuracy of the objects you defined (in other words, check your segmentation), you can use the "**OverlayOutlines**" module to overlay your outlines on your brightfield images.

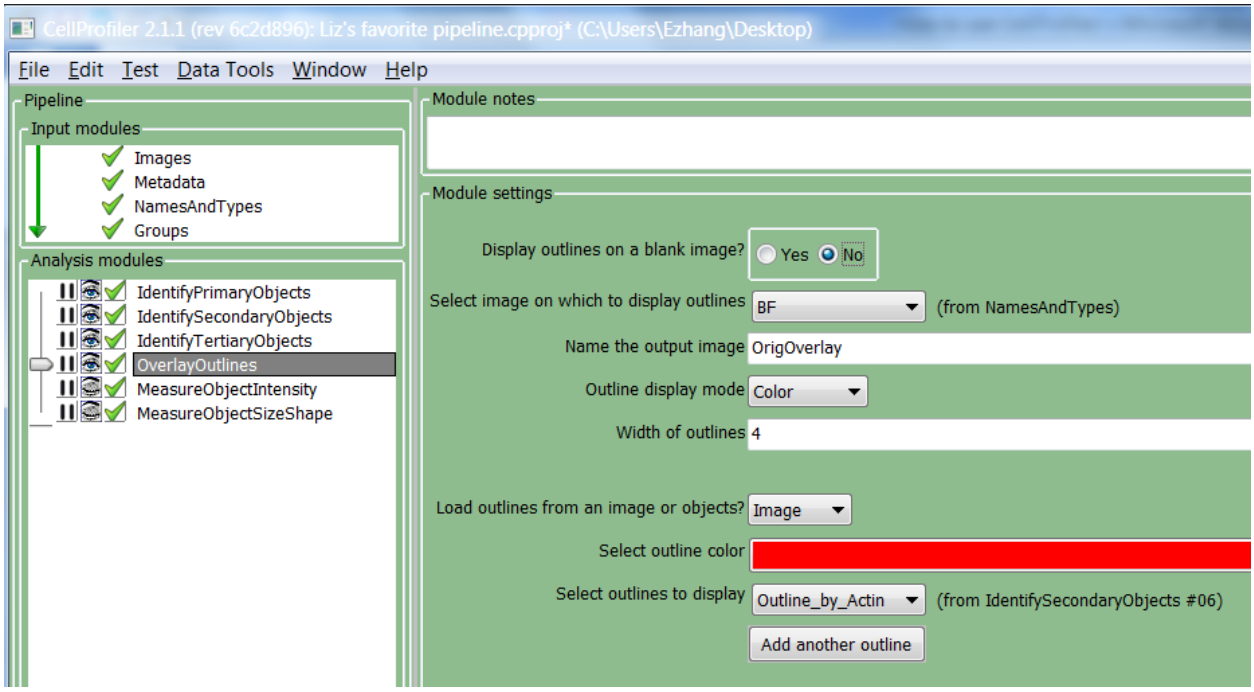

Result:

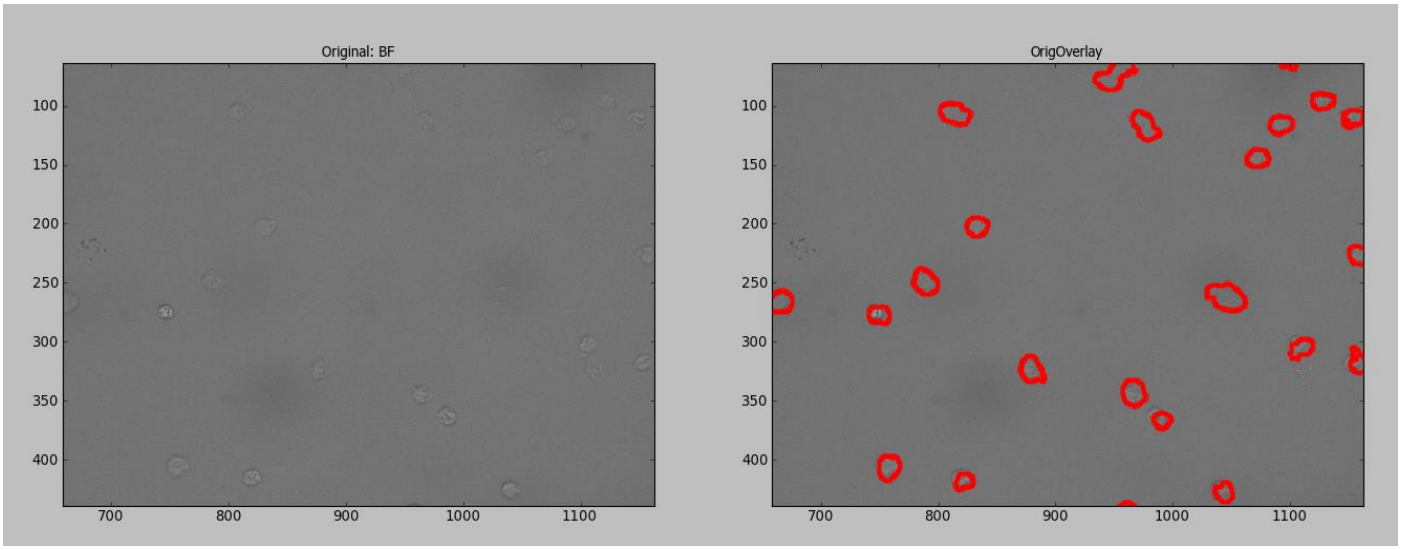

6. Now you can measure your protein of interest with "**MeasureObjectIntensity**." Pick the image with staining for your protein of interest as the "image to measure." Pick the part of the cell you want to measure that protein in as the "object to measure."

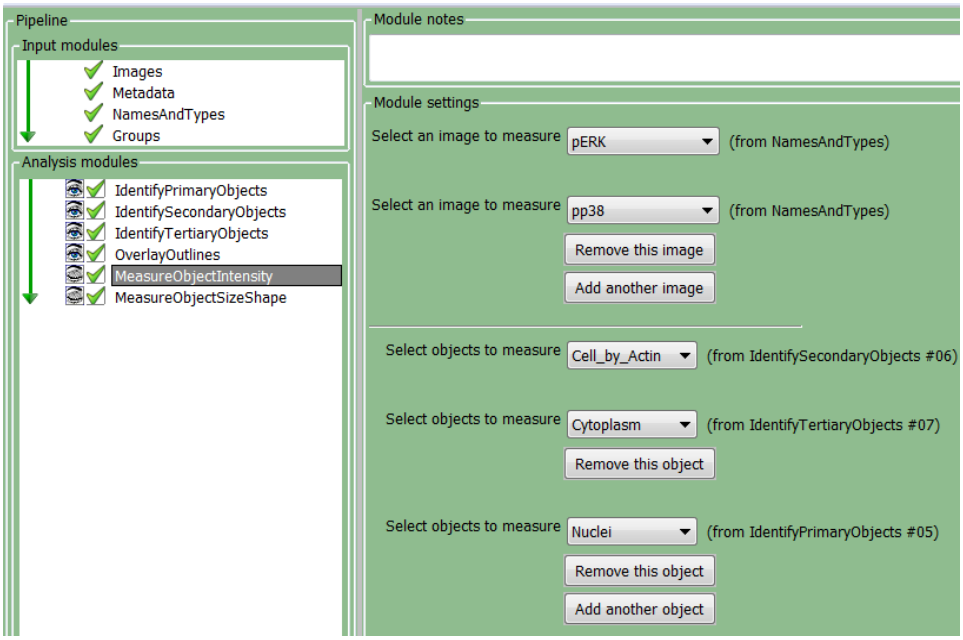

For each “object to measure” (whole cell, cytoplasm, nucleus), you’ll get a list of measurements for each marker you chose to measure.

Image	Object	Feature	Mean	Median	STD
pERK	Cell_by_Actin	IntegratedIntensity	1.804	1.545	1.181
pERK	Cell_by_Actin	MeanIntensity	nan	0.005	nan
pERK	Cell_by_Actin	StdIntensity	nan	0.001	nan
pERK	Cell_by_Actin	MinIntensity	0.004	0.004	0.001
pERK	Cell_by_Actin	MaxIntensity	0.007	0.006	0.008
pERK	Cell_by_Actin	IntegratedIntensityEdge	0.387	0.346	0.187
pERK	Cell_by_Actin	MeanIntensityEdge	nan	0.004	nan
pERK	Cell_by_Actin	StdIntensityEdge	nan	0.0	nan
pERK	Cell_by_Actin	MinIntensityEdge	0.004	0.004	0.001
pERK	Cell_by_Actin	MaxIntensityEdge	0.006	0.005	0.007
pERK	Cell_by_Actin	MassDisplacement	nan	0.258	nan
pERK	Cell_by_Actin	LowerQuartileIntensity	0.004	0.004	0.002
pERK	Cell_by_Actin	MedianIntensity	0.005	0.005	0.004
pERK	Cell_by_Actin	MADIntensity	0.001	0.0	0.001
pERK	Cell_by_Actin	UpperQuartileIntensity	0.006	0.005	0.006
pERK	Cell_by_Actin	CenterMassIntensity_X	nan	1845.117	nan
pERK	Cell_by_Actin	CenterMassIntensity_Y	nan	1393.812	nan
pERK	Cell_by_Actin	MaxIntensity_X	1894.051	1842.0	987.302
pERK	Cell_by_Actin	MaxIntensity_Y	1353.463	1388.0	839.933

7. If you are also interested in cell shape, you can use “**MeasureObjectSizeShape**.”

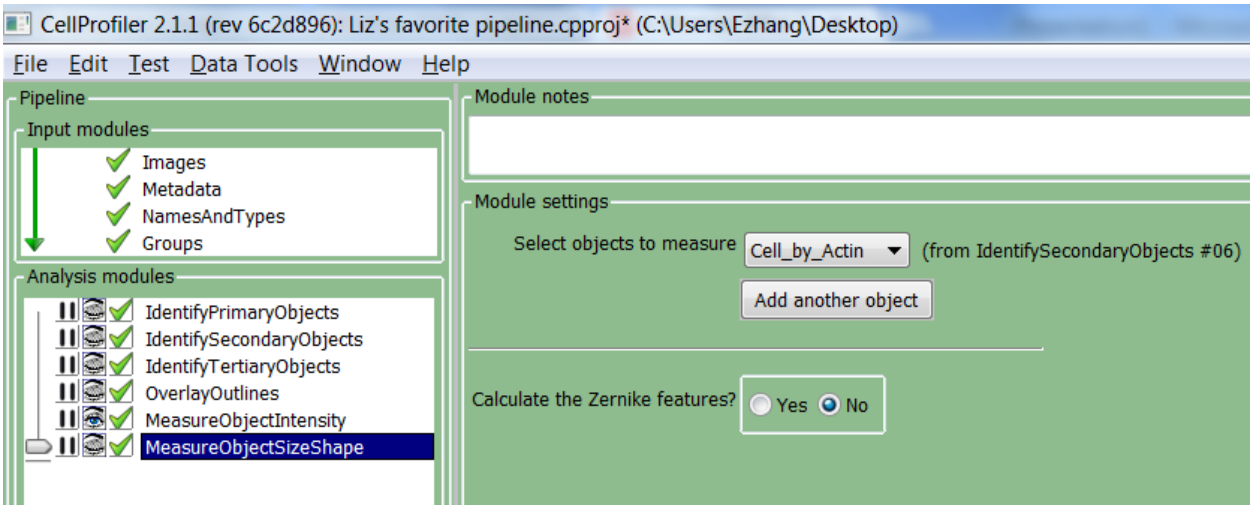

Result:

Object	Feature	Mean	Median	STD
Cell_by_Actin	Eccentricity	0.63	0.64	0.16
Cell_by_Actin	MajorAxisLength	25.67	23.46	8.13
Cell_by_Actin	MinorAxisLength	18.41	18.24	4.66
Cell_by_Actin	Orientation	-1.31	-1.87	50.12
Cell_by_Actin	Compactness	1.13	1.07	0.17
Cell_by_Actin	Area	370.21	335.00	178.35
Cell_by_Actin	Center_X	1893.62	1842.00	989.92
Cell_by_Actin	Center_Y	1353.52	1391.00	840.04
Cell_by_Actin	Extent	0.71	0.73	0.09
Cell_by_Actin	Perimeter	77.40	72.42	24.39
Cell_by_Actin	Solidity	0.91	0.93	0.05
Cell_by_Actin	FormFactor	0.77	0.80	0.14
Cell_by_Actin	EulerNumber	1.00	1.00	0.05
Cell_by_Actin	MaximumRadius	8.56	8.54	2.03
Cell_by_Actin	MeanRadius	3.42	3.40	0.69
Cell_by_Actin	MedianRadius	3.06	3.00	0.64
Cell_by_Actin	MinFeretDiameter	17.94	17.68	4.91
Cell_by_Actin	MaxFeretDiameter	25.47	23.54	8.24

8. Your pipeline is complete! Click “Start Test Mode” to try the pipeline on a small group of images. If you’re happy with the result, click “Analyze Images” to analyze your whole image set. If you have tons of images, it’ll take about an hour.

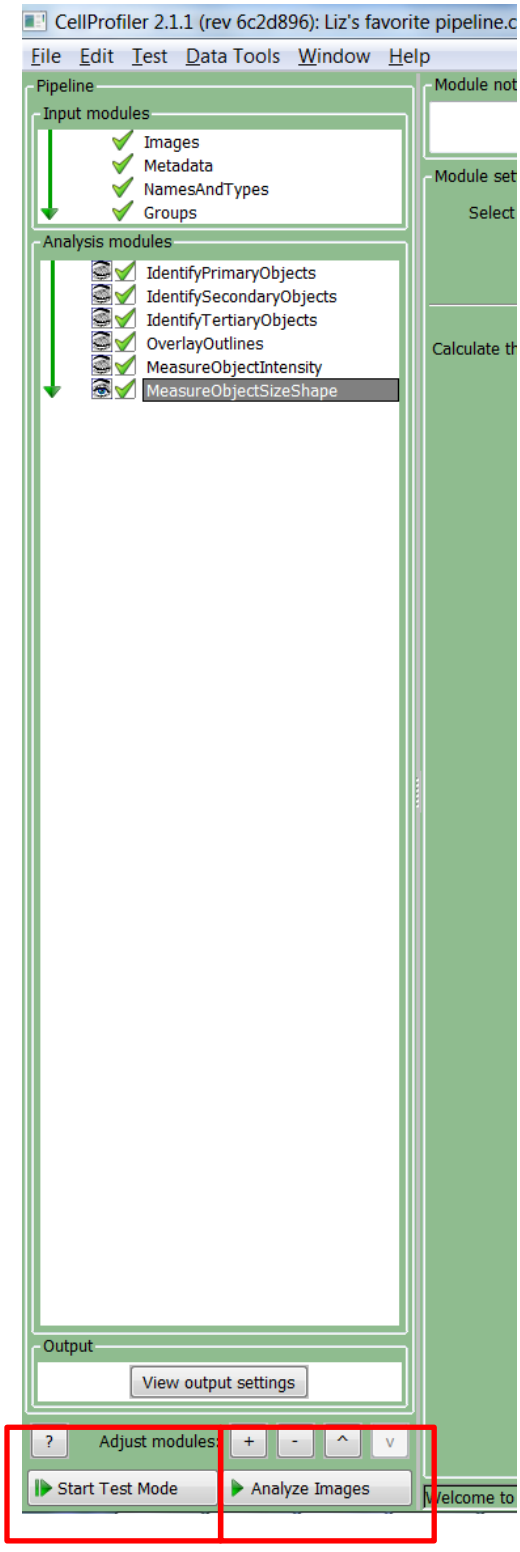

REFERENCES

1. Agner, K., *Detoxicating effect of verdoperoxidase on toxins.* Nature, 1947. **159**(4034): p. 271.
2. Alberts B, J.A., Lewis J, et al. , *Molecular Biology of the Cell. 4th edition.*2002, New York, US: Garland Science.
3. Amano, M., M. Ito, K. Kimura, Y. Fukata, K. Chihara, T. Nakano, Y. Matsuura, and K. Kaibuchi, *Phosphorylation and activation of myosin by Rho-associated kinase (Rho-kinase).* J Biol Chem, 1996. **271**(34): p. 20246-9.
4. Azzali, G., G. Orlandini, and R. Gatti, *The migration of lymphocytes and polymorphonuclear leukocytes across the endothelial wall of the absorbing peripheral lymphatic vessel.* J Submicrosc Cytol Pathol, 1990. **22**(4): p. 543-9.
5. Bain, J., L. Plater, M. Elliott, N. Shpiro, C.J. Hastie, H. McLauchlan, I. Klevernic, J.S. Arthur, D.R. Alessi, and P. Cohen, *The selectivity of protein kinase inhibitors: a further update.* Biochem J, 2007. **408**(3): p. 297-315.
6. Baratt, A., S.N. Arkhipov, and I.V. Maly, *An experimental and computational study of effects of microtubule stabilization on T-cell polarity.* PLoS One, 2008. **3**(12): p. e3861.
7. Barnhart, E.L., K.C. Lee, K. Keren, A. Mogilner, and J.A. Theriot, *An adhesion-dependent switch between mechanisms that determine motile cell shape.* PLoS Biol, 2011. **9**(5): p. e1001059.

8. Bement, W.M., H.A. Benink, and G. von Dassow, *A microtubule-dependent zone of active RhoA during cleavage plane specification.* J Cell Biol, 2005. **170**(1): p. 91-101.

9. Benard, V., B.P. Bohl, and G.M. Bokoch, *Characterization of rac and cdc42 activation in chemoattractant-stimulated human neutrophils using a novel assay for active GTPases.* J Biol Chem, 1999. **274**(19): p. 13198-204.

10. Boxer, L.A., E.T. Hedley-Whyte, and T.P. Stossel, *Neutrophil action dysfunction and abnormal neutrophil behavior.* N Engl J Med, 1974. **291**(21): p. 1093-9.

11. Boyum, A., *Isolation of mononuclear cells and granulocytes from human blood. Isolation of monuclear cells by one centrifugation, and of granulocytes by combining centrifugation and sedimentation at 1 g.* Scand J Clin Lab Invest Suppl, 1968. **97**: p. 77-89.

12. Briscoe, C., J. Moniakis, J.Y. Kim, J.M. Brown, D. Hereld, P.N. Devreotes, and R.A. Firtel, *The phosphorylated C-terminus of cAR1 plays a role in cell-type-specific gene expression and STATa tyrosine phosphorylation.* Dev Biol, 2001. **233**(1): p. 225-36.

13. Brittain, J., *Thevenin's theorem.* Spectrum, IEEE, 1990. **27**(3): p. 42.

14. Brzostowski, J.A., S. Sawai, O. Rozov, X.H. Liao, D. Imoto, C.A. Parent, and A.R. Kimmel, *Phosphorylation of chemoattractant receptors regulates chemotaxis, actin reorganization and signal relay.* J Cell Sci, 2013. **126**(Pt 20): p. 4614-26.

15. Cagatay, T., M. Turcotte, M.B. Elowitz, J. Garcia-Ojalvo, and G.M. Suel, *Architecture-dependent noise discriminates functionally analogous differentiation circuits.* Cell, 2009. **139**(3): p. 512-22.

16. Capodici, C., M.H. Pillinger, G. Han, M.R. Philips, and G. Weissmann, *Integrin-dependent homotypic adhesion of neutrophils. Arachidonic acid activates Raf-1/Mek/Erk via a 5-lipoxygenase- dependent pathway.* J Clin Invest, 1998. **102**(1): p. 165-75.

17. Cardona, A., S. Saalfeld, S. Preibisch, B. Schmid, A. Cheng, J. Pulokas, P. Tomancak, and V. Hartenstein, *An integrated micro- and macroarchitectural analysis of the Drosophila brain by computer-assisted serial section electron microscopy.* PLoS Biol, 2010. **8**(10).

18. Carpenter, A.E., T.R. Jones, M.R. Lamprecht, C. Clarke, I.H. Kang, O. Friman, D.A. Guertin, J.H. Chang, R.A. Lindquist, J. Moffat, P. Golland, and D.M. Sabatini, *CellProfiler: image analysis software for identifying and quantifying cell phenotypes.* Genome Biol, 2006. **7**(10): p. R100.

19. Chaikuad, A., E.M. Tacconi, J. Zimmer, Y. Liang, N.S. Gray, M. Tarsounas, and S. Knapp, *A unique inhibitor binding site in ERK1/2 is associated with slow binding kinetics.* Nat Chem Biol, 2014. **10**(10): p. 853-60.

20. Chau, A.H., J.M. Walter, J. Gerardin, C. Tang, and W.A. Lim, *Designing synthetic regulatory networks capable of self-organizing cell polarization.* Cell, 2012. **151**(2): p. 320-32.

21. Coates, T.D., J.C. Torkildson, M. Torres, J.A. Church, and T.H. Howard, *An inherited defect of neutrophil motility and microfilamentous cytoskeleton associated with abnormalities in 47-Kd and 89-Kd proteins.* Blood, 1991. **78**(5): p. 1338-46.

22. Conway Morris, A., K. Kefala, T.S. Wilkinson, K. Dhaliwal, L. Farrell, T. Walsh, S.J. Mackenzie, H. Reid, D.J. Davidson, C. Haslett, A.G. Rossi, J.M. Sallenave, and A.J. Simpson, *C5a mediates peripheral blood neutrophil dysfunction in critically ill patients.* Am J Respir Crit Care Med, 2009. **180**(1): p. 19-28.

23. Dandekar, S.N., J.S. Park, G.E. Peng, J.J. Onuffer, W.A. Lim, and O.D. Weiner, *Actin dynamics rapidly reset chemoattractant receptor sensitivity following adaptation in neutrophils.* Philos Trans R Soc Lond B Biol Sci, 2013. **368**(1629): p. 20130008.

24. Darwin, F., *On the Primary Vascular Dilatation in Acute Inflammation.* J Anat Physiol, 1875. **10**(Pt 1): p. 1-16.

25. Devreotes, P. and C. Janetopoulos, *Eukaryotic chemotaxis: distinctions between directional sensing and polarization.* J Biol Chem, 2003. **278**(23): p. 20445-8.

26. Devreotes, P.N. and S.H. Zigmond, *Chemotaxis in eukaryotic cells: a focus on leukocytes and Dictyostelium.* Annu Rev Cell Biol, 1988. **4**: p. 649-86.

27. Dowler, T., *On the Product of Acute Inflammation.* Med Chir Trans, 1823. **12**(Pt 1): p. 86-93.

28. Downey, G.P., J.R. Butler, H. Tapper, L. Fialkow, A.R. Saltiel, B.B. Rubin, and S. Grinstein, *Importance of MEK in neutrophil microbicidal responsiveness.* J Immunol, 1998. **160**(1): p. 434-43.

29. Driscoll, M.K., C. McCann, R. Kopace, T. Homan, J.T. Fourkas, C. Parent, and W. Losert, *Cell shape dynamics: from waves to migration.* PLoS Comput Biol, 2012. **8**(3): p. e1002392.

30. Ebbinghaus, M. and L. Santen, *Theoretical modeling of aging effects in microtubule dynamics.* Biophys J, 2011. **100**(4): p. 832-8.

31. Eddy, R.J., L.M. Pierini, F. Matsumura, and F.R. Maxfield, *Ca2+-dependent myosin II activation is required for uropod retraction during neutrophil migration.* J Cell Sci, 2000. **113 (Pt 7)**: p. 1287-98.

32. Eddy, R.J., L.M. Pierini, and F.R. Maxfield, *Microtubule asymmetry during neutrophil polarization and migration.* Mol Biol Cell, 2002. **13**(12): p. 4470-83.

33. Efimova, T., A.M. Broome, and R.L. Eckert, *A regulatory role for p38 delta MAPK in keratinocyte differentiation. Evidence for p38 delta-ERK1/2 complex formation.* J Biol Chem, 2003. **278**(36): p. 34277-85.

34. Ehrengruber, M.U., D.A. Deranleau, and T.D. Coates, *Shape oscillations of human neutrophil leukocytes: characterization and relationship to cell motility.* J Exp Biol, 1996. **199**(Pt 4): p. 741-7.

35. El Benna, J., J. Han, J.W. Park, E. Schmid, R.J. Ulevitch, and B.M. Babior, *Activation of p38 in stimulated human neutrophils: phosphorylation of the*

oxidase component p47phox by p38 and ERK but not by JNK. Arch Biochem Biophys, 1996. **334**(2): p. 395-400.

36. Ferrell, J.E., Jr. and E.M. Machleder, *The biochemical basis of an all-or-none cell fate switch in Xenopus oocytes.* Science, 1998. **280**(5365): p. 895-8.

37. Fletcher, G.B.A., *The Loeb Edition of Celsus Celsus. De Medicina. With an English translation by W. G. Spencer. In two volumes. I. [Books I–IV.] Pp. xiv + 499. (Loeb Classical Library.) London: Heinemann, 1935. Cloth, 10s. (leather, 12s. 6d.).* The Classical Review, 1936. **50**(01): p. 27-27.

38. Flyvbjerg, H., T.E. Holy, and S. Leibler, *Stochastic dynamics of microtubules: A model for caps and catastrophes.* Phys Rev Lett, 1994. **73**(17): p. 2372-2375.

39. Galic, M., S. Jeong, F.C. Tsai, L.M. Joubert, Y.I. Wu, K.M. Hahn, Y. Cui, and T. Meyer, *External push and internal pull forces recruit curvature-sensing N-BAR domain proteins to the plasma membrane.* Nat Cell Biol, 2012. **14**(8): p. 874-81.

40. Gamba, A., A. de Candia, S. Di Talia, A. Coniglio, F. Bussolino, and G. Serini, *Diffusion-limited phase separation in eukaryotic chemotaxis.* Proc Natl Acad Sci U S A, 2005. **102**(47): p. 16927-32.

41. Gauthier, J.F., A. Fortin, Y. Bergeron, M.C. Dumas, M.E. Champagne, and M.G. Bergeron, *Differential contribution of bacterial N-formyl-methionyl-leucyl-phenylalanine and host-derived CXC chemokines to neutrophil infiltration into pulmonary alveoli during murine pneumococcal pneumonia.* Infect Immun, 2007. **75**(11): p. 5361-7.

42. Gay, G., T. Courtheoux, C. Reyes, S. Tournier, and Y. Gachet, *A stochastic model of kinetochore-microtubule attachment accurately describes fission yeast chromosome segregation.* J Cell Biol, 2012. **196**(6): p. 757-74.

43. Geva-Zatorsky, N., N. Rosenfeld, S. Itzkovitz, R. Milo, A. Sigal, E. Dekel, T. Yarnitzky, Y. Liron, P. Polak, G. Lahav, and U. Alon, *Oscillations and variability in the p53 system.* Mol Syst Biol, 2006. **2**: p. 2006 0033.

44. Gohla, A., R. Harhammer, and G. Schultz, *The G-protein G13 but not G12 mediates signaling from lysophosphatidic acid receptor via epidermal growth factor receptor to Rho.* J Biol Chem, 1998. **273**(8): p. 4653-9.

45. Goldstein, D.M., A. Kuglstatter, Y. Lou, and M.J. Soth, *Selective p38alpha inhibitors clinically evaluated for the treatment of chronic inflammatory disorders.* J Med Chem, 2010. **53**(6): p. 2345-53.

46. Guo, R.F., N.C. Riedemann, K.D. Bernacki, V.J. Sarma, I.J. Laudes, J.S. Reuben, E.M. Younkin, T.A. Neff, J.D. Paulauskis, F.S. Zetoune, and P.A. Ward, *Neutrophil C5a receptor and the outcome in a rat model of sepsis.* FASEB J, 2003. **17**(13): p. 1889-91.

47. Hall-Jackson, C.A., M. Goedert, P. Hedge, and P. Cohen, *Effect of SB 203580 on the activity of c-Raf in vitro and in vivo.* Oncogene, 1999. **18**(12): p. 2047-54.

48. Hautaniemi, S., S. Kharait, A. Iwabu, A. Wells, and D.A. Lauffenburger, *Modeling of signal-response cascades using decision tree analysis.* Bioinformatics, 2005. **21**(9): p. 2027-35.

49. Heit, B., S. Tavener, E. Raharjo, and P. Kubes, *An intracellular signaling hierarchy determines direction of migration in opposing chemotactic gradients.* J Cell Biol, 2002. **159**(1): p. 91-102.

50. Hereld, D., R. Vaughan, J.Y. Kim, J. Borleis, and P. Devreotes, *Localization of ligand-induced phosphorylation sites to serine clusters in the C-terminal domain of the Dictyostelium cAMP receptor, cAR1.* J Biol Chem, 1994. **269**(9): p. 7036-44.

51. Hill, H.R., J.M. Gerrard, N.A. Hogan, and P.G. Quie, *Hyperactivity of neutrophil leukotactic responses during active bacterial infection.* J Clin Invest, 1974. **53**(4): p. 996-1002.

52. Hill, H.R., H.D. Ochs, P.G. Quie, R.A. Clark, H.F. Pabst, S.J. Klebanoff, and R.J. Wedgwood, *Defect in neutrophil granulocyte chemotaxis in Job's syndrome of recurrent "cold" staphylococcal abscesses.* Lancet, 1974. **2**(7881): p. 617-9.

53. Hirsch, J.G. and Z.A. Cohn, *Degranulation of polymorphonuclear leucocytes following phagocytosis of microorganisms.* J Exp Med, 1960. **112**: p. 1005-14.

54. Howard, T., Y. Li, M. Torres, A. Guerrero, and T. Coates, *The 47-kD protein increased in neutrophil actin dysfunction with 47- and 89-kD protein abnormalities is lymphocyte-specific protein.* Blood, 1994. **83**(1): p. 231-41.

55. Huber-Lang, M.S., E.M. Younkin, J.V. Sarma, S.R. McGuire, K.T. Lu, R.F. Guo, V.A. Padgaonkar, J.T. Curnutte, R. Erickson, and P.A. Ward, *Complement-induced impairment of innate immunity during sepsis.* J Immunol, 2002. **169**(6): p. 3223-31.

56. Hunter, J., *A treatise on the blood, inflammation, and gunshot wounds*. Vol. 945. 1840: Haswell, Barrington, and Haswell.

57. Inoue, T. and T. Meyer, *Synthetic activation of endogenous PI3K and Rac identifies an AND-gate switch for cell polarization and migration.* PLoS One, 2008. **3**(8): p. e3068.

58. Irimia, D., G. Balazsi, N. Agrawal, and M. Toner, *Adaptive-control model for neutrophil orientation in the direction of chemical gradients.* Biophys J, 2009. **96**(10): p. 3897-916.

59. Ishizaki, T., M. Naito, K. Fujisawa, M. Maekawa, N. Watanabe, Y. Saito, and S. Narumiya, *p160ROCK, a Rho-associated coiled-coil forming protein kinase, works downstream of Rho and induces focal adhesions.* FEBS Lett, 1997. **404**(2-3): p. 118-24.

60. Janes, K.A., C.C. Wang, K.J. Holmberg, K. Cabral, and J.S. Brugge, *Identifying single-cell molecular programs by stochastic profiling.* Nat Methods, 2010. **7**(4): p. 311-7.

61. Ji, L., J. Lim, and G. Danuser, *Fluctuations of intracellular forces during cell protrusion.* Nat Cell Biol, 2008. **10**(12): p. 1393-400.

62. Jilkine, A., A.F. Maree, and L. Edelstein-Keshet, *Mathematical model for spatial segregation of the Rho-family GTPases based on inhibitory crosstalk.* Bull Math Biol, 2007. **69**(6): p. 1943-78.

63. Jin, T., N. Zhang, Y. Long, C.A. Parent, and P.N. Devreotes, *Localization of the G protein betagamma complex in living cells during chemotaxis.* Science, 2000. **287**(5455): p. 1034-6.

64. Jones, T.W., *Observations on the State of the Blood and the Blood-Vessels in Inflammation.* Med Chir Trans, 1853. **36**: p. 391-402.

65. Jongstra-Bilen, J., V.L. Misener, C. Wang, H. Ginzberg, A. Auerbach, A.L. Joyner, G.P. Downey, and J. Jongstra, *LSP1 modulates leukocyte populations in resting and inflamed peritoneum.* Blood, 2000. **96**(5): p. 1827-35.

66. Kahle, N.A., G. Brenner-Weiss, J. Overhage, U. Obst, and G.M. Hansch, *Bacterial quorum sensing molecule induces chemotaxis of human neutrophils via induction of p38 and leukocyte specific protein 1 (LSP1).* Immunobiology, 2013. **218**(2): p. 145-51.

67. Keren, K., Z. Pincus, G.M. Allen, E.L. Barnhart, G. Marriott, A. Mogilner, and J.A. Theriot, *Mechanism of shape determination in motile cells.* Nature, 2008. **453**(7194): p. 475-80.

68. Kharait, S., S. Hautaniemi, S. Wu, A. Iwabu, D.A. Lauffenburger, and A. Wells, *Decision tree modeling predicts effects of inhibiting contractility signaling on cell motility.* BMC Syst Biol, 2007. **1**: p. 9.

69. Kim, J.Y., R.D. Soede, P. Schaap, R. Valkema, J.A. Borleis, P.J. Van Haastert, P.N. Devreotes, and D. Hereld, *Phosphorylation of chemoattractant receptors is not essential for chemotaxis or termination of G-protein-mediated responses.* J Biol Chem, 1997. **272**(43): p. 27313-8.

70. Kimura, K., M. Ito, M. Amano, K. Chihara, Y. Fukata, M. Nakafuku, B. Yamamori, J. Feng, T. Nakano, K. Okawa, A. Iwamatsu, and K. Kaibuchi, *Regulation of myosin phosphatase by Rho and Rho-associated kinase (Rho-kinase).* Science, 1996. **273**(5272): p. 245-8.

71. Klebanoff, S.J., *Myeloperoxidase: contribution to the microbicidal activity of intact leukocytes.* Science, 1970. **169**(3950): p. 1095-7.

72. Klinker, J.F., K. Wenzel-Seifert, and R. Seifert, *G-protein-coupled receptors in HL-60 human leukemia cells.* Gen Pharmacol, 1996. **27**(1): p. 33-54.

73. Kollmann, M., L. Lovdok, K. Bartholome, J. Timmer, and V. Sourjik, *Design principles of a bacterial signalling network.* Nature, 2005. **438**(7067): p. 504-7.

74. Korb, A., M. Tohidast-Akrad, E. Cetin, R. Axmann, J. Smolen, and G. Schett, *Differential tissue expression and activation of p38 MAPK alpha, beta, gamma, and delta isoforms in rheumatoid arthritis.* Arthritis Rheum, 2006. **54**(9): p. 2745-56.

75. Ku, C.J., Y. Wang, B. Pavie, S.J. Altschuler, and L.F. Wu, *On Identifying Information from Image-Based Spatial Polarity Phenotypes in Neutrophils.* Proc IEEE Int Symp Biomed Imaging, 2010. **14-17**: p. 1029-1032.

76. Ku, C.J., Y. Wang, O.D. Weiner, S.J. Altschuler, and L.F. Wu, *Network crosstalk dynamically changes during neutrophil polarization.* Cell, 2012. **149**(5): p. 1073-83.

77. Kuchina, A., L. Espinar, T. Cagatay, A.O. Balbin, F. Zhang, A. Alvarado, J. Garcia-Ojalvo, and G.M. Suel, *Temporal competition between differentiation programs determines cell fate choice.* Mol Syst Biol, 2011. **7**: p. 557.

78. Kuma, Y., G. Sabio, J. Bain, N. Shpiro, R. Marquez, and A. Cuenda, *BIRB796 inhibits all p38 MAPK isoforms in vitro and in vivo.* J Biol Chem, 2005. **280**(20): p. 19472-9.

79. Kumar, S., J. Xu, C. Perkins, F. Guo, S. Snapper, F.D. Finkelman, Y. Zheng, and M.D. Filippi, *Cdc42 regulates neutrophil migration via crosstalk between WASp, CD11b, and microtubules.* Blood, 2012. **120**(17): p. 3563-74.

80. Kunida, K., M. Matsuda, and K. Aoki, *FRET imaging and statistical signal processing reveal positive and negative feedback loops regulating the morphology of randomly migrating HT-1080 cells.* J Cell Sci, 2012. **125**(Pt 10): p. 2381-92.

81. Kwan, K.M. and M.W. Kirschner, *A microtubule-binding Rho-GEF controls cell morphology during convergent extension of Xenopus laevis.* Development, 2005. **132**(20): p. 4599-610.

82. Levchenko, A. and P.A. Iglesias, *Models of eukaryotic gradient sensing: application to chemotaxis of amoebae and neutrophils.* Biophys J, 2002. **82**(1 Pt 1): p. 50-63.

83. Li, Y., A. Guerrero, and T.H. Howard, *The actin-binding protein, lymphocyte-specific protein 1, is expressed in human leukocytes and human myeloid and lymphoid cell lines.* J Immunol, 1995. **155**(7): p. 3563-9.

84. Lin, B., W.R. Holmes, C.J. Wang, T. Ueno, A. Harwell, L. Edelstein-Keshet, T. Inoue, and A. Levchenko, *Synthetic spatially graded Rac activation drives cell polarization and movement.* Proc Natl Acad Sci U S A, 2012. **109**(52): p. E3668-77.

85. Liu, X., B. Ma, A.B. Malik, H. Tang, T. Yang, B. Sun, G. Wang, R.D. Minshall, Y. Li, Y. Zhao, R.D. Ye, and J. Xu, *Bidirectional regulation of neutrophil migration by mitogen-activated protein kinases.* Nat Immunol, 2012. **13**(5): p. 457-64.

86. Lockhart, P.B., M.T. Brennan, H.C. Sasser, P.C. Fox, B.J. Paster, and F.K. Bahrani-Mougeot, *Bacteremia associated with toothbrushing and dental extraction.* Circulation, 2008. **117**(24): p. 3118-25.

87. Loo, L.H., H.J. Lin, R.J. Steininger, 3rd, Y. Wang, L.F. Wu, and S.J. Altschuler, *An approach for extensibly profiling the molecular states of cellular subpopulations.* Nat Methods, 2009. **6**(10): p. 759-65.

88. Loughlin, R., R. Heald, and F. Nedelec, *A computational model predicts Xenopus meiotic spindle organization.* J Cell Biol, 2010. **191**(7): p. 1239-49.

89. Ma, W., A. Trusina, H. El-Samad, W.A. Lim, and C. Tang, *Defining network topologies that can achieve biochemical adaptation.* Cell, 2009. **138**(4): p. 760-73.

90. Machacek, M., L. Hodgson, C. Welch, H. Elliott, O. Pertz, P. Nalbant, A. Abell, G.L. Johnson, K.M. Hahn, and G. Danuser, *Coordination of Rho GTPase activities during cell protrusion.* Nature, 2009. **461**(7260): p. 99-103.

91. Macrae, E.K. and J.K. Spitznagel, *Ultrastructural localization of cationic proteins in cytoplasmic granules of chicken and rabbit polymorphonuclear leukocytes.* J Cell Sci, 1975. **17**(1): p. 79-94.

92. Marco, E., R. Wedlich-Soldner, R. Li, S.J. Altschuler, and L.F. Wu, *Endocytosis optimizes the dynamic localization of membrane proteins that regulate cortical polarity.* Cell, 2007. **129**(2): p. 411-22.

93. Maree, A.F., V.A. Grieneisen, and L. Edelstein-Keshet, *How cells integrate complex stimuli: the effect of feedback from phosphoinositides and cell shape on cell polarization and motility.* PLoS Comput Biol, 2012. **8**(3): p. e1002402.

94. Meinhardt, H., *Orientation of chemotactic cells and growth cones: models and mechanisms.* J Cell Sci, 1999. **112 (Pt 17)**: p. 2867-74.

95. Mendoza, M.C., E.E. Er, W. Zhang, B.A. Ballif, H.L. Elliott, G. Danuser, and J. Blenis, *ERK-MAPK drives lamellipodia protrusion by activating the WAVE2 regulatory complex.* Mol Cell, 2011. **41**(6): p. 661-71.

96. Mestas, J. and C.C. Hughes, *Of mice and not men: differences between mouse and human immunology.* J Immunol, 2004. **172**(5): p. 2731-8.

97. Metchnikoff, E., *Immunity in infective diseases*1905: University Press.

98. Meuret, G., U. Detel, H.P. Kilz, H.J. Senn, and H. van Lessen, *Human monocytopoiesis in acute and chronic inflammation.* Acta Haematol, 1975. **54**(6): p. 328-35.

99. Michaelson, D., J. Silletti, G. Murphy, P. D'Eustachio, M. Rush, and M.R. Philips, *Differential localization of Rho GTPases in live cells: regulation by hypervariable regions and RhoGDI binding.* J Cell Biol, 2001. **152**(1): p. 111-26.

100. Mintz, R., B.Z. Garty, T. Meshel, N. Marcus, C. Katanov, E. Cohen-Hillel, and A. Ben-Baruch, *Reduced expression of chemoattractant receptors by polymorphonuclear leukocytes in Hyper IgE Syndrome patients.* Immunol Lett, 2010. **130**(1-2): p. 97-106.

101. Mishra, P.K., A. Kunwar, S. Mukherji, and D. Chowdhury, *Dynamic instability of microtubules: effect of catastrophe-suppressing drugs.* Phys Rev E Stat Nonlin Soft Matter Phys, 2005. **72**(5 Pt 1): p. 051914.

102. Mistafa, O., A. Ghalali, S. Kadekar, J. Hogberg, and U. Stenius, *Purinergic receptor-mediated rapid depletion of nuclear phosphorylated Akt depends on pleckstrin homology domain leucine-rich repeat phosphatase, calcineurin, protein phosphatase 2A, and PTEN phosphatases.* J Biol Chem, 2010. **285**(36): p. 27900-10.

103. Mizuno, R., Y. Kamioka, K. Kabashima, M. Imajo, K. Sumiyama, E. Nakasho, T. Ito, Y. Hamazaki, Y. Okuchi, Y. Sakai, E. Kiyokawa, and M. Matsuda, *In vivo imaging reveals PKA regulation of ERK activity during neutrophil recruitment to inflamed intestines.* J Exp Med, 2014. **211**(6): p. 1123-36.

104. Mogilner, A., J. Allard, and R. Wollman, *Cell polarity: quantitative modeling as a tool in cell biology.* Science, 2012. **336**(6078): p. 175-9.

105. Morris, A.C., M. Brittan, T.S. Wilkinson, D.F. McAuley, J. Antonelli, C. McCulloch, L.C. Barr, N.A. McDonald, K. Dhaliwal, R.O. Jones, A. Mackellar, C. Haslett, A.W. Hay, D.G. Swann, N. Anderson, I.F. Laurenson, D.J. Davidson, A.G. Rossi, T.S. Walsh, and A.J. Simpson, *C5a-mediated neutrophil dysfunction is RhoA-dependent and predicts infection in critically ill patients.* Blood, 2011. **117**(19): p. 5178-88.

106. Morris, E.J., S. Jha, C.R. Restaino, P. Dayananth, H. Zhu, A. Cooper, D. Carr, Y. Deng, W. Jin, S. Black, B. Long, J. Liu, E. Dinunzio, W. Windsor, R. Zhang, S. Zhao, M.H. Angagaw, E.M. Pinheiro, J. Desai, L. Xiao, G. Shipps, A. Hruza, J. Wang, J. Kelly, S. Paliwal, X. Gao, B.S. Babu, L. Zhu, P. Daublain, L. Zhang, B.A. Lutterbach, M.R. Pelletier, U. Philippar, P. Siliphaivanh, D. Witter, P. Kirschmeier, W.R. Bishop, D. Hicklin, D.G. Gilliland, L. Jayaraman, L. Zawel, S. Fawell, and A.A. Samatar, *Discovery of a novel ERK inhibitor with activity in models of acquired resistance to BRAF and MEK inhibitors.* Cancer Discov, 2013. **3**(7): p. 742-50.

107. Murphy, P.M., *The molecular biology of leukocyte chemoattractant receptors.* Annu Rev Immunol, 1994. **12**: p. 593-633.

108. Nakae, H., S. Endo, K. Inada, T. Takakuwa, T. Kasai, and M. Yoshida, *Serum complement levels and severity of sepsis.* Res Commun Chem Pathol Pharmacol, 1994. **84**(2): p. 189-95.

109. Narang, A., *Spontaneous polarization in eukaryotic gradient sensing: a mathematical model based on mutual inhibition of frontness and backness pathways.* J Theor Biol, 2006. **240**(4): p. 538-53.

110. Neilson, M.P., D.M. Veltman, P.J. van Haastert, S.D. Webb, J.A. Mackenzie, and R.H. Insall, *Chemotaxis: a feedback-based computational model robustly predicts multiple aspects of real cell behaviour.* PLoS Biol, 2011. **9**(5): p. e1000618.

111. Nielsen, H., N.H. Valerius, and O.B. Schaffalitzky de Muckadell, *Selective defect of phagocyte responsiveness to N-f-Met-Leu-Phe in a familial syndrome of recurrent cold abscesses.* J Infect Dis, 1986. **153**(6): p. 1184-6.

112. Odell, G.M. and V.E. Foe, *An agent-based model contrasts opposite effects of dynamic and stable microtubules on cleavage furrow positioning.* J Cell Biol, 2008. **183**(3): p. 471-83.

113. Ofer, N., A. Mogilner, and K. Keren, *Actin disassembly clock determines shape and speed of lamellipodial fragments.* Proc Natl Acad Sci U S A, 2011. **108**(51): p. 20394-9.

114. Omann, G.M. and L.A. Sklar, *Response of neutrophils to stimulus infusion: differential sensitivity of cytoskeletal activation and oxidant production.* J Cell Biol, 1988. **107**(3): p. 951-8.

115. Onsum, M. and C.V. Rao, *A mathematical model for neutrophil gradient sensing and polarization.* PLoS Comput Biol, 2007. **3**(3): p. e36.

116. Otsuji, M., S. Ishihara, C. Co, K. Kaibuchi, A. Mochizuki, and S. Kuroda, *A mass conserved reaction-diffusion system captures properties of cell polarity.* PLoS Comput Biol, 2007. **3**(6): p. e108.

117. Parent, C.A. and P.N. Devreotes, *A cell's sense of direction.* Science, 1999. **284**(5415): p. 765-70.

118. Pestonjamasp, K.N., C. Forster, C. Sun, E.M. Gardiner, B. Bohl, O. Weiner, G.M. Bokoch, and M. Glogauer, *Rac1 links leading edge and uropod events through Rho and myosin activation during chemotaxis.* Blood, 2006. **108**(8): p. 2814-20.

119. Pillinger, M.H., A.S. Feoktistov, C. Capodici, B. Solitar, J. Levy, T.T. Oei, and M.R. Philips, *Mitogen-activated protein kinase in neutrophils and enucleate neutrophil cytoplasts: evidence for regulation of cell-cell adhesion.* J Biol Chem, 1996. **271**(20): p. 12049-56.

120. Raj, A. and A. van Oudenaarden, *Nature, nurture, or chance: stochastic gene expression and its consequences.* Cell, 2008. **135**(2): p. 216-26.

121. Rather, L.J., *Disturbance of function (functio laesa): the legendary fifth cardinal sign of inflammation, added by Galen to the four cardinal signs of Celsus.* Bull N Y Acad Med, 1971. **47**(3): p. 303-22.

122. Riedemann, N.C., R.F. Guo, K.D. Bernacki, J.S. Reuben, I.J. Laudes, T.A. Neff, H. Gao, C. Speyer, V.J. Sarma, F.S. Zetoune, and P.A. Ward, *Regulation by C5a of neutrophil activation during sepsis.* Immunity, 2003. **19**(2): p. 193-202.

123. Rittirsch, D., M.A. Flierl, B.A. Nadeau, D.E. Day, M. Huber-Lang, C.R. Mackay, F.S. Zetoune, N.P. Gerard, K. Cianflone, J. Kohl, C. Gerard, J.V. Sarma, and P.A.

Ward, *Functional roles for C5a receptors in sepsis.* Nat Med, 2008. **14**(5): p. 551-7.

124. Robbins, D.J. and M.H. Cobb, *Extracellular signal-regulated kinases 2 autophosphorylates on a subset of peptides phosphorylated in intact cells in response to insulin and nerve growth factor: analysis by peptide mapping.* Mol Biol Cell, 1992. **3**(3): p. 299-308.

125. Rodrigue, N. and H. Philippe, *Mechanistic revisions of phenomenological modeling strategies in molecular evolution.* Trends Genet, 2010. **26**(6): p. 248-52.

126. Rogers, S.L., U. Wiedemann, U. Hacker, C. Turck, and R.D. Vale, *Drosophila RhoGEF2 associates with microtubule plus ends in an EB1-dependent manner.* Curr Biol, 2004. **14**(20): p. 1827-33.

127. Ross, R. and G. Odland, *Human wound repair. II. Inflammatory cells, epithelial-mesenchymal interrelations, and fibrogenesis.* J Cell Biol, 1968. **39**(1): p. 152-68.

128. Rudolph, J., Y. Xiao, A. Pardi, and N.G. Ahn, *Slow inhibition and conformation selective properties of extracellular signal-regulated kinase 1 and 2 inhibitors.* Biochemistry, 2015. **54**(1): p. 22-31.

129. Saalfeld, S., A. Cardona, V. Hartenstein, and P. Tomancak, *As-rigid-as-possible mosaicking and serial section registration of large ssTEM datasets.* Bioinformatics, 2010. **26**(12): p. i57-63.

130. Sanderson, J.B., *On the Infective Product of Acute Inflammation.* Med Chir Trans, 1873. **56**: p. 345-84.

131. Sarma, J.V. and P.A. Ward, *New developments in C5a receptor signaling.* Cell Health Cytoskelet, 2012. **4**: p. 73-82.

132. Schliwa, M., *Chromatophores: their use in understanding microtubule-dependent intracellular transport.* Methods Cell Biol, 1982. **25 Pt B**: p. 285-312.

133. Schmid, B., J. Schindelin, A. Cardona, M. Longair, and M. Heisenberg, *A high-level 3D visualization API for Java and ImageJ.* BMC Bioinformatics, 2010. **11**: p. 274.

134. Schneider, C.A., W.S. Rasband, and K.W. Eliceiri, *NIH Image to ImageJ: 25 years of image analysis.* Nat Methods, 2012. **9**(7): p. 671-5.

135. Servant, G., O.D. Weiner, P. Herzmark, T. Balla, J.W. Sedat, and H.R. Bourne, *Polarization of chemoattractant receptor signaling during neutrophil chemotaxis.* Science, 2000. **287**(5455): p. 1037-40.

136. Servant, G., O.D. Weiner, E.R. Neptune, J.W. Sedat, and H.R. Bourne, *Dynamics of a chemoattractant receptor in living neutrophils during chemotaxis.* Mol Biol Cell, 1999. **10**(4): p. 1163-78.

137. Shibata, T., M. Nishikawa, S. Matsuoka, and M. Ueda, *Modeling the self-organized phosphatidylinositol lipid signaling system in chemotactic cells using quantitative image analysis.* J Cell Sci, 2012. **125**(Pt 21): p. 5138-50.

138. Solomkin, J.S., L.A. Cotta, J.K. Brodt, J.W. Hurst, and C.K. Ogle, *Neutrophil dysfunction in sepsis. III. Degranulation as a mechanism for nonspecific deactivation.* J Surg Res, 1984. **36**(5): p. 407-12.

139. Solomkin, J.S., M.K. Jenkins, R.D. Nelson, D. Chenoweth, and R.L. Simmons, *Neutrophil dysfunction in sepsis. II. Evidence for the role of complement activation products in cellular deactivation.* Surgery, 1981. **90**(2): p. 319-27.

140. Southwick, F.S., G.A. Dabiri, M. Paschetto, and S.H. Zigmond, *Polymorphonuclear leukocyte adherence induces actin polymerization by a transduction pathway which differs from that used by chemoattractants.* J Cell Biol, 1989. **109**(4 Pt 1): p. 1561-9.

141. Southwick, F.S., G.A. Dabiri, and T.P. Stossel, *Neutrophil actin dysfunction is a genetic disorder associated with partial impairment of neutrophil actin assembly in three family members.* J Clin Invest, 1988. **82**(5): p. 1525-31.

142. Spector, W.G. and D.A. Willoughby, *The origin of mononuclear cells in chronic inflammation and tuberculin reactions in the rat.* J Pathol Bacteriol, 1968. **96**(2): p. 389-99.

143. Srinivasan, S., F. Wang, S. Glavas, A. Ott, F. Hofmann, K. Aktories, D. Kalman, and H.R. Bourne, *Rac and Cdc42 play distinct roles in regulating PI(3,4,5)P3 and polarity during neutrophil chemotaxis.* J Cell Biol, 2003. **160**(3): p. 375-85.

144. Stephens, L., L. Milne, and P. Hawkins, *Moving towards a better understanding of chemotaxis.* Curr Biol, 2008. **18**(11): p. R485-94.

145. Straus, W., *Colorimetric analysis with N, N-dimethyl-p-phenylenediamine of the uptake of intravenously injected horseradish peroxidase by various tissues of the rat.* J Biophys Biochem Cytol, 1958. **4**(5): p. 541-50.

146. Swaney, K.F., C.H. Huang, and P.N. Devreotes, *Eukaryotic chemotaxis: a network of signaling pathways controls motility, directional sensing, and polarity.* Annu Rev Biophys, 2010. **39**: p. 265-89.

147. Tkachenko, E., M. Sabouri-Ghomi, O. Pertz, C. Kim, E. Gutierrez, M. Machacek, A. Groisman, G. Danuser, and M.H. Ginsberg, *Protein kinase A governs a RhoA-RhoGDI protrusion-retraction pacemaker in migrating cells.* Nat Cell Biol, 2011. **13**(6): p. 660-7.

148. Van Keymeulen, A., K. Wong, Z.A. Knight, C. Govaerts, K.M. Hahn, K.M. Shokat, and H.R. Bourne, *To stabilize neutrophil polarity, PIP3 and Cdc42 augment RhoA activity at the back as well as signals at the front.* J Cell Biol, 2006. **174**(3): p. 437-45.

149. VanBuren, V., L. Cassimeris, and D.J. Odde, *Mechanochemical model of microtubule structure and self-assembly kinetics.* Biophys J, 2005. **89**(5): p. 2911-26.

150. von Dassow, G., E. Meir, E.M. Munro, and G.M. Odell, *The segment polarity network is a robust developmental module.* Nature, 2000. **406**(6792): p. 188-92.

151. Wang, F., P. Herzmark, O.D. Weiner, S. Srinivasan, G. Servant, and H.R. Bourne, *Lipid products of PI(3)Ks maintain persistent cell polarity and directed motility in neutrophils.* Nat Cell Biol, 2002. **4**(7): p. 513-8.

152. Wang, Y., C.J. Ku, E.R. Zhang, A.B. Artyukhin, O.D. Weiner, L.F. Wu, and S.J. Altschuler, *Identifying network motifs that buffer front-to-back signaling in polarized neutrophils.* Cell Rep, 2013. **3**(5): p. 1607-16.

153. Ward, P.A., *The harmful role of c5a on innate immunity in sepsis.* J Innate Immun, 2010. **2**(5): p. 439-45.

154. Ward, P.A., *The dark side of C5a in sepsis.* Nat Rev Immunol, 2004. **4**(2): p. 133-42.

155. Wauson, E.M., M.L. Guerra, B. Barylko, J.P. Albanesi, and M.H. Cobb, *Off-target effects of MEK inhibitors.* Biochemistry, 2013. **52**(31): p. 5164-6.

156. Weiner, O.D., W.A. Marganski, L.F. Wu, S.J. Altschuler, and M.W. Kirschner, *An actin-based wave generator organizes cell motility.* PLoS Biol, 2007. **5**(9): p. e221.

157. Weiner, O.D., P.O. Neilsen, G.D. Prestwich, M.W. Kirschner, L.C. Cantley, and H.R. Bourne, *A PtdInsP(3)- and Rho GTPase-mediated positive feedback loop regulates neutrophil polarity.* Nat Cell Biol, 2002. **4**(7): p. 509-13.

158. Welf, E.S., S. Ahmed, H.E. Johnson, A.T. Melvin, and J.M. Haugh, *Migrating fibroblasts reorient directionality by a metastable, PI3K-dependent mechanism.* J Cell Biol, 2012. **197**(1): p. 105-14.

159. White, F.W., *CULTURES FROM THE BLOOD In SEPTICAEMIA, PNEUMONIA, MENINGITIS AND CHRONIC DISEASES.* J Exp Med, 1899. **4**(3-4): p. 425-50.

160. Wong, K., O. Pertz, K. Hahn, and H. Bourne, *Neutrophil polarization: spatiotemporal dynamics of RhoA activity support a self-organizing mechanism.* Proc Natl Acad Sci U S A, 2006. **103**(10): p. 3639-44.

161. Wong, K., A. Van Keymeulen, and H.R. Bourne, *PDZRhoGEF and myosin II localize RhoA activity to the back of polarizing neutrophil-like cells.* J Cell Biol, 2007. **179**(6): p. 1141-8.

162. Wu, J., A. Pipathsouk, A. Keizer-Gunnink, F. Fusetti, W. Alkema, S. Liu, S. Altschuler, L. Wu, A. Kortholt, and O.D. Weiner, *Homer3 regulates the establishment of neutrophil polarity.* Mol Biol Cell, 2015. **26**(9): p. 1629-39.

163. Wu, S., A. Wells, L.G. Griffith, and D.A. Lauffenburger, *Controlling multipotent stromal cell migration by integrating "course-graining" materials and "fine-tuning" small molecules via decision tree signal-response modeling.* Biomaterials, 2011. **32**(30): p. 7524-31.

164. Wu, Y., L. Zhan, Y. Ai, M. Hannigan, M. Gaestel, C.K. Huang, and J.A. Madri, *MAPKAPK2-mediated LSP1 phosphorylation and FMLP-induced neutrophil polarization.* Biochem Biophys Res Commun, 2007. **358**(1): p. 170-5.

165. Xiao, Z., N. Zhang, D.B. Murphy, and P.N. Devreotes, *Dynamic distribution of chemoattractant receptors in living cells during chemotaxis and persistent stimulation.* J Cell Biol, 1997. **139**(2): p. 365-74.

166. Xiong, Y., C.H. Huang, P.A. Iglesias, and P.N. Devreotes, *Cells navigate with a local-excitation, global-inhibition-biased excitable network.* Proc Natl Acad Sci U S A, 2010. **107**(40): p. 17079-86.

167. Xu, J., F. Wang, A. Van Keymeulen, P. Herzmark, A. Straight, K. Kelly, Y. Takuwa, N. Sugimoto, T. Mitchison, and H.R. Bourne, *Divergent signals and*

cytoskeletal assemblies regulate self-organizing polarity in neutrophils. Cell, 2003. **114**(2): p. 201-14.

168. Xu, J., F. Wang, A. Van Keymeulen, M. Rentel, and H.R. Bourne, *Neutrophil microtubules suppress polarity and enhance directional migration.* Proc Natl Acad Sci U S A, 2005. **102**(19): p. 6884-9.

169. Ye, R.D., F. Boulay, J.M. Wang, C. Dahlgren, C. Gerard, M. Parmentier, C.N. Serhan, and P.M. Murphy, *International Union of Basic and Clinical Pharmacology. LXXIII. Nomenclature for the formyl peptide receptor (FPR) family.* Pharmacol Rev, 2009. **61**(2): p. 119-61.

170. Yuan, J., R.W. Branch, B.G. Hosu, and H.C. Berg, *Adaptation at the output of the chemotaxis signalling pathway.* Nature, 2012. **484**(7393): p. 233-6.

171. Zeya, H.I. and J.K. Spitznagel, *Antibacterial and Enzymic Basic Proteins from Leukocyte Lysosomes: Separation and Identification.* Science, 1963. **142**(3595): p. 1085-7.

172. Zhang, E.R., L.F. Wu, and S.J. Altschuler, *Envisioning migration: mathematics in both experimental analysis and modeling of cell behavior.* Curr Opin Cell Biol, 2013. **25**(5): p. 538-42.

173. Zigmond, S.H., *Ability of polymorphonuclear leukocytes to orient in gradients of chemotactic factors.* J Cell Biol, 1977. **75**(2 Pt 1): p. 606-16.

174. Zigmond, S.H., H.I. Levitsky, and B.J. Kreel, *Cell polarity: an examination of its behavioral expression and its consequences for polymorphonuclear leukocyte chemotaxis.* J Cell Biol, 1981. **89**(3): p. 585-92.

175. Zigmond, S.H. and S.J. Sullivan, *Sensory adaptation of leukocytes to chemotactic peptides.* J Cell Biol, 1979. **82**(2): p. 517-27.

176. Zu, Y.L., J. Qi, A. Gilchrist, G.A. Fernandez, D. Vazquez-Abad, D.L. Kreutzer, C.K. Huang, and R.I. Sha'afi, *p38 mitogen-activated protein kinase activation is required for human neutrophil function triggered by TNF-alpha or FMLP stimulation.* J Immunol, 1998. **160**(4): p. 1982-9.